Silesian University of Technology

1 2 9 0

UNIVERSIDADE D COIMBRA

Amjad Iqbal

CHARACTERIZATION OF DESTRUCTION PROCESSES IN TWO-PHASE THERMAL BARRIER COATINGS – MODEL INVESTIGATIONS IN CONDITIONS OF HIGH-TEMPERATURE OXIDATION AND CORROSION IN LIQUID SALTS DEPOSITS

February 2025

Characterization of Destruction Processes in Two Phase Thermal Barrier Coatings – Model Investigations in Conditions of High Temperature Oxidation and Corrosion in Liquid Salts Deposits

Submitted in Partial Fulfilment of the Requirements for the Degree of Doctor of Philosophy in Materials Engineering at Silesian University of Technology, and Degree of Doctor of Philosophy in Mechanical Engineering in the specialty of Surface Engineering and Nanomaterials at University of Coimbra

Characterization of destruction processes in two phase thermal barrier coatings – model investigations in conditions of high temperature oxidation and corrosion in liquid salts deposits

Author

Amjad Iqbal

Advisor[s]

Associate Professor Grzegorz Moskal

Full Professor Albano Cavaleiro

Institutional Collaboration

Institute 1	**Silesian University of Technology**	**Institute 2**	**University of Coimbra**

Katowice (Poland), Coimbra (Portugal) February, 2025

“My Lord, expand for me my chest [with assurance]; ease for me my task; and untie the knot from my tongue, that they may understand my speech”!

[Quran: Surah Taha 20:25-28]

ACKNOWLEDGEMENTS

The work presented in this doctoral thesis focuses on the Modification of Thermal barrier coatings, by advanced ceramic materials, innovative architecture of ceramic coatings, as well as the identification of the major routes of degradation under pure sulphates. Doctoral dissertation was carried out at the Department of Materials Technologies, Silesia University of Technology, Poland and at the Department of Mechanical Engineering, University of Coimbra, Portugal.

First and foremost, I would like to say, “All praise is due to Allah (SWTH) for His countless blessings and guidance in my life. I am very thankful to Professor Grzegorz Moskal at the Silesian University of Technology and Professor Albano Cavaleiro at the University of Coimbra for putting their trust in me and allowing me to work under their supervision for my PhD dissertation. They both have made this entire process much smoother for me and have granted me permission to pursue a dual doctorate. I am deeply appreciative of their humble behavior, unwavering support, and valuable mentorship at every step, which have been instrumental in helping me identify and accomplish the key milestones of this dissertation.

Next, I want to thank my friends for their engaging discussions, the memorable trips we've shared, and the delightful experiences we've had together. Their camaraderie and support have made this journey even more fulfilling.

Finally, I would like to express my gratitude to my all-family members for their unwavering love and support, which has been an anchor throughout my research journey. Especially the memories of my beloved mother, father, wife and my children’s have been a constant source of inspiration and strength.

Abstract

The main objective of the work is the development of thermal barrier coatings (TBCs) by modification of the top ceramic layer and the identification of their new degradation routes. TBCs have emerged as a promising solution for improving the performance, durability, and lifespan of industrial components exposed to high temperatures, corrosive conditions, and neutron irradiation. Plasma spray (PS) technology was used to deposit bond coat (BC) and topcoat (TC) layers due to its large application in industrial sector and availability of equipment. The concept of dual phase was introduced in the topcoat layer (ZrO2-based ceramics), which is a new innovative way to fabricate TBCs with low thermal conductivity and higher thermal stability. Recently, dual phase system got much attention due to their low thermal conductivity, offer higher susceptibility at higher temperature which is the main requirement of advanced ceramic materials. Dual phase system was fabricated from commercially available advanced ceramic materials specially pyrochlore-fluorite nature of zirconates and cerates. The complex phenomenon, involving the simultaneous presence of multiple corrosive species, is extensively explored under condition of hot corrosion in molten sodium sulphate and pure oxidation. Three advanced two phase-system Gadolinium Zirconate with Yttria Stabilized Zirconia ($Gd_2Zr_2O_7$+Y_2O_3(ZrO_2)), Lanthanum Zirconate based ($La_2Zr_2O_7$+Y_2O_3(ZrO_2)), and Lanthanum Cerate ($La_2Ce_2O_7$+Y_2O_3(ZrO_2)) were investigated at the temperature of 920°C and 970°C for hot corrosion. The results revealed that the major processes involved during the degradation are phase decomposition, formation of new phase with lower and higher content of rare earth oxide, non-equilibrium diffusion process, and mutual interactions between dual phase TBCs. Visual inspection of the TBCs coatings after prolonged exposure revealed an intact ceramic layer with minor spallation only observed at the edges.

Keywords: Thermal Barrier Coatings, Hot Corrosion, High Temperature Oxidation, Degradation Routes, Dual Phase Systems, Molten Sodium Sulphate.

Abstrakcyjny

Głównym celem przedstawionej pracy jest opracowanie nowego typu powłokowych barier termicznych (TBC) poprzez modyfikację zewnętrznej warstwy ceramicznej i identyfikację nowych mechanizmów degradacji. TBC są obiecującym rozwiązaniem poprawiającym wydajność, trwałość i żywotność komponentów przemysłowych, które narażone są na wysokie temperatury, warunki korozyjne i promieniowanie neutronowe. Do otrzymania powłok TBC, w tym wmiędzywarstwy oraz warstwy ceramicznej, zastsowano technologia natrysku plazmowego (PS), co wynika z jej szerokiego zastosowanie w sektorze przemysłowym i dostępność sprzętu. Koncepcja powłok duwfazowych, bazująca na ceramice ZrO2 stanowi nowy innowacyjny kierunek rowozju powłok TBC o niskiej przewodności cieplnej i wyższej stabilności termicznej. Ostatnio systemy dwufazowe zyskały dużą uwagę ze względu na ich niską przewodność cieplną, oferując większą odporność w wyższych temperaturach, co jest głównym wymogiem zaawansowanych materiałów ceramicznych. System dwufazowy został wytworzony z dostępnych komercyjnie proszków, w tym cyrkonianów i ceranów o pirochlorowo-fluorytowej typie sieci. Badaniom poddano systemy TBC testowane w złożonych warunkach korozyjnych, w tym w ciekłych osadach solnych. Trzy zaawansowane dwufazowe systemy na baazie cyrkonianu gadolinu z tlenkiem cyrkonu stabilizowanym tlenkiem itru ($Gd_2Zr_2O_7$+Y_2O_3(ZrO_2)), cyrkonianu lantanu ($La_2Zr_2O_7$+Y_2O_3(ZrO_2)) i cerianu lantanu ($La_2Ce_2O_7$+Y_2O_3(ZrO_2)) zostały zbadane w temperaturze 920°C i 970°C pod kątem odporności na korozję na gorąco. Wyniki wykazały, że istotne procesy zachodzące podczas procesu degradacji to rozkład ftermiczny bazowych faz, tworzenie nowej fazy o niższej i wyższej zawartości tlenku ziem rzadkich, proces dyfuzji nierównowagowej i proces wzajemnej interakcji między dwufazowymi TBC. Po przedłużonej ekspozycji, wizualna inspekcja powłok TBC, wykazała nienaruszoną warstwę ceramiczną z niewielkimi odpryskami obserwowanymi tylko na krawędziach.

Słowa kluczowe: powłoki termoizolacyjne, korozja na gorąco, czyste utlenianie, drogi degradacji, układy dwufazowe, stopiony siarczan sodu.

Resumo

O principal objetivo deste trabalho é o desenvolvimento de revestimentos de barreira térmica (TBCs) através da modificação da camada cerâmica de topo e a identificação de novas caminhos de degradação. Os TBC surgiram como uma solução promissora para melhorar o desempenho, a durabilidade e a vida útil dos componentes industriais expostos a altas temperaturas, condições corrosivas e irradiação por neutrões. A tecnologia de projeção térmica (PS) foi utilizada para depositar camadas de adesão (BC) e de topo (TC) devido à grande disponibilidade de equipamentos e à sua aplicação no setor industrial. O conceito de fase dupla foi introduzido na camada de topo (cerâmica à base de ZrO_2), que é a forma inovadora de fabricar TBCs com baixa condutividade térmica e maior estabilidade térmica. Recentemente, o sistema bifásico tem recebido grande atenção devido à sua baixa condutividade térmica, oferecendo uma maior resistência a temperaturas mais elevadas, que é o principal requisito dos materiais cerâmicos avançados. O sistema de fase dupla foi fabricado a partir de materiais cerâmicos avançados disponíveis comercialmente, especialmente do tipo pirocloro-fluorite de zirconatos e ceratos. O fenómeno complexo que envolve a presença simultânea de múltiplas espécies corrosivas é extensivamente explorado em condições de corrosão a quente em sais de sulfato de sódio fundido assim como em oxidação pura. Foram investigados em corrosão a quente, às temperaturas de 920°C e 970°C, três sistemas avançados: (i) zirconato de gadolínio de duas fases com zircónio estabilizado com ítria ($Gd_2Zr_2O_7$+Y_2O_3(ZrO_2)), (ii) zirconato à base de lantânio ($La_2Zr_2O_7$+Y_2O_3(ZrO_2)) e, (iii) cerato de lantânio ($La_2Ce_2O_7$+Y_2O_3(ZrO_2)). Os resultados revelaram que os principais processos envolvidos durante a degradação são a decomposição de fases, a formação de uma nova fase com teores mais elevados ou reduzidos de óxido de terras raras, o processo de difusão fora de equilíbrio e o processo de interação mútua entre TBCs de fase dupla. A inspeção visual dos revestimentos de TBCs após exposição prolongada revelou uma camada cerâmica intacta, com pequena fragmentação observada apenas nas arestas.

Palavras-chave: Revestimentos de Barreira Térmica, Corrosão a Quente, Oxidação a Temperaturas Elevadas, Modelos de Degradação, Sistemas Bi-fásicos; Sulfato de Sódio Fundido.

Contents

LIST OF FIGURES xi

LIST OF TABLES xv

LIST OF SIMBOLS AND ACRONYMS/ ABBREVIATIONS xvii
List of Formulas and Symbols xvii
Acronyms/Abbreviations xvii

1. INTRODUCTION 1
1.1. State of the art TBCs 2
1.1.1. High temperature advanced ceramic materials (ACM) 4
1.2. Research gap 11
1.2.1. Research questions 12
1.3. Thesis outline 12

2. LITERATURE REVIEW 15
2.1. Introduction to hot corrosion 15
2.2. Type I and Type II hot corrosion 18
2.3. Rare earth zirconates ($Re_2Zr_2O_7$) 24
2.4. Dual-phase TBCs- innovative coatings type 28
2.5. References. 32

3. EXPERIMENTAL PROCEDURE 36
3.1. State of the art experiment 36
3.2. Hot corrosion – pure oxidation test 39
3.3. Characterization techniques 40

4. LANTHANUM ZIRCONATE BASED TBCS 41
4.1. Introduction to LZO based TBCs 41
4.2. Results and discussion. 44
4.2.1. Characterization of feedstock powders 44
4.2.2. Characterization of as deposited and corroded samples 47
4.2.3. The overall strength and reliability of TBCs 47
4.2.4. Examining the stability of phases in LZO+YSZ 50
4.3. Summary 63
4.4. Conclusion 64
4.5. References: 65

5. GADOLINIUM ZIRCONATE BASED TBCS 67
5.1. Introduction to GZO based TBCs 67
5.2. Results and discussion. 69
5.2.1. Characterization of feedstock powders 69
5.2.2. Characterization of coatings samples 72
5.2.3. Degradation mechanism in GZO+YSZ systems 73
5.3. Summary 87
5.4. Conclusion 88

5.5. References. 88
6. LANTHANUM CERATE BASED TBCS 90
6.1. Introduction to LCO based TBCs 90
6.2. Results and discussion 93
6.2.1. Characterization of feedstock powders 93
6.2.2. Characterization of coatings samples 96
6.2.3. Degradation mechanism in LCO+YSZ 99
6.3. Summary 109
6.4. Conclusion 109
6.5. References 110
7. CONCLUSION 112
ANNEX A 115

LIST OF FIGURES

Figure 1.1. SEM view of Engine Alliance GP7200 aircraft engine, Visualization of layer of TBCs System (Engine image courtesy of Engine Alliance, turbine blade photograph courtesy of YXLON, and the SEM micrograph.....3

Figure 2.1. Differential thermal analysis of pure sodium sulphate, samarium zirconates and its alloying elements.....18

Figure 2.2. (a) Type 1: Corrosion of nickel, with and without the presence of the salt Na_2SO_4 in 1 atm. O_2+4% SO_2 at 900 °C. (b) Type 2: Corrosion of nickel at 700 °C, covered with Na_2SO_4 deposit (2.5 gm/cm^2) in 1 atm. O_2+4% SO_2 at different total gas pressure…..22

Figure 2.3. (a) Crystal structure fluorite type $Re_2Zr_2O_7$. (b) Crystal structure fpyrocholore type $Re_2Zr_2O_7$.....25

Figure 2.4. (a) XRD pattern of high entropy ceramic after 1500 °C for 3 h (b) Crystal pyrocholore type structure (c) Broad View in (222) differaction peaks (d) Lattice parameter of sintered (e) Thermal conductivity after 1500 °C for 3 h.....27

Figure 2.5. The architecture of a Fabricated System and level of advancements.....31

Figure 3.1. Flow sheet Daigram for the Experimental procedure…….38

Figure 4.1. SEM micrographs of YSZ (a, c) and LZO (b, d) powders: high-resolution SEM images of powders at 100 μm and at 50 μm. Kikuchi lines: EBSD (electron backscattered diffraction) method. (e-YSZ), (f-LZO)…….45

Figure 4.2. XRD Patterns for YSZ (a) and LZO (b) powders, indicating their phase composition. (c) Particle size measurement via Master Sizer……46

Figure 4.3. SEM Micrographs of YSZ-LZO dual phase coatings: SEM top surface morphology, top surface EDX morphology……..48

Figure 4.4. SEM micrographs of YSZ-LZO dual phase coatings: SEM cross sectional surface morphology……..49

Figure 4.5. Stereomicrograph of YSZ-LZO dual phase coatings: Images of the examined surface coatings following exposure to high-temperature corrosion testing in (Na_2SO_4+V_2O_5) corrosion environment at temperatures of 920°C for 240 hours and 970°C for 72 hours……...50

Figure 4.6. XRD patterns of 8YSZ + LZO coatings in as-sprayed condition and after exposure to Na_2SO_4 at 920°C and 970°C……...51

Figure 4.7. Top surface morphology of YSZ-LZO dual phase coatings: SEM images of the examined top surface coatings following exposure in pure sodium sulfate environment at temperatures of 920°C for 240 hours. Elemental mapping images of TBCs…….53

Figure 4.8. Top surface morphology of YSZ-LZO dual phase coatings: SEM images of the examined top surface coatings following exposure in Na_2SO_4 at temperatures of 970°C for 96 hours. Elemental mapping images of TBCs…….54

Figure 4.9. XRD patterns of 8YSZ + LZO coatings in as-sprayed condition and after exposure to $Na_2SO_4 + V_2O_5$ at 920°C and 970°C……..55
Figure 4.10. Top surface morphology of YSZ-LZO dual phase coatings: SEM images of the examined top surface coatings following exposure in $Na_2SO_4 + V_2O_5$ at temperatures of 920°C for 240 hours. Elemental mapping images of TBCs……...57
Figure 4.11. Top surface morphology of YSZ-LZO dual phase coatings: SEM images of the examined top surface coatings following exposure in $Na_2SO_4 + V_2O_5$ at temperatures of 970°C for 72 hours. Elemental mapping images of TBCs…….58
Figure 4.12. (a) XRD patterns for pellets 100% 8YSZ at 800°C,900 °C, 1000 °C, 1100 °C, 1200 °C, 1300 °C, and 1400 °C for 168 h. (b) XRD patterns for pellets 90% 8YSZ + 10% Na_2SO_4 annealed at 800°C,900 °C, 1000 °C, 1100 °C, 1200 °C, 1300 °C, and 1400 °C for 168 h. (c) XRD patterns for pellets 90% 8YSZ +9% Na_2SO_4 + 1% V_2O_5 annealed at 800°C,900 °C, 1000 °C, 1100 °C, 1200 °C, 1300 °C, and 1400 °C for 168 h……59
Figure 4.13. (a) XRD patterns for pellets 100% $La_2Zr_2O_7$ at 800°C,900 °C, 1000 °C, 1100 °C, 1200 °C, 1300 °C, and 1400 °C for 168 h. (b) XRD patterns for pellets 90% $La_2Zr_2O_7$ + 10% Na_2SO_4 annealed at 800°C,900 °C, 1000 °C, 1100 °C, 1200 °C, 1300 °C, and 1400 °C for 168 h. (c) XRD patterns for pellets 90% $La_2Zr_2O_7$ + 9% Na_2SO_4 + 1% V_2O_5 annealed at 800°C,900 °C, 1000 °C, 1100 °C, 1200 °C, 1300 °C, and 1400 °C for 168 h……59
Figure 4.14. (a) XRD patterns for pellets 50 % 8YSZ – 50 % $La_2Zr_2O_7$ annealed at 800°C, 900 °C, 1000 °C, 1100 °C, 1200 °C, 1300 °C, and 1400 °C for 168 h. (b) XRD patterns for pellets 45 % 8YSZ + 45 % $La_2Zr_2O_7$ + 10% Na_2SO_4 annealed at 800°C,900 °C, 1000 °C, 1100 °C, 1200 °C, 1300 °C, and 1400 °C for 168 h. (c) XRD patterns for pellets 45 % 8YSZ + 45 % $La_2Zr_2O_7$ + 9% Na_2SO_4 + 1% V_2O_5 annealed at 800°C,900 °C, 1000 °C, 1100 °C, 1200 °C, 1300 °C, and 1400 °C for 168 h……..60
Figure 4.15. (a) XRD patterns for pellets 33.3 % 8YSZ + 33.3 % $La_2Zr_2O_7$ +33.3 % Cr_2O_3 annealed at 800°C,900 °C, 1000 °C, 1100 °C, 1200 °C, 1300 °C, and 1400 °C for 168 h. (b) XRD patterns for pellets 40 % 8YSZ + 40 % $La_2Zr_2O_7$ +10% Cr_2O_3+ 10% Na_2SO_4 annealed at 800°C,900 °C, 1000 °C, 1100 °C, 1200 °C, 1300 °C, and 1400 °C for 168 h.(c) XRD patterns for pellets 40 % 8YSZ + 40 % $La_2Zr_2O_7$ + 10% Cr_2O_3+ 9% Na_2SO_4 +1% V_2O_5 annealed at 800°C,900 °C, 1000 °C, 1100 °C, 1200 °C, 1300 °C, and 1400 °C for 168 h…..60
Figure 4.16. (a) XRD patterns for pellets 33.3 % 8YSZ + 33.3 % $La_2Zr_2O_7$ +33.3 % NiO annealed at 800°C,900 °C, 1000 °C, 1100 °C, 1200 °C, 1300 °C, and 1400 °C for 168 h.(b) XRD patterns for pellets 40 % 8YSZ + 40 % $La_2Zr_2O_7$ +10% NiO + 10% Na_2SO_4 annealed at 800°C,900 °C, 1000 °C, 1100 °C, 1200 °C, 1300 °C, and 1400 °C for 168 h. (c) XRD patterns for pellets 40 % 8YSZ + 40 % $La_2Zr_2O_7$ + 10% NiO + 9% Na_2SO_4 +1% V_2O_5 annealed at 800°C,900 °C, 1000 °C, 1100 °C, 1200 °C, 1300 °C, and 1400 °C for 168 h…..62
Figure 4.17. DTA tract of $La_2Zr_2O_7$ and 8YSZ compared with pure Al_2O_3, Cr_2O_3, NiO, Y_2O_3……..63
Figure 4.18. Phase composition of the ceramic topcoat of 50% $La_2Zr_2O_7$ + 50% 8YSZ TBC composite after oxidation test at 1100 °C with 360 h of exposure…….63

Figure 5.1. SEM micrographs of YSZ and GZO powders: **a**,**b** top-surface images of YSZ and GZO powders, **c**,**d** cross-sectional views of YSZ and GZO powders……71
Figure 5.2. X-ray diffraction patterns of **a** yttria-stabilized zirconia and **b** gadolinium zirconates feedstock powders used in the APS process……71
Figure 5.3. The EBSD patterns of **a** yttria-stabilized zirconia, **b** gadolinium zirconates, and their crystallographic details……72

Figure 5.4. The granule size of distribution of prayed feedstock powders……72
Figure 5.5. Cross-section analysis of 8YSZ/GZO dual-phase TBCs with chemical composition analysis in characteristic micro-areas……73
Figure 5.6. Top surface morphology of 8YSZ/GZO dual-phase as-sprayed coatings……...73

Figure 5.7. Visualization of the examined top surfaces of 8YSZ/GZO TBC systems in the as-prayed condition a after hot corrosion testing in a pure sodium sulphate (Na_2SO_4) environment at temperatures of 920 °C for 124 (b) and 240 h (c) and 970 °C for 124 h (d)……74
Figure 5.8. Top surface morphology and chemical composition in characteristic micro-areas of 8YSZ/GZO TBC systems after hot corrosion at 920 °C for 240 h……77
Figure 5.9. Top surface morphology and chemical composition in characteristic micro-areas of 8YSZ/GZO TBC systems after hot corrosion at 970 °C for 124 h……78
Figure 5.10. Phase constituent of 8YSZ/GZO TBC systems after hot corrosion tests……..79
Figure 5.11. Fluorite new-formed compounds localization in ZrO -GdO……80

Figure 5.12. XRD analysis of powder-based GZO + 8YSZ and
GZO + YSZ + Na_2SO_4 systems under high-temperature annealing at temperature range 800–1400 °C……81
Figure 5.13. DTA characterization of mutual interactions between 8YSZ and GZO powders and Na_2SO_4 salt at temperature range 25–1200 °C……...82
Figure 5.14. Phase constituent of the 25 % 8YSZ + 75 % GZO TBC system after long-term oxidation at temperature 1100 °C……83
Figure 5.15. Phase component of 50 % 8YSZ + 50 % GZO TBC system after long-term oxidation at temperature 1100 °C……84
Figure 5.16. Phase component of 75 % 8YSZ + 25 % GZO TBC system after long-term oxidation at temperature 1100 °C……85
Figure 5.17. Phase constituent of pure 8YSZ and GZO powders, as well as the equally weighted mixture 8YSZ + GZO, as a function of temperature……..86

Figure 6.1. SEM micrographs of YSZ (a, c) and LCO (b, d) powders: high-resolution SEM images of powders at 100 μm and at 50 μm. Kikuchi lines: EBSD (e-f) method……...94
Figure 6.2. XRD Patterns for LCO (a) and YSZ (b) powders, indicating their phase composition. (c) Particle size measurements were obtained using a Master Sizer, with values following a log-normal distribution……..96
Figure 6.3. SEM Micrographs of YSZ-LCO dual phase coatings: SEM top surface morphology, top surface EDX morphology……..97
Figure 6.4. SEM micrographs of YSZ-LCO dual phase coatings: SEM and EDX cross sectional surface morphology……...98
Figure 6.5. Stereomicrograph of YSZ-LCO dual phase coatings: Images of the examined high-temperature corrosion testing in (Na_2SO_4) corrosion environment at temperatures of 920°C for 240 hours and 970°C for 124 hours……...98
Figure 6.6. Diffraction pattern of heat-treated LCO-YSZ based dual phase coatings at 920°C (10 days) followed by XRD/SEM and further sintering at 970°C (4 days)……..100
Figure 6.7. Top Surface SEM morphology and EDX analysis after hot corrosion 920 °C……101
Figure 6.8. Top Surface SEM morphology and EDX analysis after hot corrosion 970 °C……102
Figure 6.9. Cross sectional SEM morphology and EDX analysis after 970 °C……...103

Figure 6.10. Phase constituent of hot corrosion at lower temperature for 8YSZ and LCO dual phase, as a function of temperature in sodium sulphate for 24 hours each interval…..107
Figure 6.11. Phase constituent of pure oxidation at higher temperature for 8YSZ and LCO dual phase, as a function of temperature for 24 hours each interval…….108

LIST OF TABLES

Table 1.1. Promising properties of next generation ACM…….……7

Table 2.1. The melting temperature for common sulphate salts…….…….17

Table 2.2. Reaction during combustion process at high temperature……..23

T**able 2.3**. Thermal conductivity values of common zirconates at 1473K……..25

Table 2.4. Calculated CTE of rare earth zirconate elements……...28

Table 3.1. Chemical composition of IN 625 substrate alloy……...37

Table 3.2. Technical Parameters for the Depositions of coatings……...37

Table 6.1. Basic Proposed equation for current TBCs System……..106

LIST OF SIMBOLS AND ACRONYMS/ ABBREVIATIONS

List of Formulas and Symbols

LZO – $La_2Zr_2O_7$

GZO – $Gd_2Zr_2O_7$

LCO – $La_2Ce_2O_7$

Sodium Sulphate – Na_2SO_4

Acronyms/Abbreviations

TBCs – Thermal Barrier Coatings

TC – Topcoat

BC – Bond Coat

TGO – Thermally Grown Oxide

DCL – Double Ceramic Layer

LCO – Lanthanum Cerates

LZO – Lanthanum Zirconates

GZO – Gadolinium Zirconates

YSZ – Yttria Stabilized Zirconia

REO – Rare Earth Oxide

ACM – Advanced Ceramic Materials

APS – Atmospheric Plasma Spray

EPVD – Electron Beam Physical Vapor Deposition

SEM – Scanning Electron Microscopy

XRD – X-ray Diffraction

DTA – Differential Thermal Analysis

EBSD – Electron Backscatter Diffraction

CTE – Coefficient of Thermal Expansion

1. INTRODUCTION

Hot corrosion is one of the serious issues to several industrial operations, including those in electric power plants, aircraft, gas turbines, heat-treating, mineral and metallurgical processing, which run at temperatures higher than 500 °C. Strong oxidation of materials that leads to the rusting of industrial components is the second major issue for in many industrial processes. Most high temperature metals are designed to engage with the oxidizing atmosphere in a way that causes a protective oxide layer to develop for the underneath substrate protection [1]. Modern gas turbine engines, marine propulsion systems, rockets, ramjets, and aerospace jet engines require extremely high temperatures to operate efficiently. To meet demands for high thrust, power, thermal stability, and fuel efficiency, robust high-temperature materials are critical. This necessitates the development of advanced ceramics (ACM) and durable thermal barrier coatings (TBCs), which withstand harsh conditions, including thermal stresses and sulfate-induced degradation, ensuring reliability in next-generation propulsion systems. [2,3]. TBCs are getting attention due to their prominent usage in modern aero-land based gas turbine blades, combustor, hot section of jet fuel, and nuclear power plants [4]. The academic researcher and industries are cooperating to develop superior quality multi layers TBCs, especially focusing on the high temperature ceramics, advanced thermal spray technologies, and modern architecture of TBCs**.** The main attributes of TBCs include long-term thermal insulation, thermal shock resistance, hot corrosion resistance, oxidation barrier protection, metallic fatigue resistance, and thermomechanical stress resilience, ensuring reliability across multi-cycle service conditions. [5]**.**

TBCs long term durability, their integrity and high temperature efficiency was confirmed by several hours of service in long term-exposure to various continuous high temperature thermal cycles by controlling their thickness composition in the bond coat (BC), and the formation of multi-layer TBCs system by advances in ceramics and thermal spray (TS) technology [6]**.** In industries dealing with high temperatures, TBCs technology is crucial because it offers many layers of defense against chemical, mechanical and thermal attacks for underneath substrate. In the hot section of engine, TBCs are the critical protective

layers for high temperature endurance along with air cooling for the Ni-based super alloys and offer reduction in temperature up to 300 °C [7].

In the aerospace sector, rocket engine combustion chamber reaches up to 3200 °C, this enormous amount of heat (causes oxidation and thermal stresses) is managed by applying TBCs in the hot section of engine, and employing copper cooling system which circulate the hydrogen at −240 °C. During gas turbine operation, the temperature on rotor inlet exceeds 1700 °C, and on the blade more than 1000 °C which necessitates the use of high temperature ceramic materials. In automobile industry, the piston where TBCs are applied, the temperature is lower, approximately 50 °C, while inside cylinder 2400 °C for gasoline engine and 3000 °C for diesel engine are reported in the literature. Thus, the internal components of engine valves, pistons and cylinder are vulnerable to high temperature corrosion, high temperature stress, which also necessitates the use of high temperature ceramic materials. Aside from the above, TBCs also find their best application in marine industry, additive manufacturing, and hypersonic vehicle technology [8].

1.1. State of the art TBCs

TBCs consist of Ni-based super alloys which act as substrate having two main layers, the first layer is bond coat (BC) while the second layer is topcoat (TC). BC and TC layers are deposited via thermal spray process. There is another layer that forms due to the oxidation of BC during working conditions which is called thermally grown oxide (TGO) and mainly composed of BC alloying elements. The TGO layer acts as a diffusional barrier, preventing additional oxidation of the BC alloying elements while TC layer provide insulation properties. TC layers include rare earth oxides, yttria-stabilized zirconia (YSZ), and other advanced ceramic materials (ACM). TC and BC are deposited by various thermal spraying methods. The most well-known of these methods are atmospheric plasma spraying (APS) and electron beam physical vapor deposition (EB-PVD). The thickness of deposited TBCs layer is 200-300 μm, but they can tolerate temperature drop of about 200–300 °C. **Figure 1.1**. displays a photograph of a turbine blade (~10 cm long) and the developed TBCs system in the jet engine blades, which is taken from the reference [9].

The main threats to TBCs are the various decomposition mechanisms that ultimately degrade the deposited coatings over time. TBCs can be degraded over time for a

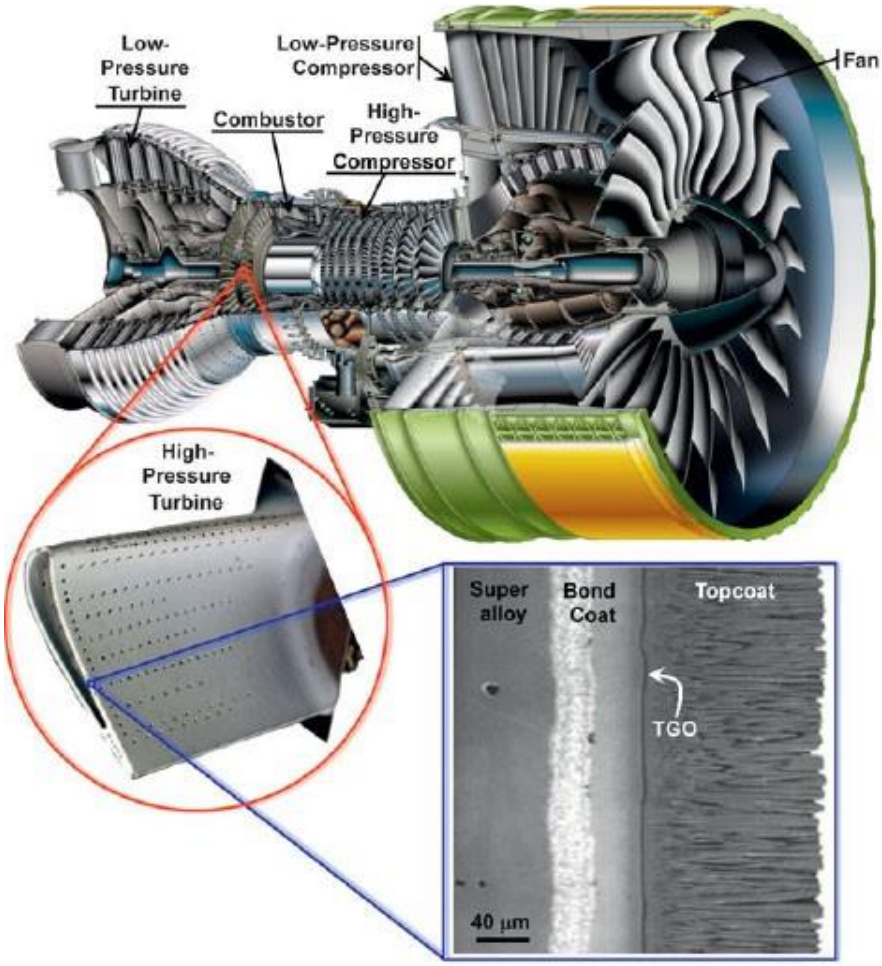

Figure 1.1. SEM view of Engine Alliance GP7200 aircraft engine, Visualization of layer of TBCs System (Engine image, courtesy of Engine Alliance; turbine blade, photograph courtesy of YXLON, and the SEM micrograph [9].

variety of reasons, including long term thermal cycle, oxidation, erosion, chemical attacks. The decomposition of TBCs can be overcome by developing more durable coating materials, improving the coating activity by function and structural change, operating materials at lower temperature to reduce thermal stress and erosion.

Nowadays, greater emphasis has been placed on research on high temperature materials. This thesis is particularly focused on investigating new methods for the preparation of coatings, in particular development of new coatings designs. The resistance of the high temperature TBCs coatings to high-temperature oxidation, hot corrosion is one of the major factors determining performance. For this reason, research and development efforts have focused on the change of the physical properties of MCrAlY bond coat by adding noble metals such as hafnium (Hf) and platinum (Pt), which have been shown to increase resistance to high-temperature oxidation and improve its overall thermal

performance. Other promising candidates for improving the performance of BC are Cr_2AlC, which has good oxidation resistance, and CoCrAlY-TiB_2, which has significantly improved antioxidation activity. CuAlNiCrFe also has good oxidation resistance and anti-diffusional properties. Maniam et al. [10] highlights the potential advantages of utilizing alumina (Al), electroplated from ionic liquids (IL), as a promising method for producing diffusion aluminides. These aluminides can be used as bond coats to improve the longevity of recently developed alloys used as base substrates. Another research explores different techniques for electrodeposition, such as modifying aluminides with intermediate electrodeposited layers and applying (Pt) electrodeposition on MCrAlZ overlays [11]. The presence of outstanding creep resistance and increased lifetime for creep in super alloys, makes them commonly used materials for high temperature applications. The prolonged high temperature effect on super alloys can produce some limitations under stress conditions. They include the non-continuous formation of Al-oxides due to insufficient amount of aluminum in super alloys. This can be overcome by Ti-aluminides [12] and overlay coating of TBCs, which includes formation of BC [13]**.** The overlay coating consists of a MCrAlY layer, where M is either Fe, Ni, Co, or a combination of these metals. A thermal grown oxide layer (TGO) is created from MCrAlY coating due to diffusion of oxygen from TC during service. The commonly used TC material is 7–8% yttria (Y_2O_3) stabilized zirconia (Zr_2O_3), due to its low heat conductivity, good chemical inertness, and high-temperature fracture toughness**.**

1.1.1. High temperature advanced ceramic materials (ACM)

To sustain durability and increase the performance of TBCs, various advanced ceramic materials (ACM) have been researched. Yttria-stabilized zirconia (YSZ), which has a high melting point, low thermal conductivity, and a good thermal expansion coefficient (CTE) match with the substrate, is one of the conventional ceramic materials that can be utilized as TBCs. Rare-earth oxides (REO), such as gadolinium oxide (Gd_2O_3), samarium oxide (Sm_2O_3), cerium oxide (CeO_2) lanthanum oxide (La_2O_3) praseodymium oxide (Pr_6O_{11}) neodymium oxide (Nd_2O_3) and europium oxide (Eu_2O_3), stabilized zirconia have been shown to have good TBCs properties and can be deposited using plasma spraying (PS). Other materials like alumina (Al_2O_3), due to its high melting point and good resistance to thermal shock, and silicon carbide (SiC), which has excellent thermal stability and low thermal expansion coefficient, are also promising TBCs materials. Hafnium oxide (HfO_2) is a

relatively new TBCs material that has shown interesting properties such as a high melting point and low heat conductivity. Atomic layer deposition (ALD) and chemical vapor deposition (CVD) are two methods that can be used to deposit it. The choice of TBCs material depends on several factors, including the operating temperature of the component, the thermal stresses, the desired thermal insulation properties, and the coating process used. The most prevalent components in rare earth oxides, including various zirconates, have been the subject of discussion for the past few years [14]**.** Comprehensive literature [15–19] available confirms that titania, zirconia, alumina, porcelain, porcelainite, yttrium aluminum garnets (YAG) - ($Y_3Al_xFe_{5-x}O_{12}$), monazite ($LaPO_4$), perovskites (ABO_3), lanthanum magnesium hexa-aluminate ($LaMgAl_{11}O_{19}$), , hafnium oxide (HfO_2), yttrium oxide (Y_2O_3), scandium oxide (Sc_2O_3), calcium zirconate ($CaZrO_3$), ceria-stabilized zirconia (CSZ), lanthanum aluminate ($LaAlO_3$), magnesium zirconate ($MgZrO_3$) and strontium zirconate ($SrZrO_3$), rare earth zirconates and even diamond may all be thought as viable TBCs materials since they have shown minimal properties which are required for thermal barrier ceramic materials. Pyrochlore $Ln_2Zr_2O_7$ (where ln= La, Nd, Sm, Gd) was revealed to be a possible substitute for YSZ because of its low thermal conductivity at higher temperatures, comparable yield stress, and lower Young's modulus. Due to its improved thermal barrier properties and stability even at temperatures above 2000 °C, lanthanum zirconate ($La_2Zr_2O_7$ - LZO) is a promising material for a variety of high-temperature treatments. LZO has low thermal expansion coefficient which makes it a good candidate for use as a buffer layer in electronic devices, particularly for the development of advanced microelectronic devices. Even though LZO mismatch with the growth of coatings prevent it from being readily substituted for normal YSZ.

1.1.1.1. Topcoat (TC)

A ceramic TC with thicknesses of 100–600 μm is usually called thermal barrier coating; it is mainly selected by the low thermal conduction, low thermal diffusivity of oxygen and molten salts, phase stability at higher temperature, high thermal shock resistance under various thermal cycles, and robust adherence to BC. Additionally, it is essential that the materials employed as TBCs demonstrate admirable erosion resistance, hot corrosion and oxidation resistances and successful surviving ability to resist calcium magnesium-alumina-silicate (CMAS) or foreign object damage (FOD) [20]**.** YSZ demonstrates favorable characteristics, including a low thermal conductivity (ranging from 2.0 to 2.3 W/m/K at

approximately 1000 °C) and even lower values (0.9–1.2 W/m/K) for porosities within the range of 10–15% [21]**.** Moreover, it has high melting point of 1680 ºC and a coefficient of thermal expansion (11×10^{-6}/K at around 1000 ºC) [22]. The YSZ exhibits stable phase at high temperatures up to 1200 °C. At temperatures above 1200 °C, the metastable tetragonal (t') phase, causing it to decompose into yttria-rich cubic (c) phase and a yttria- deficient tetragonal (t) phase due to yttria redistribution. Upon further cooling, the Y-deficient tetragonal (t) phase transforms into the monoclinic (m) phase, producing a 3–5% volume expansion. When the phase-transformed part reaches a critical value, the resulting volume expansions lead to crack initiation, propagation, and even coating spallation [22]**.** These types of coatings have strong tendency for oxidation, since oxygen diffuses through ceramic pores and oxidizes BC to TGO, to shield BC oxidation such as with MCrAlY, mullite or aluminides. This has been common practice in gas turbine to suppress TGO thickness [23]. Mullite $3Al_2O_3.2SiO_2$ has lower thermal expansion coefficient, superior oxygen resistant, and higher thermal conductivity ($k = 3.3\ Wm^{-1}K^{-1}$ at 1300 K) than YSZ, making it ideal for environmental barrier coatings (EBCs) rather than thermal insulation [22]**.** Mullite is a highly encouraging coating material for silicon carbide due to their close thermal expansion coefficients. It is reported in the literature that YSZ-mullite composite coatings abridged the crack initiation and growth with surge of temperature [24]**.** Pyrochlore materials have been widely used as thermal barrier materials, because of their excellent properties. Low thermal conductivity, a high coefficient of thermal expansion at high temperatures, a remarkable melting point, the capacity to minimize flaws, and unwavering phase stability at high temperatures are a few of these. Particularly interesting is the rare-earth pyrochlore oxide layer ($RE_2T_2O_7$), where "RE" stands for rare-earth elements like Pr, Sm, Gd, Er, La, Nd, Eu, Y, and Lu, and "T" stands for tetravalent metals such as Pb, Sn, Ti, Zr, or M. The tetravalent metal oxide TO_2 is converted into $RE_2T_2O_7$ (pyrochlore structure) by replacing 12 T atoms with RE atoms and resulting in the formation of 1/8 oxygen vacancies enabling charge neutrality (fluorite structure). A decrease in thermal conductivity is caused by modifications in the chemical bonds and the appearance of oxygen vacancies inside the structure. During the early 2000s, molecular dynamics (MD) simulations were employed to predict key properties of rare-earth pyrochlores ($RE_2T_2O_7$), including elastic modulus, thermal expansion coefficient (CTE), and thermal conductivity, as part of efforts to develop TBCs. While MD provided insights into elastic and thermal expansion behavior, thermal

conductivity predictions often required complementary experimental or theoretical methods due to phonon transport complexities. Although experimental evidence did not yet fully corroborate the prediction, their thermal conductivity varied between 1.40 to 3.04 $Wm^{-1}K^{-1}$. When compared to the collapse of La-O bonds under hydrostatic pressure, the collapse of T-O bonds occurs more slowly, making them more durable. For example, LZO (Pyrochlore) compared to 7–8YSZ, has approximately 20% lower thermal conductivity, lower Young´s modulus and equivalent mechanical strength / fracture toughness. The thermal expansion coefficient (CTE) of pyrochlore is less than 10% for temperature greater than 900 ºC, while below 900 ºC CTE is comparable to 7–8YSZ [25-26]**.** Recently, Shen et al. [27] fabricated Gd doped lanthanum cerate $(La_{1-x}\ Gd_x)_2(Zr_{0.7}\ Ce_{0.3})_2O_7$ TBCs using electron beam physical vapor deposition (EB-PVD). On the other hand, the fabrication of bilayer zirconate and cerate [28] gave rise to improved properties. These TBCs exhibit relatively high thermal durability due to several factors, including improved CTE, the formation of a feathery structure, the use of double-layer coatings (DCL), and the stabilizing effect of gadolinium substitution. The evolution of ceramic topcoats continues to favor zirconia-based ceramics due to their high toughness and good thermal matching substrates. However, recent developments involving rare-earth oxides like RE_3NbO_7 [29]**,** $RENbO_4$ [30]**,** and $RETaO_4$ [31]**,** along with rare-earth zirconates, show improved high-temperature stability and lower thermal conductivity. **Table 1.1.** presents advanced ceramic materials and their properties. Future efforts aim to enhance fracture toughness and CTE for better thermal matching and strain tolerance, ultimately leading to longer lifetimes in these coatings.

Table 1.1. Promising properties of next generation ACM

ACM	Ref.	Properties
ZrO_2	[35]	T_m = 2973 K D_{th} = 0.43 ×10^{-6} m^2s^{-1} (1273 K) E = 21 GPa (1373 K) α = 15.3×10^{-6} K^{-1}(1273 K)
8YSZ	[35]	T_m = 2973 K D_{th} = 0.43 ×10^{-6} m^2s^{-1} (1273 K) λ = 2.20-2.50 $Wm^{-1}K^{-1}$ E = 40 GPa (293 K) α = 10.7×10^{-6} K^{-1} (293-1273 K) ν =0.22
Gadolinium zirconate -GZO $Gd_2Zr_2O_7$	[36-37]	T_m = 2600-2725 K α = 9–11.9×10^{-6} K^{-1} (1000 °C)

		$\lambda = 1.6\ Wm^{-1}K^{-1}$ (1000 °C) E = 75 GPa (293 K)
Lanthanum hexaaluminate ($LaMgAl_{11}O_{19}$)	[38-39]	T_m = 800-2300 K $\alpha = 9.6\times10^{-6}\ K^{-1}$ (30-1000°C) $C_p = 0.86\ Jg^{-1}K^{-1}$ (1273 K) $\lambda = 2.6\ Wm^{-1}K^{-1}$ (1273 K)
Yttrium oxide (Y_2O_3)	[39-40]	T_m = 2698 K $\alpha = 8.6\text{-}9\times10^{-6}\ K^{-1}$(1170 K) $\lambda = 13.6\ Wm^{-1}K^{-1}$ (300 K) E = 120-170 GPa (300 K)
Yttrium aluminium garnet (YAG)	[38]	T_m = 2243 K E = GPa $\alpha = 9.1\times10^{-6}K^{-1}$ $\lambda = 3.0\ Wm^{-1}K^{-1}$ (1273 K)
Hafnium oxide (HfO_2)	[41-42]	T_m = 3031 K $\alpha = 5.5\text{-}6.5\times10^{-6}$/°C (298-1273 K) E = 200-400 GPa $\lambda = 2.6\text{-}3.6\ Wm^{-1}K^{-1}$ (298 K)
lanthanum zirconate -LZO $La_2Zr_2O_7$	[36] [43]	T_m = 2573k $D_{th} = 0.54\times10^{-6}\ m^2\cdot s^{-1}$ (1273 K) $\lambda = 1.56\ Wm^{-1}K^{-1}$ (1273 K) E = 175 Gpa (293 K)
Neodymium Zirconates-NZO $Nd_2Zr_2O_7$	[44-45]	T_m = 2593-2580 K $\alpha = 9.6\times10^{-6}\ k^{-1}$ (1000 °C) $\lambda = 0.4\text{-}2.5\ Wm^{-1}K^{-1}$ (1000 °C) E = 151GPa
Samarium zirconate -SmZO $Sm_2Zr_2O_7$	[35],[44] [46]	T_m = 2770-2299 K $\alpha = 14.55\times10^{-6}\ k^{-1}$ (1273 K) $\lambda = 1.6\ Wm^{-1}K^{-1}$ (298.15 K) E = 231GPa
CeO_2	[47]	T_m = 2873K $D_{th} = 0.86\times10^{-6}m^2s^{-1}$ (1273 K) $\alpha = 13\times10^{-6}k^{-1}$ (293-1500 K) $\lambda = 2.77\ Wm^{-1}K^{-1}$ (293 K) E =172 GPa (293 K) $C_p = 0.47\ Jg^{-1}K^{-1}$(1273 K)
Scandium oxide (Sc_2O_3),	[40]	T_m = 2758 K $\alpha = 8.3\times10^{-6}\ k^{-1}$ (293 K) E = 450 GPa $\lambda = 9\text{–}12\ Wm^{-1}K^{-1}$ (293 K)
Ceria-stabilized zirconia (CSZ)	[40],[48]	T_m = 2673- 2973 K $\alpha = 10\text{-}12\times10^{-6}$ /°C E = 200-300 GPa $\lambda = 2\text{-}3\ Wm^{-1}K^{-1}$ (293 K).
Lanthanum Cerates-LCO $La_2Ce_2O_7$	[49]	T_m = 2573 K $D_{th} = 0.19\times10^{-6}\ m^2s^{-1}$

		$\lambda = 0.6\ Wm^{-1}K^{-1}$ $\alpha = 12.3\times10^{-6}\ k^{-1}$ (573-1473 K) $C_p = 0.43\ J^{-1}\ k^{-1}$
Lanthanum aluminate ($LaAlO_3$),	[50-51] [36]	$T_m = 2353$ K $\alpha = 9.2\times10^{-6}\ K^{-1}$(1273 K) $\lambda = 20\text{-}25\ Wm^{-1}K^{-1}$ E = 320GP Average (293 K)
Magnesium zirconate ($MgZrO_3$)	[52-53]	$T_m = 2860$ k $C_p = 400\text{-}600$ J/(kg·K). $\alpha = 9\text{-}12\times10^{-6}\ K^{-1}$(293 K) $\lambda = 3.5 Wm^{-1}K^{-1}$ (1073 K) E = 200-300 GPa (293 K)
Strontium zirconate ($SrZrO_3$)	[35],[54]	$T_m = 3073$ k $\lambda = 2.3\ Wm^{-1}K^{-1}$ (1200 K) E = 88 GPa (1200 K) $\alpha = 11\times10^{-6}\ K^{-1}$ (300–1273 K)
Calcium zirconate ($CaZrO_3$)	[55-56]	$T_m = 2803$ K $\lambda = 2.5\ Wm^{-1}K^{-1}$ $\alpha = 8.4\text{-}8.9\times10^{-6}\ K^{-1}$ (1273 K)
Barium zirconate ($BaZrO_3$)	[4]	$T_m = 2963$ K $\lambda = 3.42\ Wm^{-1}K^{-1}$ (1273 K) $\alpha = 8.1\times10^{-6}\ K^{-1}$ (1273 K) E = 181 Gpa (293 K) $D_{th} = 1.25\times10^{-6}\ m^2s^{-1}$
Rare-Earth Tantalates $YTaO_4$ $NdTaO_4$ $GdTaO_4$ $YbTaO_4$ $EuTaO_4$	[57-59]	$\lambda = 1.5\ /(Wm^{-1}K^{-1})$ E= 140 GPa $\lambda = 1.41\ /(Wm^{-1}K^{-1})$ at 1073 K E = 178GPa $\lambda = 1.701.41\ /(Wm^{-1}K^{-1})$ at 1173 K E = 154 GPa $\lambda = 1.65\text{–}3\ 7.6\ /(Wm^{-1}K^{-1})$ (1473 K) E = 122 GPa $\lambda = 1.26$ (1173 K) E = 175 GPa
Rare-Earth Niobates $NdNbO_4$ $SmNbO_4$	[60]	$\lambda = 2.0\ Wm^{-1}K^{-1}$ (1273 K) $\alpha = 11.80\times10^{-6}\ K^{-1}$ (1273 K) E =108 GPa $\lambda = 2.05\ Wm^{-1}K^{-1}$ (1273 K) $\alpha = 10.86\times10^{-6}\ K^{-1}$ (1273 K)

$GdNbO_4$		E = 120 GPa λ =1.66 $Wm^{-1}K^{-1}$ (1273 K) α =10.30 $\times 10^{-6}$ K^{-1} (1273 K) E =131 GPa
Symbols In the Table:1 T_m= Melting point, D_{th}=thermal diffusivity, α= thermal expansion coefficient, λ= thermal conductivity, E=Young's modulus, C_p= heat capacity		

1.1.1.2. Bond coat (BC)

The bond coat acts as a pre-coating contact, promoting adhesion between the substrate and topcoat, and enhancing the structural rigidity of the TBC. The bond coat is 100–300 μm layer of MCrAlN intermetallic alloy, where M is a metal from VIIIB group (M=Ni, Co, Fe, or mixture of these), and N a metal from IIIB and IVB groups (N = Y, Zr, Hf, Yb, or mixture of these). TGO, with a thickness of 1–10 μm, is a hard layer formed between TC and BC during operation at high temperature. Alpha-alumina (α-Al_2O_3) is the main component in TGO, which shield the BC against oxygen diffusion and act as barrier. During TBCs production and operation, oxygen diffuses through the topcoat to form the TGO layer. Overall, bond coat material studies and developments are essential to enhancing the functionality and lifespan of TBCs. The addition of noble metals, as well as the use of alternative materials such as Cr_2AlC and CoCrAlY-TiB_2, are promising in improving the high-temperature oxidation resistance of bond coats. Further research is needed to develop and optimize these materials for practical applications [32].

Rabieifar et al. reviewed [33] reviewed the research related with β- (Ni, Pt) Al as well as Pt-modified γ–γ′ bond coats, that have gained prominence in more recent times. Pt modification in bond coats positively affected high-temperature oxidation and hot corrosion resistance, leading to the commercial use of Pt-modified β bond coats like RT22, SS82A, and MDC150L. High-Entropy Alloys (HEAs) [34], known for their strength and stability, hold promising results as BC materials in high-temperature applications. HEAs, due to their unique properties, can enhance hot corrosion resistance by promoting the formation of a continuous and dense thermally grown oxide (TGO). Additionally, they help in controlling diffusion between the bonding layer and the substrate at elevated temperatures.

1.2. Research gap

TBCs are facing several challenges that limit their effectiveness and durability such as thermal cycling durability, erosion resistance, oxidation resistance, bond coat degradation, manufacturing and repair cost. TBCs are prone to structural damage and performance deterioration due to several factors, including externally applied damage like foreign object damage (FOD), temperature and gradient effects, sintering, erosion by crystalline calcium alumina silica (CMAS), corrosion, and oxidation.

The resilience of the TBCs system depends on the resistance to frequent degradation mechanisms. The degradation of TBCs occurs due to changes in the following issues of TBCs: (1) growth of the overlay TGO on top of MCrAlY, (2) ability of ceramic coat for elevated temperature sintering, (3) alteration in the ceramic phase due to continuous service at high temperature (4) coating layers and substrate CTE mismatch can cause thermal strains (5) hot corrosion by melted salts, like CMAS (CaO-MgO-Al2O3-SiO2) and ashes. Devoted scientists and engineers are working hard to overcome these challenges by developing novel coating materials, improving coating methods, and better understanding the underlying causes of degradation.

Ongoing research in TBCs is focused on improving durability. With the same purpose, this research was designed based on two-phase thermal barrier coatings, usually called dual phase TBCs. Dual phase TBCs offer much lower thermal conductivity, which is the main requirement for ACM, more resilience and durability in long term exposure under extreme conditions. Dual phase TBCs provide enhanced thermal properties as compared to conventional nonceramic layer or double ceramic layer (DCL). In a dual phase system, heat flow is resisted by mutual phases and provide better insulation properties where radiation effect is stronger. Low thermal conductivity phases, such as pyrochlore (rare earth zirconates), play an important role in lowering thermal conductivity, while features like porosity and inter-splat boundaries help to reduce stress within the coating, making it more durable under harsh conditions. The literature on the composite dual phase system of Sm_2ZrO_7+YSZ [61] provides much deeper details about lowering the thermal conductivity through structure and property relation of deposited coatings.

1.2.1. Research questions

The lowering of thermal conductivity and increasing durability is a research gap still existing, which makes new research on how these dual phases behave under hot corrosion-pure oxidation at micro level very actual. The requirements for long term exposure at high temperature for several hours, and resistance to sulphate environment, are not explored in the literature for the dual phase system. The main questions that were taken into consideration in this thesis are!

1. Are two phase systems (pyrochlore and zirconia) stable at high temperatures?
2. How dual phase systems will degrade under an environment of a corrosive Na_2SO_4 salt (source from fuel impurities, airborne salt), which melts at relatively low temperatures?
3. How the presence of dual phases, including interfaces and boundaries, affects the coating's stability and resistance to phase changes or degradation at high temperatures with Na_2SO_4 exposure?

Exploring these questions could lead to new breakthroughs in dual phase TBCs technology, helping us designing coatings with even better performance for high-temperature applications. While it remains accurate that the high-temperature corrosion mechanism in salt deposits, such as Na_2SO_4 and V_2O_5, takes place independently of any additives, the topic of elevated-temperature corrosion processes in different multilayer coatings lacks comprehensive coverage in existing literature. This holds true, except for composite coatings that include ceramic layers featuring dual-phase characteristics. This is particularly important for dual-phase composite coatings, as they are not well discussed in the literature. This study aims to address the literature gap on research of dual-phase composite coatings under hot corrosion, which are of particular significance due to their unique properties and potential applications.

1.3. Thesis outline

The use of two-phase composite ceramic layers of the 8YSZ+$Ln_2(Zr/Ce)_2O_7$ type may constitute a new direction in the development of TBCs, and their phase stability will be determined by the type of elements used in the $A_2B_2O_7$ compounds, i.e. rare earth

oxide A and element of the B type. The most advantageous solution will be the use of lanthanum zirconates, which are characterized by the highest initiation energy of the pyrochlore-fluorite transformation, which guarantees the highest stability of the phase composition.

Exploring these details could lead to new breakthroughs in dual phase TBCs technology, helping us design coatings with even better performance for high-temperature applications. While it remains accurate that the high-temperature corrosion mechanism in unadulterated salt deposits, such as Na_2SO_4 and V_2O_5, takes place independently of any additives, the topic of elevated-temperature corrosion processes in different multilayer coatings lacks comprehensive coverage in the existing literature. This holds true, except for composite coatings that include ceramic layers featuring dual-phase characteristics. Particularly important for dual-phase composite coatings, as they are not discussed in literature well. This study aims to address the lack of literature and research on dual-phase composite coatings under hot corrosion, which are of particular significance due to their unique properties and potential application.

Chapter one – Introduction

This chapter sets the stage for research by introducing thermal barrier coatings (TBCs), their importance for high temperature applications, morphology in terms of bond coat (BC) and topcoat (TC). It also explains advanced ceramic materials (ACM) available in the literature for the production of BC and TC. The motivation and context emphasizes the need for advanced high-temperature coatings, being introduced the main research questions and research Gap. The chapter also describes the hypothesis on dual phase systems and sets the theme of this PhD research.

Chapter two – literature review

This chapter reviews existing literature on hot corrosion. It explores hot corrosion mechanisms, including their types (e.g., Type I and Type II), and explains the degradation routes of ceramic materials under aggressive environments. Additionally, it discusses recent advancements in zirconate-based ceramics (lanthanides of zirconates), highlighting their significance and the strategies to optimize their properties (e.g., thermal stability, phase stability) for high-temperature applications. Finally, the modern architecture of TBCs is discussed.

Chapter three – Experimental Procedure

This chapter describes the experimental methods and materials used in the research, with a focus on the atmospheric plasma spray of LCO, LZO, YSZ and GZO systems. It also outlines the main characterization techniques employed, like SEM, EBSD, X-ray diffraction and DTA analysis. Furthermore, it discusses the performed hot corrosion and pure oxidation tests.

Chapter four – LZO-based TBCs

This chapter details the findings from under-reviewed research based on the LZO+YSZ-based dual phase TBCs system. It identifies the new degradation routes, thermal stability of dual phase system under hot corrosion and pure oxidation. The effect of LZO in YSZ at high temperature is discussed in detail.

Chapter five – GZO-based TBCs

This chapter details findings from published research based on the GZO+YSZ-based dual phase TBCs system. It identifies the new degradation routes, thermal stability of dual phase system under hot corrosion and pure oxidation. The effect of GZO in YSZ at high temperature is discussed in detail.

Chapter six – LCO-based TBCs

This chapter details findings from under- reviewed research based on the LCO+YSZ-based dual phase TBCs system. It identifies the new degradation routes, thermal stability of dual phase system under hot corrosion and pure oxidation. The effect of LCO in YSZ at high temperature is discussed in detail.

Chapter six – Conclusion and Future trends

The concluding chapter synthesizes the findings, discussing the contributions of dual phase system in the production of advanced TBCs. This chapter marks the final conclusion about using dual phase TBCs, as an alternative way for the TBCs and the new degradation routes of TBCs. It revisits the research questions, outlines the achievements of the study, and suggests directions for future research to further advance the field.

2. LITERATURE REVIEW

2.1. Introduction to hot corrosion

The TBCs are prone to degradation due to several corrosive species such as sodium (Na), magnesium (Mg), vanadium (V) and sulfur (S)-based compounds. These compounds are the impurities from low quality fuel (hydrocarbons) and air pollutants from the environment. Hot corrosion is a major contributor to the economic losses in the industrial sector due to extra maintenance or forced downtime. The industry widely acknowledges that the formation of various salts on high-temperature equipment is the main cause of hot corrosion. High temperature environment promotes the formation of liquid salt, and the literature suggests that sodium sulfate (Na_2SO_4) or its mixtures with other sulphates like magnesium (Mg), potassium (K), calcium (Ca), and vanadium (V) [62] are common corrosive species, resulting from low-quality fuel, air aerosols, and oxidation from the combustion processes in engines. The elements formed include sodium vanadate, potassium vanadate, calcium vanadate, and simple or complex vanadate's as presented in equations 1–3. Impurities may develop during the export, extraction, and refining of fuel [63]**.** When such corrosion environment pure salts or salt mixture interacts with TBCs, several degradation process initiate. YSZ conventional TC in the presence of V_2O_5 with Na_2SO_4, vanadium interacts with yttrium, creating yttrium vanadate (YO_4), causing zirconia destabilization and the development of monoclinic zirconia (m-ZrO_2). In addition, the corrosive reagent $NaVO_3$ increases nuclear mobility and accelerates YSZ's yttrium depletion, which ultimately depletes Y_2O_3's zirconium lattice. The phase transition from tetragonal zirconia to monoclinic zirconia occurs during cooling, causing a volume elongation of about five percent, escorting towards spallation and destruction of YSZ TBCs. The corrosive environment created by combustion by-products, including water vapor, Na_2SO_4 and V_2O_5, is of great concern. These problems are further complicated by the presence of molten calcium-magnesium-alumina-silicate (CMAS), which enters the gas turbine through the intake air and comes from sources such as soil, ash from volcanoes, sandy soils, and debris from airfields [64]. Although these corrosive substances can individually degrade materials

at high temperatures when mixed during combustion, their melting point decreases due to the formation of eutectics, creating an even more aggressive environment. CMAS corrosion in gas turbine engines occurs from the ingestion of silicate particles, where even a low concentration results in significant ingestion of dirt. A turbojet engine that sucks 300 m^3 of air per second at an altitude of 11 km can consume about 110 kg of dry air. Particulate filters can remove large particles, but smaller particles (less than 80 μm) still reach TBCs. These particles, which pass through combustion chambers at temperatures up to 1650 °C, melt and adhere to the surfaces of the TBC, causing degradation. Despite the filtration effort, the high airflow required for the engines prevents complete removal, making CMAS corrosion a persistent problem [65–66]. In general, the great variety of vanadium salts found in ash deposits is the consequence of a chemical interaction between two major components, V_2O_5 and Na_2SO_4. The resultant vanadium salt, however, may vary in aggressiveness depending on its molar ratio and temperature.

$$xNa_2SO_4 + yV_2O_5 \rightarrow xNa_2O{\cdot}yV_2O_5 + xSO_3 \quad (1)$$

$$xK_2SO_4 + yV_2O_5 \rightarrow xK_2O{\cdot}yV_2O_5 + xSO_3 \quad (2)$$

$$xCaSO_4 + yV_2O_5 \rightarrow xCaO{\cdot}yV_2O_5 + xSO_3 \quad (3)$$

The literature widely discusses how low-quality fuels, alkali and alkaline impurities, and induced impurities from the fractional distillation process during refining combine to create a hot corrosion environment in molten salt at high temperatures. In addition to the fuel grade, the combustion fuel frequently contains sulfur ranging from 0.1wt. percent to 1wt. percent (or more) as well as sulfate salts and other sulfur species from marine air absorbed into the hot area of the turbine engine. Hot corrosion involves both oxidation and sulphuration. **Table 2.1.** [67-68] shows the melting points of potential corrosive sulfates. Binary and tertiary systems lower their melting point depending on Van der Waals interaction. High temperatures and the presence of V_2O_5 or mixture of two sulphate salts intensify these reactions. Impurities lower the melting point and increase the boiling point, stabilizing the liquid phase and making it more energetically favorable. This extends the liquid range to lower temperatures and the gaseous molecules to higher temperatures. The existence of various sulfate salts forms several eutectic phases and lowers the liquification point at high temperature [69]. As it can be seen from Table 1 in binary or ternary systems, the presence of other compounds can change structural properties as compared to pure salt. That’s why the mixture of salts leads to a low eutectic point than its pure form, which is the

temperature at which eutectic compounds form in the transition from solid to liquid state. This type of effect was also observed for various alloying elements of TBCs materials, such as **Figure 2.1.** [70]. The employment of differential thermal analysis (DTA) showed the creation of eutectic compounds at lower temperatures upon the combination of sodium sulphate with different ceramic materials, including samarium stabilized by zirconia and hafnia oxide, as well as yttria-stabilized by zirconia and cerium oxide. The eutectic point of these multi-phase compounds was observed to decrease by 35–40 °C, indicating a lower melting temperature compared to the pure sodium sulphate. This suggests that the addition of these ceramic materials may have a catalytic effect on the melting behavior of the compounds. The lowest melting point was observed with the composition of the dual-phase ceramic of samarium stabilized by zirconia and hafnia oxide with the sulphate salts, indicating that this combination may have unique properties that make it particularly effective for low-temperature eutectic formation, and can accelerate the degradation process upon corrosion. The observed analysis also provides valuable insights into the formation of low-temperature eutectic point in these compositions and can be used to optimize the composition of these materials for various applications specially to corrosion mitigations.

Table 2.1. The melting temperature for common sulphate salts [67-68]

Corrosive salts	**Melting Temperature (T_m)**
Na_2SO_4	884 °C
K_2SO_4	1069 °C
$Na_2S_2O_7$	400.9 °C
$K_2S_2O_7$	325 °C
$Na_3Fe\ (SO_4)_3$	624 °C
$K_2Fe\ (SO_4)_3$	618 °C
Na_2SO_4–$CoSO_4$	575 °C
K_2SO_4–$CoSO_4$	535 °C
$CaSO_4$	1460 °C
$MgSO_4$	1124 °C
$CoSO_4$	735 °C

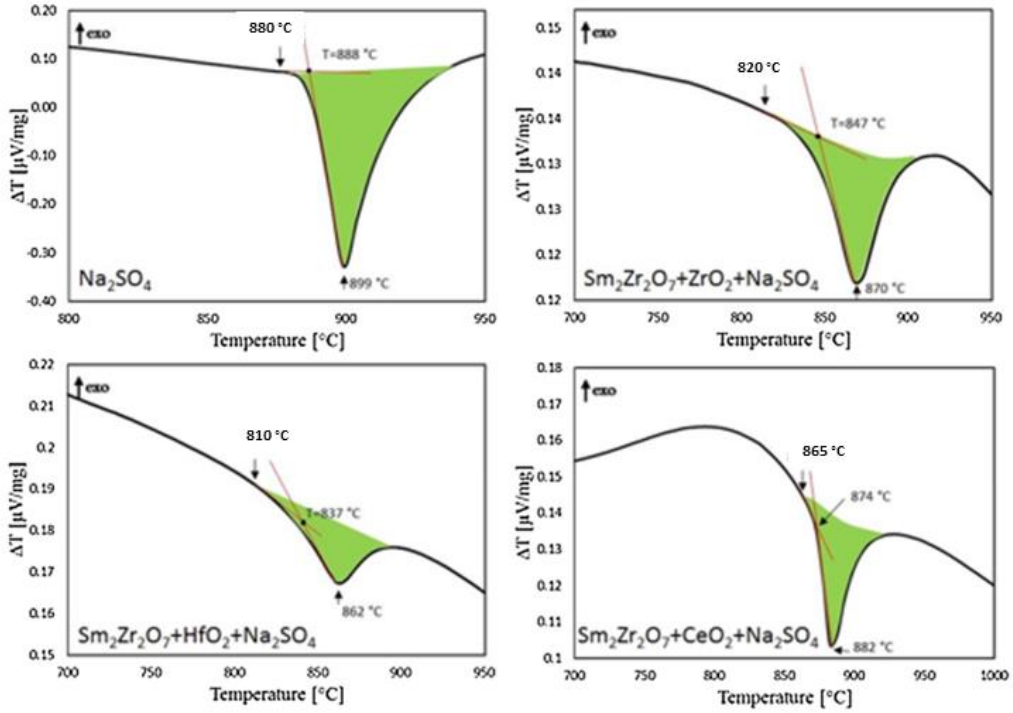

Figure 2.1. Differential thermal analysis of pure sodium sulphate, samarium zirconates and its alloying elements [70].

2.2. Type I and Type II hot corrosion

Type-I hot corrosion at high temperatures and Type-II hot corrosion at low temperatures are the two main types of hot corrosion conditions. The standard for both types is based on the melting point of sodium sulfate, with Type-I referring to temperatures above 884 °C and Type-II referring to temperatures below the melting point of sodium sulfate. As sodium sulfate splits into its acidic and basic ions in equation 4, this is known as Type-I corrosion.

$$Na_2SO_4 \rightarrow Na_2O\ (\text{Basic}) + SO_3\ (\text{Acidic}) \qquad (4)$$

The presence of several salts in corrosive environment, such as salt mixture, decreases the eutectic point of binary or ternary systems typically resulting in Type-II corrosion [71]. Type I and Type II hot corrosion can both be better understood with the help of Arrhenius equation (5), which provides the formula for the temperature dependence of reaction rates. Thermodynamic stability of corrosion products and kinetical studies of various ceramics is required to understand the degradation mechanism in the specific ceramic materials. what's are the various aspects that need to be considered while studying

degradation mechanism in ceramic materials and describe the aspect of thermodynamics and kinetics studies.

$$k = Ae - \left(\frac{E_a}{RT}\right) \qquad (5)$$

where: k (should be same letter as in Equation) symbolizes the reaction's rate constant, whereas A is a pre-exponential factor, influenced by the frequency of molecular collisions and the likelihood of them causing a reaction. *Ea* corresponds to the activation energy, denoting the minimal energy essential for the reaction's initiation. *R* stands for the gas constant, and *T* represents the temperature expressed in Kelvin.

The degradation of alumina ceramics in aqueous environments is a common example that explains the importance of thermodynamics and kinetics. Alumina ceramics are commonly used in various applications due to their excellent mechanical and electrical properties. However, they are susceptible to degradation in aqueous environments due to hydrolysis reactions, which can lead to the formation of amorphous aluminum hydroxide and the dissolution of the ceramic material. Thermodynamic calculations can be used to predict the stability of aluminum hydroxide and the conditions under which it is likely to form. As an illustration, under a pH of 7, the thermodynamic balance supports the generation of aluminum hydroxide. This process is accompanied by a modification in Gibbs free energy amounting to -744.7 kJ/mol. This indicates that the formation of aluminum hydroxide is thermodynamically favorable under these conditions. Kinetic studies can be used to determine the rate at which the hydrolysis reaction occurs and the factors that influence the rate. For example, studies have shown that the rate of hydrolysis of alumina ceramics increases with increasing temperature and pH, as well as with the presence of impurities in the aqueous environment. At 90 °C and pH 7, the rate constant for the hydrolysis of alumina is approximately 2.6 x 10^{-8} mol/(m^2s). The transformation from the T phase to the M phase is thermodynamically disfavored at room temperature and low stresses, because the T phase has a lower Gibbs free energy than the M phase. Therefore, the formation of the M phase in the TBCs requires a driving force, such as high-temperature exposure or mechanical stresses, to overcome the thermodynamic barrier and facilitate the phase transformation. In addition to the thermodynamic stability of the phases, the kinetics of the phase transformation also play a critical role in TBCs degradation. The speed at which phase transformation occurs relies on multiple factors, encompassing temperature, stress, composition, and the

microstructure of the coating. For example, higher temperatures and stress can accelerate the phase transformation, leading to faster degradation of the TBCs.

The mechanism of hot corrosions that are induced sulfates, chlorides, and vanadate's involves the formation of molten salts on the surface of the material, which then react with the material to form metal oxides and sulfides. The rate of hot corrosion is strongly influenced by temperature and can be described using the Arrhenius equation [72-73].

The Arrhenius equation can be used to calculate the rate constant of the reaction that causes hot corrosion and can be used to forecast how temperature will affect the rate of corrosion. Higher temperatures increase the rate of corrosion, as they increase the likelihood of the formation of molten salts, thus the reaction requires less activation energy to take place. However, the Arrhenius equation is only applicable within a certain temperature range and may not accurately predict the rate of corrosion at very high temperatures. There is Type I hot, high-temperature corrosion/sulfidation as a result of basic fluxing, which dissolves oxide scales that typically protect high temperature component surfaces. Molten sulfate deposits build up on these surfaces and lead to the corrosion of the alloy beneath. This type of corrosion is identified by a smooth base alloy oxide interface and a continuous, uniform depletion zone below the oxide scale that contains discrete sulfide particles [74]. Type I hot corrosion is caused by molten sodium sulfate, and a fundamental fluxing technique involves creating metal sulfides to increase the Na_2O activity in the molten sulfate. Type I hot corrosion come to mind at high temperatures, typically above 500 °C, when metal surfaces are exposed to molten salts, such as sodium sulfate (Na_2SO_4) or potassium sulfate (K_2SO_4). These salts are commonly found in industrial environments, such as gas turbines, steam generators, and boilers. As shown in **Figure 2.2.** below, the corrosion rate is extremely high from the start of the corrosion process when the salt deposits on the metal surface are in a liquid state. This is because the molten salt is highly corrosive and attacks the metal surface aggressively, leading to rapid degradation. The kinetics of this corrosion process are mainly linear, meaning that the corrosion rate remains constant over time. In the presence of salt, the melting point of the salt is an important factor to consider. When the temperature surpasses the melting point, the salt transitions into a liquid state, causing the corrosion rate to accelerate significantly in contrast to when the salt is in solid form.

To illustrate, consider the scenario of nickel (Ni) corrosion exposed to Na_2SO_4 at 900 °C, exceeding the melting point of Na_2SO_4 at 880 °C. In this context, the corrosion rate

exhibits rapid escalation right from the outset, comparable to the oxidation of Ni in the absence of salt, where the corrosion rate is minimal. Minor quantities of sulfur combined with sodium, magnesium, or potassium have the potential to generate sufficient Na_2SO_4 or K_2SO_4, thereby triggering corrosion. Unfiltered air could contain concentrations of up to 2600 ppm of Na_2SO_4, 19,000 ppm of NaCl, along with other compounds originating from saltwater, thereby exacerbating the corrosive impact of the environment on components of marine gas turbines. Once the protective oxide scales are compromised, the underlying alloy or coating becomes vulnerable to swift oxidation and sulfidation. Particularly at temperatures surpassing 950 °C, the dominant mechanism responsible for the failure of coating materials shifts to oxidation [75]. **Figure 2.2.** revealed that Type II hot corrosion occurs at relatively lower temperatures, typically below 500 °C, and is characterized by an initial slow corrosion rate followed by a sudden increase in the corrosion rate after an incubation period. The delay in onset is a result of the development of a shielding oxide layer on the metal surface, effectively restraining the corrosion process. However, once this oxide layer is breached, the corrosion rate increases rapidly. The fundamental approach to enhance fluxing involves elevating the Na_2O activity within the molten sulfate via the generation of metal sulfides. Even minor concentrations of sulfur combined with sodium or potassium can yield adequate Na_2SO_4 or K_2SO_4, or form their eutectic mixtures, setting off the corrosion sequence. The initial phase entails a period of incubation during which the conditions mature until the protective scale dissolves, allowing the direct penetration of the melt to the underlying alloy. Upon the breach of the protective oxide scales, the substrate alloy or coating becomes susceptible to swift oxidation and sulfidation. Beyond approximately 950 °C, the prevailing process causing material deterioration shifts towards oxidation. In the early-stage oxidation process continues, the formation of protective oxide on the metal, as it advances oxidation by products dissolves salt. Due to this relative mixture, eutectic formation that transition to molten state and triggered a rapid upsurge in the corrosion reaction. As an illustration the situation in the Ni corrosion starts around 700 °C with robust Na_2SO_4 deposition. The corrosion reaction initiates, as Ni undergoes oxidation, formation of NiO, formation of other byproducts like SO_2, $NiSO_4$ is produced. Throughout this early stage, Na_2SO_4 remains in the solid state, causing the corrosion rate to be gradual.

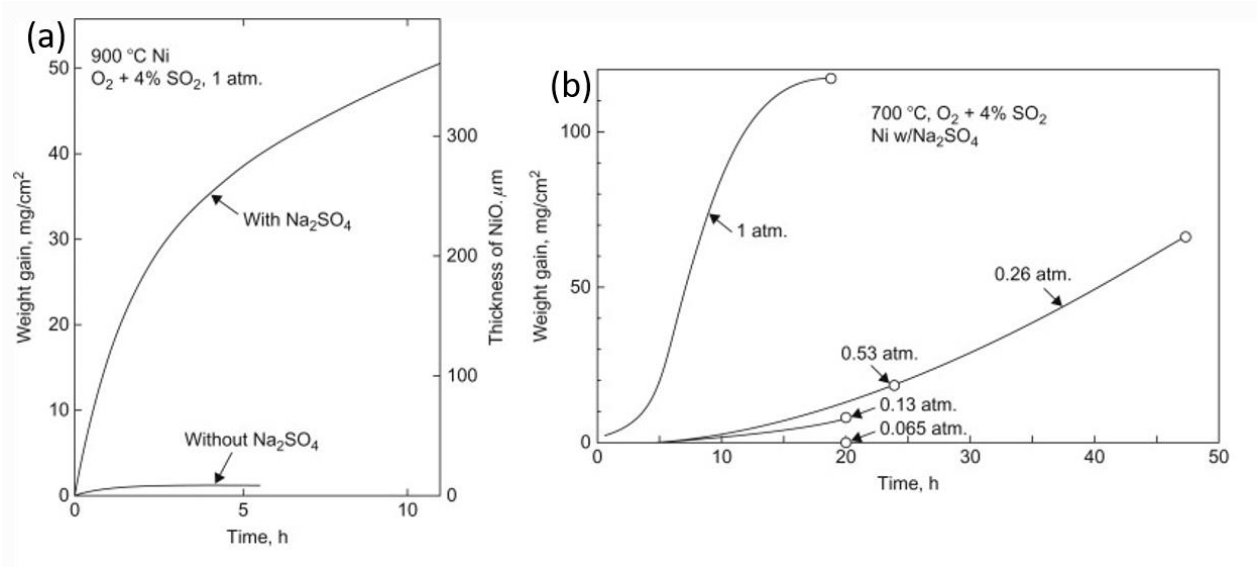

Figure 2.2. (a) Type 1: Corrosion of nickel, with and without the presence of the salt Na_2SO_4 in 1 atm. O_2+4% SO_2 at 900 °C. (b) Type 2: Corrosion of nickel at 700 °C, covered with Na_2SO_4 deposit (2.5 gm/cm^2) in 1 atm. O_2+4% SO_2 at different total gas pressures [75]

However, the oxidation byproducts interact with salt deposit, begin to combination of Na_2SO_4 and $NiSO_4$ characterized by lowering melting point than the pure salt, the corrosion rate suddenly increase. This phenomenon is graphically described in **Figure 2.2.** Ceramic coatings are utilized to prevent Type I processes, which initiate at high temperatures. When the temperature of the TBCs increases to between 700 °C and 925 °C, molten salts such as sodium and vanadium, that have accumulated on the TBC's top layer, undergo a phase transition. This results in an interaction with the Y_2O_3 phase of TBCs components, leading to degradation of the TBCs as described in equations 1, 2, 3, 6, and 7. The stabilization process of zirconia triggers a shift from its tetragonal phase to a monoclinic one. This transformation worsens the harm caused on the structural integrity of yttria-stabilized zirconia, accelerates its corrosion, and induces alterations in the coating's volume. Failure of TBCs, particularly due to spallation, stems from changes in the oxide layers' mass, either involving an increase or a reduction.

$$t\text{-}ZrO_2(Y_2O_3) + 2NaVO_3 \rightarrow m\text{-}ZrO_2 + 2YVO_4 + Na_2O \quad (6)$$

$$ZrO_2\,(Y_2O_3) + V_2O_5 \rightarrow ZrO_2\,(m) + 2YVO_4 \quad (7)$$

The literature mostly discusses the hot corrosion process of traditional coatings based on YSZ or innovative coating types based on rare earth zirconates/cerates in the setting of liquid Na_2SO_4 salt deposits supported by V_2O_5. This is because this specific environment is known to be extremely aggressive and is often used as a benchmark for studying hot

corrosion resistance [76-77]. Literature comprehensively describes [78-79] the impurities within the fuel products, that transform into acidic and basic oxide during combustion process in the engine. During the combustion process sulfur compounds and oxides engage in Lewis's reaction, which give rise to sulfate, vanadium salts lowering melting point and capable of deposition on the TBCs. In the case of YSZ, studies have shown that sulfate salt deposits, such as Na_2SO_4, can be present in the hot corrosion environment. Nevertheless, the presence of sulfate salt deposits does not compromise the stability of metastable t' ZrO_2 within the TBCs. An effective approach to impede TBCs degradation resulting from interactions with liquid salt deposits, particularly those containing V_2O_5, is to hinder the intrusion of liquids into the ceramic layer via pores and fissures. This objective can be realized by refining the microstructure and porosity of the TBC, alongside the application of supplementary barrier layers or coatings onto the TBCs itself. A thorough summary of the hot corrosion processes for TBCs based on zirconium oxide modified by yttrium oxide was provided by Jones' study [80-81]. The study discovered that sulfate salt deposits, such as Na_2SO_4, which can build up on the TBCs surface in high-temperature settings, are typically composed of sulfur. Even under long-term working conditions, the presence of sulfate salt deposits has little impact on the stability of metastable t' ZrO_2 in the TBCs. Instead, reaction 8 takes place, creating yttrium sulfate, or $Y_2(SO4)_3$. Reaction 8 (**Table 2.2.**) involves the reaction of $ZrO_2(Y_2O_3)$ with sulfur trioxide (SO_3) gas, which results in the formation of yttrium sulfate and monoclinic ZrO_2(m-ZrO_2). The formation of yttrium sulfate in the TBCs is a relatively benign process that does not significantly affect the TBC's protective properties. Several studies [82-83] also emphasize that YVO_4 crystals that formed during chemical reaction are main corrosion products which transform phase and generate stress that leads to coatings failure. The author proposes to add other possibilities of formation of salts, the degradation of zirconates, and their reaction mechanism with zirconates. These reactions are thermodynamically favorable.

Table 2.2. Reaction during combustion process at high temperature

$2\ Na + ½\ O_2 \rightarrow Na_2O$	Acidic (1)
$S + O_2 \rightarrow SO_2$; $SO_2 + ½\ O_2 \rightarrow SO_3$	Basic (2)
$SO_3 + Na_2O \rightarrow Na_2SO_4$	Salt Formation (3)
$2\ K + ½\ O_2 \rightarrow K_2O$	Acidic (4)

$S + O_2 \rightarrow SO_2$; $SO_2 + ½\ O_2 \rightarrow SO_3$	Basic (2)
$SO_3 + K_2O \rightarrow K_2SO_4$	Salt Formation (5)
$Ca + ½\ O_2 \rightarrow CaO$	Acidic (6)
$S + O_2 \rightarrow SO_2$; $SO_2 + ½\ O_2 \rightarrow SO_3$	Basic (2)
$SO_3 + CaO \rightarrow CaSO_4$	Salt Formation (7)
$ZrO_2\ (Y_2O_3) + 3SO_3\ (gas) \rightarrow Y_2(SO_4)_3 + m\text{-}ZrO_2$	(8)
$ZrO_2\ (La_2O_3) + 3SO_3\ (gas) \rightarrow La_2(SO_4)_3 + m\text{-}ZrO_2$	(9)
$ZrO_2\ (Gd_2O_3) + 3SO_3\ (gas) \rightarrow Gd_2(SO_4)_3 + m\text{-}ZrO_2$	(10)
$ZrO_2\ (Sm_2O_3) + 3SO_3\ (gas) \rightarrow Sm_2(SO_4)_3 + m\text{-}ZrO_2$	(11)
$ZrO_2\ (Nd_2O_3) + 3SO_3\ (gas) \rightarrow Nd_2(SO_4)_3 + m\text{-}ZrO_2$	(12)

2.3. Rare earth zirconates ($Re_2Zr_2O_7$)

Rare earth zirconate are new potential ceramic materials that is used as TBCs due to their prominent thermal properties. **Figure 2.3.** shows the pyrochlore and fluorite type crystal lattice structure for rare earth zirconates. According to $r(RE^{3+})/r(Zr^{4+})$ and temperature, rare-earth zirconates ($Re_2Zr_2O_7$) usually have a pyrochlore structure (P) or a defective fluorite (F) structure, both belong to face centered cubic (FCC) crystallographic lattice type structure. The pyrochlore structure, categorized under the *Fd3m* (227) space group, is essentially an ordered version of the defective fluorite structure. It has four distinct atomic positions and can be expressed as $Re_2Zr_2O_6O'$, in this configuration, rare-earth cations with larger ionic radii occupy the 16d site, forming cubes with eight surrounding O^{2-} ions. Smaller Zr^{4+} ions occupy the 16c site and are surrounded by six O^{2-} ions, forming octahedra. Oxygen ions are distributed across three positions in the lattice: the 8b, 48f, and 8a sites. The O′ ions are located at the 8b position, O ions are at the 48f position, and the oxygen vacancies are at the 8a site, forming tetrahedra with four Zr^{4+}ions. On the other hand, the fluorite structure is denoted as AO_2, with both cations and oxygen ions occupying a single crystallographic position each. In the defective fluorite variant of rare-earth zirconates, 18 of the oxygen vacancies are randomly distributed. The main difference between the pyrochlore and defective fluorite structures lies in the arrangement of oxygen vacancies, which are ordered in the pyrochlore and disordered in the fluorite structure.

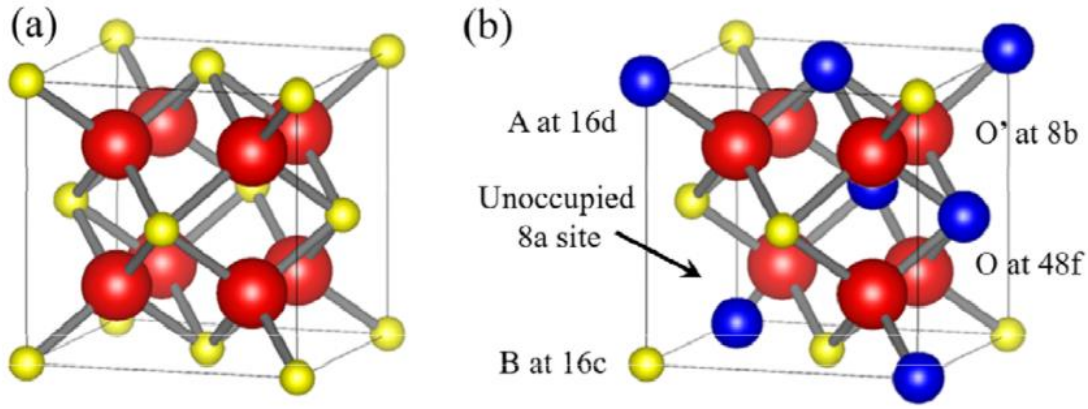

Figure 2.3. (a) Crystal structure fluorite type $Re_2Zr_2O_7$. (b) Crystal structure pyrochlore type $Re_2Zr_2O_7$ [84]

In both pyrochlore and fluorite there is an oxygen vacancy which is responsible for the phonon scattering and helps to reduce thermal conductivity of overall molecular structure $A_2B_2O_7$. Maloney [85] and Wu et al. [44] reported thermal conductivity values of LZO, SmZO, NdZO, and GdZO are between 1.5 -to- 2 $Wm^{-1}K^{-1}$ at 800 ℃, which is significantly lower than that of YSZ. Thermal conductivity calculated by the first principle for rare earth zirconates reveals that GZO and NdZO were anisotropic [86]. $Sm_2Zr_2O_7$ doping with Yb^{3+} initiate phase transition at high temperature, but due to oxygen vacancies- phonon scattering, records the lowest thermal conductivity occurred at $(Sm_{2/3}Yb_{1/3})_2Zr_2O_7$ [87]. The much lower thermal conductivity value less than 1.0 $Wm^{-1}K^{-1}$ is reported for the high entropy zirconates $(La_{0.2}Nd_{0.2}Sm_{0.2}Eu_{0.2}Gd_{0.2})_2Zr_2O_7$ prepared by Li et al. [19], due to their large amount of lattice defect and complexity can be seen in the **Figure 2.4.(e).** Common zirconates that are used as TBCs their thermal conductivity values are mentioned below **Table 2.3**. which are comparable with YSZ.

Table 2.3. Thermal conductivity values of common zirconates at 1473K [88]

Rare earth materials	Thermal conductivity ($Wm^{-1}K^{-1}$)
$La_2Zr_2O_7$	1.98
$Gd_2Zr_2O_7$	1.91
$Sm_2Zr_2O_7$	2.09
$Nd_2Zr_2O_7$	1.83
$Dy_2Zr_2O_7$	1.31 (at 1073.15k) [89]

Li et al. [19] experimented with six rare-earth oxides (La_2O_3, Nd_2O_3, Sm_2O_3, Eu_2O_3, Gd_2O_3, and Y_2O_3) and ZrO_2. Five out of six equimolar rare earth materials investigated for high entropy oxide (HEO). **Figure 2.4. (a).** XRD Pattern 1#$(La_{0.2}Nd_{0.2}Sm_{0.2}Eu_{0.2}Gd_{0.2})_2Zr_2O_7$, 2#$(Y_{0.2}Nd_{0.2}Sm_{0.2}Eu_{0.2}Gd_{0.2})_2Zr_2O_7$, 3#$(La_{0.2}Y_{0.2}Sm_{0.2}Eu_{0.2}Gd_{0.2})_2Zr_2O_7$, 4#$(La_{0.2}Nd_{0.2}Y_{0.2}Eu_{0.2}Gd_{0.2})_2Zr_2O_7$, 5#$(La_{0.2}Nd_{0.2}Sm_{0.2}Y_{0.2}Gd_{0.2})_2Zr_2O_7$, and 6#$(La_{0.2}Nd_{0.2}Sm_{0.2}Eu_{0.2}Y_{0.2})_2Zr_2O_7$ (b) shows one-eighth of the unit cell of the powder. The results indicate that the designed ceramics fall within the stability range of the pyrochlore structure. By sequentially substituting rare-earth ions with Y^{3+} in the ceramic composition #1 $(La_{0.2}Nd_{0.2}Sm_{0.2}Eu_{0.2}Gd_{0.2})_2Zr_2O_7$, the diffraction peaks of sample #2 shift to higher angles, followed by a gradual shift to lower angles from samples 3# through 6#, as shown in **Figure. 2.4.(c). Figure 2.4.(d)** shows the calculated lattice constants of the sintered ceramics, along with a linear fit curve to aid in interpretation. A nearly linear increase in the lattice parameters for sintered ceramics 2#, 3#, 4#, 5#, and 6# is evident. These changes are attributed to the substitution of larger rare-earth ions with smaller Y^{3+} ions, which causes a systematic adjustment in the lattice structure. It is understood that the degree of disorder in rare earth zirconates solid solutions is determined by the ionic radius ratio of rare-earth ions and zirconium ion.

Fluorite type crystals lattice has higher CTE than pyrochlore type crystal lattice due to their weak bonding strength in the structure, and CTE of $RE_2Zr_2O_7$ decreases with increasing radius of rare-earth ions. Doping effects in rare earth zirconate also produces higher value of CTE and lower thermal conductivity level. Fan et al. [89] reported the rare-earth elements CTEs via a data driven approach. The molecular dynamics method was used, and the results are shown in **Table 2.4**. Zr-O bond has influence on the functional structure and the mechanical properties of rare-earth zirconate materials like CTE due to anharmonicity of atomic vibrations.

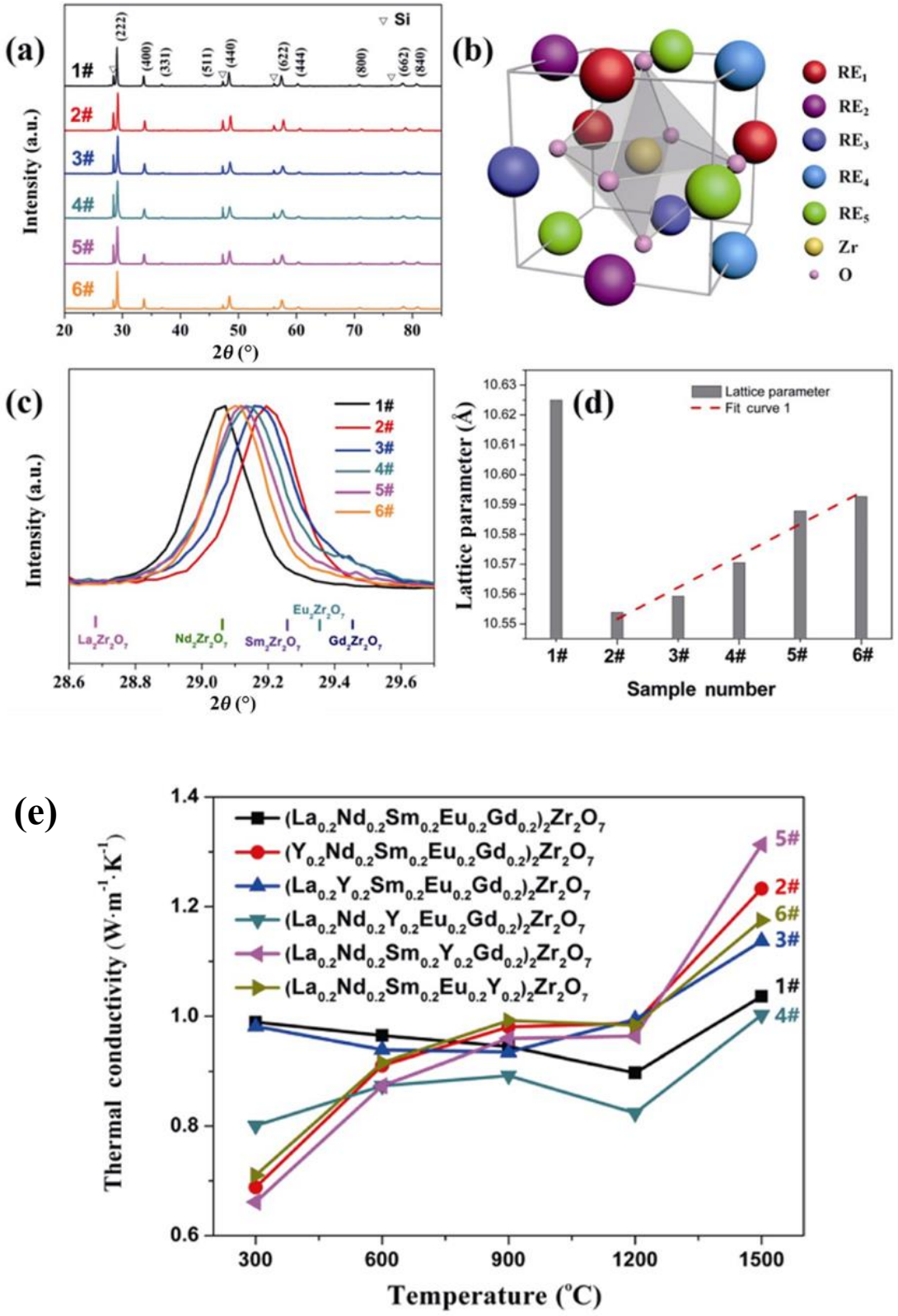

Figure 2.4. (a) XRD pattern of high entropy ceramic after 1500 °C for 3 h (b) Crystal pyrochlore type structure (c) Broad View in (222) diffraction peaks (d) Lattice parameter of sintered (e) Thermal conductivity after 1500 °C for 3 h [19]

Table 2.4 Calculated CTE of rare earth zirconate elements [90]

Rare earth materials	CTE of pyrochlore (10^{-6} K^{-1})	CTE of fluorite (10^{-6} K^{-1})
$Lu_2Zr_2O_7$	8.57	9.39
$Gd_2Zr_2O_7$	7.91	9.18
$Sm_2Zr_2O_7$	7.77	9.55
$Nd_2Zr_2O_7$	7.80	9.71
$Eu_2Zr_2O_7$	7.81	8.88
$Er_2Zr_2O_7$	8.00	9.02
$Yb_2Zr_2O_7$	7.99	9.37

2.4. Dual-phase TBCs- innovative coatings type

Dual-phase TBCs are new types of coatings also called two phase thermal barrier coatings, modified from double ceramic layer (DCL). These coatings consist of two distinct phases or microstructures, usually a composite ceramic layer and a metallic layer, that are designed to work together to provide superior thermal insulation and resistance to thermal cycling. In the case of dual-phase TBCs, the ceramic TC layer is often composed of two ceramic substances, such as YSZ with rare earth zirconates/cerates, mullites, which has excellent thermal insulation properties and can withstand high temperatures without degrading. The metallic layer is usually made of a material such as a MCrAlY (metal-ceramic-aluminum-yttrium) alloy, which provides good adhesion to the substrate and also acts as a diffusion barrier to prevent oxidation and other forms of corrosion. The two layers are designed to work together to provide a number of benefits. The ceramic layer provides excellent thermal insulation, reducing the heat transfer from the hot gas stream to the engine component. This helps to protect the component from overheating and reduces the risk of thermal fatigue or cracking. The metallic layer provides good adhesion to the substrate and acts as a diffusion barrier, preventing the underlying material from oxidizing or corroding. The dual-phase new type of TBCs is also designed to withstand the thermal cycling that occurs in high-temperature environments. During operation, the engine component will go through cycles of heating and cooling as the hot gas stream flows over it. This can cause thermal stresses that can lead to cracking or delamination of the coating.

However, the dual-phase TBCs is designed to withstand these stresses by allowing the two layers to expand and contract at different rates, reducing the risk of cracking or delamination. Dual-phase coatings and composite coatings are both types of coatings used in various industries for their unique properties and benefits [91-92]. However, they differ in their composition, structure, and performance characteristics. Dual-phase coatings are made by combining two different materials, usually pure ceramics or alloys, in a way that creates two distinct phases or microstructures within the coating. These phases can have different chemical and physical properties, such as different melting points, hardness, or corrosion resistance. Dual-phase coatings are often used for their superior wear resistance, corrosion resistance, ultimate low thermal conductivity and higher fracture toughness or thermal stability. No material now in use possesses all of these features; for instance, rare earth pyrochlores have the necessary thermal properties but lack the necessary mechanical attributes for outstanding overall endurance. Schmitt et al**.** [92] fabricated the multiphase coatings via APS creating monolithic and composite TBCs. The coatings were produced using cubic Low-k, t′ Low-k, and YSZ materials. It was observed that by introducing a resilient t′ Low-k phase within a predominantly thermally stable, low-conductivity cubic Low-k, composite t′ and cubic Low-k coatings hold the potential to enhance TBCs performance. These multi-phase coatings, comprised of t′ Low-k and cubic Low-k components, display notably lower thermal conductivities compared to 7YSZ, while preserving comparable porosity and shape. Furthermore, investigations revealed that the incorporation of t′ Low-k secondary phases in nonlinear proportions can extend the resistance of cubic Low-k coatings against erosion. Increasing the t′ Low-k phase by 20 % led to a reduction of over 37 % in the contrast between t′ Low-k and cubic Low-k, concurrently diminishing the erosion rate. According to multi-phase composite mixing principles, there is much more room for customized microstructures of composite TBCs can provide improved benefit.

It is also observed that while the use of secondary phases can provide benefits in improving TBCs performance, these benefits are limited by practical factors such as flaws and defects. The study utilized a toughening t′ Low-k phase, which may be unstable at elevated temperatures (> 1400 °C) for prolonged periods, future studies could explore other secondary phases that are thermally stable in this temperature range. The secondary phase used must have high overall durability and thermal stability, although it does not necessarily

need to have low thermal conductivity since the matrix phase provides most of the thermal insulation. This opens up the possibility of using materials that are not traditionally considered for TBC applications.

In dual phase TBCs, one material is typically used as the matrix, while the other is used as the reinforcing phase. The reinforcing phase can be in the form of particles, fibers, and is usually chosen for its low thermal conductivity. By incorporating the reinforcing phase into the matrix, the overall thermal conductivity of the TBCs can be reduced. Composite TBCs have been shown to have lower thermal conductivity than single-phase TBCs at elevated temperatures. This makes them suitable for use in high-temperature applications where thermal insulation is critical. In recent studies, the formation of dual phase TC material between $Sm_2Zr_2O_7$ and 8YSZ have been found to significantly reduce the thermal conductivity of the resulting composite dual phase material, which can be beneficial for certain applications where thermal insulation is required [61], [70]. Dual Phase TBCs systems are made up of two or more ceramic materials with different thermal conductivities, and they can be designed to have a lower overall thermal conductivity than single-phase TBCs. The lowering of thermal conductivity for TBCs is a great challenge for new materials. There are various types of ceramic coatings available in the TBCs systems, and they can be classified based on their composition, structure, and thickness. Several different ceramic coating architectures of TBCs are illustrated in **Figure 2.5.** In monolayer coatings, there is only one ceramic layer used to provide standard protection. In double-layer ceramic coatings (DCL), two layers of different compositions are used in order to achieve advanced performance. In the triple ceramic coatings, three layers provide properties in a wider range. Functional graded coatings (FGCs) use a number of layers with different composition and structure in order to limit the thermal stress and improve adhesion. In dual-phase TBCs, two phases are present in the coating system. Single layer and double layer dual phase composite system presented in **Figure 2.5.** parts (e) and (f).

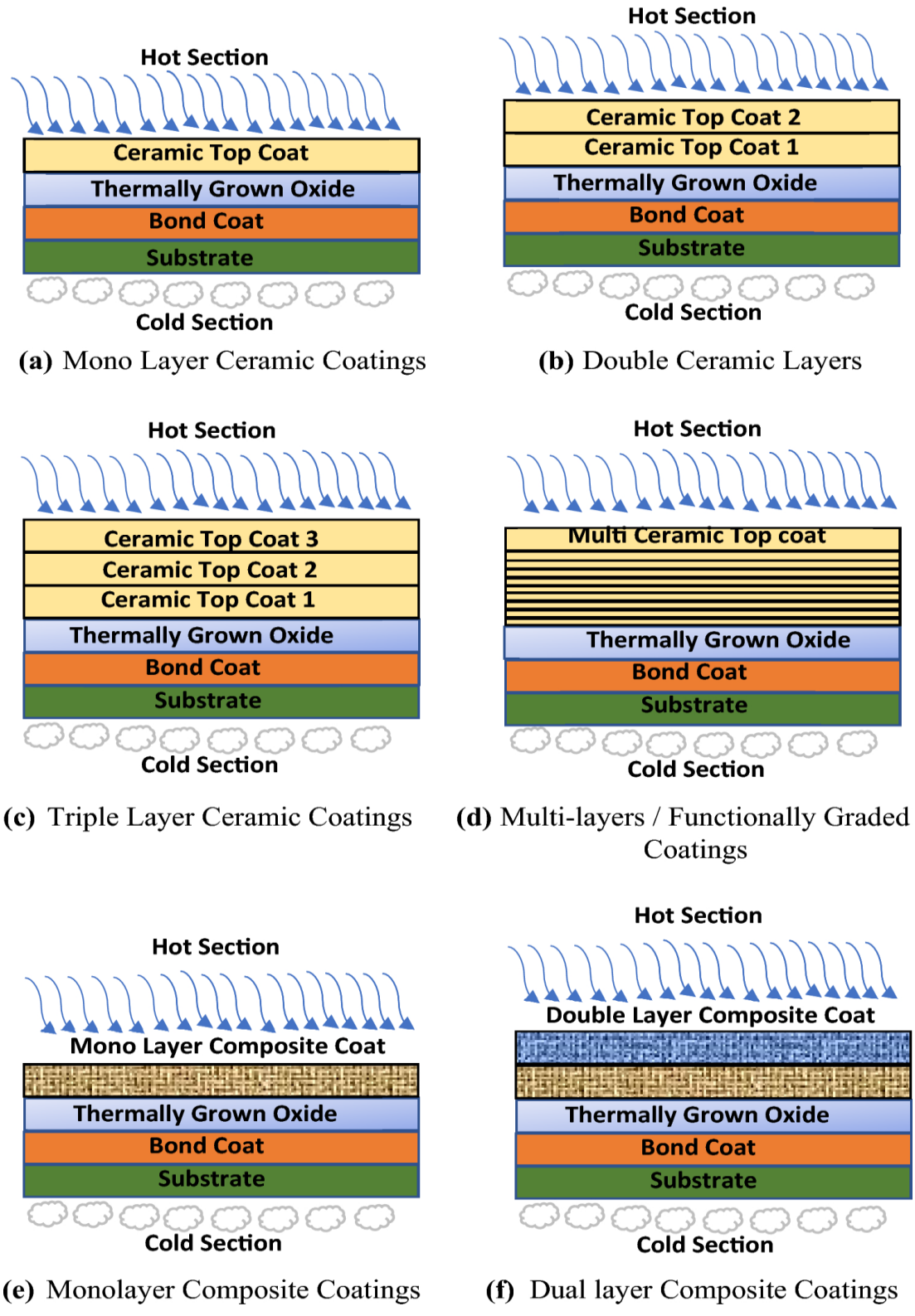

Figure 2.5. The architecture of a Fabricated System and level of advancements [16]

2.5. References.

1. Liu, Q., Huang, S., & He, A. (2019). Composite ceramics thermal barrier coatings of yttria stabilized zirconia for aero-engines. *Journal of materials science & technology*, *35*(12), 2814-2823.
2. Jayakumar, T., Mathew, M. D., Laha, K., & Sandhya, R. (2013). Materials development for fast reactor applications. *Nuclear Engineering and Design*, *265*, 1175-1180.
3. Jayakumar, T., Mathew, M. D., & Laha, K. (2013). High temperature materials for nuclear fast fission and fusion reactors and advanced fossil power plants. *Procedia Engineering*, *55*, 259-270.
4. Cao, X. Q., Vassen, R., & Stöver, D. (2004). Ceramic materials for thermal barrier coatings. *Journal of the European Ceramic Society*, *24*(1), 1-10.
5. Moskal, G. (2009). Thermal barrier coatings: characteristics of microstructure and properties, generation and directions of development of bond. *Journal of Achievements in Materials and Manufacturing Engineering*, *37*(2), 323-331.
6. Ali, I., Sokołowski, P., Pawłowski, L., Wett, D., Grund, T., & Lampke, T. (2021). Study on the characteristics of a TBC system containing a PVD-Al interlayer under isothermal loading. *Coatings*, *11*(8), 887.
7. Myoung, S. W., Lee, S. S., Kim, H. S., Kim, M. S., Jung, Y. G., Jung, S. I., ... & Paik, U. (2013). Effect of post heat treatment on thermal durability of thermal barrier coatings in thermal fatigue tests. *Surface and Coatings Technology*, *215*, 46-51.
8. Bogdan, M., & Peter, I. (2024). A Comprehensive Understanding of Thermal Barrier Coatings (TBCs): Applications, Materials, Coating Design and Failure Mechanisms. *Metals*, *14*(5), 575.
9. Clarke, D. R., Oechsner, M., & Padture, N. P. (2012). Thermal-barrier coatings for more efficient gas-turbine engines. *MRS bulletin*, *37*(10), 891-898.
10. K.K. Maniam, S. Paul, Progress in novel electrodeposited bond coats for thermal barrier coating systems, Materials 14 (15) (2021) 4214
11. S. Wu, Y. Zhao, W. Li, W. Liu, Y. Wu, F. Liu, Research progresses on ceramic materials of thermal barrier coatings on gas turbine, Coatings 11 (1) (2021) 79.
12. S.R.J. Saunders, J.R. Nicholls, Coatings and surface treatments for high temperature oxidation resistance, Mater. Sci. Technol. 5 (8) (1989) 780–798.
13. M. Perrut, P. Caron, M. Thomas, A. Couret, High temperature materials for aerospace applications: Ni-based superalloys and γ-TiAl alloys, Comptes Rendus Phys. 19 (8) (2018) 657–671.
14. Zhang, C., Chen, F., Huang, Z., Jia, M., Chen, G., Ye, Y., ... & Lavernia, E. J. (2019). Additive manufacturing of functionally graded materials: A review. *Materials Science and Engineering: A*, *764*, 138209.
15. Belmonte, M. (2006). Advanced ceramic materials for high temperature applications. *Advanced engineering materials*, *8*(8), 693-703.
16. Iqbal, A., & Moskal, G. (2023). Recent development in advance ceramic materials and understanding the mechanisms of thermal barrier coatings degradation. *Archives of Computational Methods in Engineering*, *30*(8), 4855-4896.
17. Wu, S., Zhao, Y., Li, W., Liu, W., Wu, Y., & Liu, F. (2021). Research progresses on ceramic materials of thermal barrier coatings on gas turbine. *Coatings*, *11*(1), 79.
18. Zhaolu, X. U. E., Hongbo, G. U. O., Shengkai, G. O. N. G., & Huibin, X. U. (2018). Novel ceramic materials for thermal barrier coatings. *航空材料学报*, *38*(2), 10-20.
19. Li, F., Zhou, L., Liu, J. X., Liang, Y., & Zhang, G. J. (2019). High-entropy pyrochlores with low thermal conductivity for thermal barrier coating materials. *Journal of Advanced Ceramics*, *8*, 576-582.
20. Ren, X., & Pan, W. (2014). Mechanical properties of high-temperature-degraded yttria-stabilized zirconia. *Acta materialia*, *69*, 397-406.
21. Hasselman, D., Johnson, L. F., Bentsen, L. D., SYED, R., Lee, H. L., & SWAIN, M. V. (1987). Thermal diffusivity and conductivity of dense polycrystalline Zr0. *Am. Ceram. Soc. Bull*, *66*(5), 799-806.
22. Saini, A. K., Das, D., & Pathak, M. K. (2012). Thermal barrier coatings-applications, stability and longevity aspects. *Procedia Eng*, *38*, 3173-3179.
23. Hasselman, D., Johnson, L. F., Bentsen, L. D., SYED, R., Lee, H. L., & SWAIN, M. V. (1987). Thermal diffusivity and conductivity of dense polycrystalline Zr0. *Am. Ceram. Soc. Bull*, *66*(5), 799-806.
24. Vaßen, R., Kerkhoff, G., & Stöver, D. (2001). Development of a micromechanical life prediction model for plasma sprayed thermal barrier coatings. *Materials Science and Engineering: A*, *303*(1-2), 100-109.
25. Cao, X. Q., Vassen, R., & Stöver, D. (2004). Ceramic materials for thermal barrier coatings. *Journal of the European Ceramic Society*, *24*(1), 1-10.
26. Hirata, Y., Shimonosono, T., Itoh, S., & Kiritoshi, S. (2017). Theoretical and experimental analyses of thermal properties of dense polycrystalline mullite. *Ceramics International*, *43*(13), 10410-10414.
27. Shen, Z., Liu, G., He, L., Mu, R., & Dai, J. (2022). Thermal property and failure behaviors of Gd doped LaZrCeO coatings with feathery microstructure. *npj Materials Degradation*, *6*(1), 17.
28. Shen, Z., He, L., Mu, R., Xu, Z., & Huang, G. (2020). Effects of gradient transitional layer on thermal cycling life and failure of LaZrCeO/YSZ thermal barrier coatings. *Corrosion Science*, *163*, 108224.
29. Lin, C. H. E. N., Keren, L. U. O., Baihui, L. I., Mingyu, H. U., & Jing, F. E. N. G. (2023). Mechanical property enhancements and amorphous thermal transports of ordered weberite-type RE 3 Nb/TaO 7 high-entropy oxides. *Journal of Advanced Ceramics*, *12*(2).
30. Lai, L., Gan, M., Wang, J., Chen, L., Liang, X., Feng, J., & Chong, X. (2023). New class of high-entropy rare-earth niobates with high thermal expansion and oxygen insulation. *Journal of the American Ceramic Society*, *106*(7), 4343-4357.

31. Feng, J., Wang, J., Yang, K., & Chen, L. (2023). Thermophysical properties investigations and optimizations of RETaO4 ceramics for thermal barrier coatings applications. In *Thermal Barrier Coatings* (pp. 21-41). Woodhead Publishing.
32. Soare, A., Csaki, I., Sohaciu, M., Oprea, C., Soare, S., Costina, I., & Petrescu, M. I. (2017, June). New bond coat materials for thermal barrier coating systems processed via different routes. In *IOP conference series: materials science and engineering* (Vol. 209, No. 1, p. 012045). IOP Publishing.
33. Rabieifar, A. (2023). A Comprehensive Review of Thermal Barrier Coatings Microstructure with Different Platinum-Modified Aluminide Bond Coats. *Journal of Environmental Friendly Materials*, *7*(1), 65-79.
34. Shahbazi, H., Vakilifard, H., Nair, R. B., Liberati, A. C., Moreau, C., & Lima, R. S. (2023, May). High Entropy Alloy (HEA) Bond Coats for Thermal Barrier Coatings (TBCs)—A Review. In *International Thermal Spray Conference* (Vol. 84536, pp. 659-666). ASM International.
35. Vassen, R., Stuke, A., & Stöver, D. (2009). Recent developments in the field of thermal barrier coatings. *Journal of thermal spray technology*, *18*, 181-186.
36. Zhang, J., Guo, X., Jung, Y. G., Li, L., & Knapp, J. (2017). Lanthanum zirconate based thermal barrier coatings: A review. *Surface and Coatings Technology*, *323*, 18-29.
37. Wang, C. (2006). Experimental and computational phase studies of the ZrO2-based systems for thermal barrier coatings.
38. Curtis, C. E. (1957). Properties of yttrium oxide ceramics. *Journal of the American Ceramic Society*, *40*(8), 274-278.
39. Liu, H., Li, S., Li, Q., & Li, Y. (2010). Investigation on the phase stability, sintering and thermal conductivity of Sc2O3–Y2O3–ZrO2 for thermal barrier coating application. *Materials & Design*, *31*(6), 2972-2977.
40. Di Girolamo, G., Blasi, C., Schioppa, M., & Tapfer, L. (2010). Structure and thermal properties of heat treated plasma sprayed ceria–yttria co-stabilized zirconia coatings. *Ceramics International*, *36*(3), 961-968.
41. Lakiza, S. M., Hrechanyuk, M. I., Red'ko, V. P., Ruban, O. K., Tyshchenko, J. S., Makudera, A. O., & Dudnik, O. V. (2021). The role of hafnium in modern thermal barrier coatings. *powder metallurgy and metal ceramics*, *60*(1), 78-89.
42. Wu, Y., Hong, D., Zhong, X., Niu, Y., & Zheng, X. (2023). Research progress on hafnium-based thermal barrier coatings materials. *Ceramics International*, *49*(13), 21133-21141.
43. Hajizadeh-Oghaz, M., Shoja Razavi, R., & Ghasemi, A. (2015). Synthesis and characterization of ceria–yttria co-stabilized zirconia (CYSZ) nanoparticles by sol–gel process for thermal barrier coatings (TBCs) applications. *Journal of Sol-Gel Science and Technology*, *74*(3), 603-612.
44. Wu, J., Wei, X., Padture, N. P., Klemens, P. G., Gell, M., García, E., ... & Osendi, M. I. (2002). Low-thermal-conductivity rare-earth zirconates for potential thermal-barrier-coating applications. *Journal of the American Ceramic Society*, *85*(12), 3031-3035.
45. Dai, H., Zhong, X., Li, J., Meng, J., & Cao, X. (2006). Neodymium–cerium oxide as new thermal barrier coating material. *Surface and Coatings Technology*, *201*(6), 2527-2533.
46. Di Girolamo, G. (2023). New Materials for Thermal Barrier Coatings: Design, Manufacturing and Performance. In *Ceramic Coatings for High-Temperature Environments: From Thermal Barrier to Environmental Barrier Applications* (pp. 3-36). Cham: Springer International Publishing.
47. Ma, W., Gong, S., Xu, H., & Cao, X. (2006). The thermal cycling behavior of Lanthanum–Cerium Oxide thermal barrier coating prepared by EB–PVD. *Surface and Coatings Technology*, *200*(16-17), 5113-5118.
48. Park, S. Y., Kim, J. H., Kim, M. C., Song, H. S., & Park, C. G. (2005). Microscopic observation of degradation behavior in yttria and ceria stabilized zirconia thermal barrier coatings under hot corrosion. *Surface and Coatings Technology*, *190*(2-3), 357-365.
49. Ma, W., & Dong, H. (2011). Ceramic thermal barrier coating materials. In *Thermal barrier coatings* (pp. 25-52). Woodhead publishing.
50. Vourdas, N., Marathoniti, E., Pandis, P. K., Argirusis, C., Sourkouni, G., Legros, C., ... & Stathopoulos, V. N. (2018). Evaluation of LaAlO3 as top coat material for thermal barrier coatings. *Transactions of Nonferrous Metals Society of China*, *28*(8), 1582-1592.
51. Georgiopoulos, I., Vourdas, N., Mirza, S., Andreouli, C., & Stathopoulos, V. (2018). LaAlO3 as overlayer in conventional thermal barrier coatings. *Procedia Structural Integrity*, *10*, 280-287.
52. Hoffman, M. A., Lawler, B. J., Güralp, O. A., Najt, P. M., & Filipi, Z. S. (2015). The impact of a magnesium zirconate thermal barrier coating on homogeneous charge compression ignition operational variability and the formation of combustion chamber deposits. *International Journal of Engine Research*, *16*(8), 968-981.
53. Bespalko, Y., Kuznetsova, T., Kriger, T., Chesalov, Y., Lapina, O., Ishchenko, A., ... & Stathopoulos, V. (2020). La2Zr2O7/LaAlO3 composite prepared by mixing precipitated precursors: Evolution of its structure under sintering. *Materials Chemistry and Physics*, *251*, 123093.
54. Yuan, J., Sun, J., Wang, J., Zhang, H., Dong, S., Jiang, J., ... & Cao, X. (2018). SrCeO3 as a novel thermal barrier coating candidate for high–temperature applications. *Journal of Alloys and Compounds*, *740*, 519-528.
55. Kumar, V., Sharma, R., Sharma, A. K., & Sharma, R. K. (2023). Mechanical stresses analysis of a partially ceramic coated cylinder liners using finite element analysis. *Materials Today: Proceedings*, *72*, 2369-2377.
56. Cano, C., Osendi, M. I., Belmonte, M., & Miranzo, P. (2006). Effect of the type of flame on the microstructure of CaZrO3 combustion flame sprayed coatings. *Surface and Coatings Technology*, *201*(6), 3307-3313.
57. Wang, L., Di, Y., Wang, H., Li, X., Dong, L., & Liu, T. (2019). Effect of lanthanum zirconate on high temperature resistance of thermal barrier coatings. *Transactions of the Indian Ceramic Society*, *78*(4), 212-218.
58. Chen, L., Hu, M., Guo, J., Chong, X., & Feng, J. (2020). Mechanical and thermal properties of RETaO4 (RE= Yb, Lu, Sc) ceramics with monoclinic-prime phase. *Journal of Materials Science & Technology*, *52*, 20-28.
59. Wang, J., Chong, X., Zhou, R., & Feng, J. (2017). Microstructure and thermal properties of RETaO4 (RE= Nd, Eu, Gd, Dy, Er, Yb, Lu) as promising thermal barrier coating materials. *Scripta Materialia*, *126*, 24-28.
60. Zhang, P., Feng, Y., Li, Y., Pan, W., Zong, P. A., Huang, M., ... & Wan, C. (2020). Thermal and mechanical properties of ferroelastic RENbO4 (RE= Nd, Sm, Gd, Dy, Er, Yb) for thermal barrier coatings. *Scripta Materialia*, *180*, 51-56.

61. Moskal, G., Jasik, A., Mikuśkiewicz, M., & Jucha, S. (2020). Thermal resistance determination of Sm2Zr2O7+ 8YSZ composite type of TBC. *Applied Surface Science*, *515*, 145998.
62. Gonzalez-Rodriguez, J. G., Haro, S., Martinez-Villafane, A., Salinas-Bravo, V. M., & Porcayo-Calderon, J. (2006). Corrosion performance of heat resistant alloys in Na2SO4–V2O5 molten salts. *Materials science and engineering: A*, *435*, 258-265.
63. Wong-Moreno, A., Martinez, Y. M., & Martinez, L. (1994). *High temperature corrosion enhanced by residual fuel oil ash deposits* (No. CONF-940222-). NACE International, Houston, TX (United States).
64. Zhou, X., He, L., Cao, X., Xu, Z., Mu, R., Sun, J., ... & Zou, B. (2017). La2 (Zr0. 7Ce0. 3) 2O7 thermal barrier coatings prepared by electron beam-physical vapor deposition that are resistant to high temperature attack by molten silicate. *Corrosion Science*, *115*, 143-151.
65. Kang, Y. X., Bai, Y., Bao, C. G., Wang, Y., Chen, H. Y., Gao, Y., & Li, B. Q. (2017). Defects/CMAS corrosion resistance relationship in plasma sprayed YPSZ coating. *Journal of Alloys and Compounds*, *694*, 1320-1330.
66. Song, W., Yang, S., Fukumoto, M., Lavallée, Y., Lokachari, S., Guo, H., ... & Dingwell, D. B. (2019). Impact interaction of in-flight high-energy molten volcanic ash droplets with jet engines. *Acta Materialia*, *171*, 119-131.
67. Jinyang, H. U. A. N. G., Jintao, L. U., Zhen, Y. A. N. G., Yongli, Z. H. O. U., Yingying, D. A. N. G., & Yong, Y. U. A. N. (2018, November). Corrosion Behavior of Austenitic stainless steels utilized for coal-fired boilers in simulated coal-ash/high sulfur environments. In *2018 International Conference on Power System Technology (POWERCON)* (pp. 4525-4532). IEEE.
68. Rapp, R. A., & Goto, K. S. (1981). The hot corrosion of metals by molten salts. *ECS Proceedings Volumes*, *1981*(1), 159.
69. Wang, Y., Pillai, R., Yazhenskikh, E., Frommherz, M., Müller, M., Quadakkers, W. J., & Naumenko, D. (2022). Comparison of Na2SO4, K2SO4 and Na2SO4-K2SO4 deposit induced hot corrosion of a β-NiAl coating. *Corrosion Science*, *198*, 110146.
70. Moskal, G., Jucha, S., Mikuśkiewicz, M., Migas, D., & Jasik, A. (2020). Atypical decomposition processes of Sm2Zr2O7+ 8YSZ dual-phase TBCs during hot corrosion. *Corrosion Science*, *170*, 108681.
71. Roy, P., & Ghosh, S. (2023). Oxidation and Hot Corrosion Behavior of Thermal Barrier Coatings-A Brief Review. *High Temperature Corrosion of Materials*, *99*(5), 331-343.
72. Chen, K., Seo, D., Lee, S. H., & Byon, E. (2018). A physics-based model of temperature-exposure-dependent interfacial fracture toughness of thermal barrier coatings. *Journal of Physics Communications*, *2*(12), 125005.
73. Essa, S. K., Liu, R., & Yao, M. X. (2019). Temperature and exposure-dependent interfacial fracture toughness model for thermal barrier coatings. *Surface and Coatings Technology*, *358*, 505-510.
74. Kalsi, S. S. (2015). Hot corrosion and its mechanism: a review. *Int. J. Emerg. Technol*, *7*, 133-136.
75. Khanna, A. S. (2005). High temperature oxidation. In *Handbook of environmental degradation of materials* (pp. 105-152). William Andrew Publishing.
76. Mehta, A., Vasudev, H., Singh, S., Prakash, C., Saxena, K. K., Linul, E., ... & Xu, J. (2022). Processing and advancements in the development of thermal barrier coatings: a review. *Coatings*, *12*(9), 1318.
77. Mohanty, B. P., & Shores, D. A. (2004). Role of chlorides in hot corrosion of a cast Fe–Cr–Ni alloy. Part I: experimental studies. *Corrosion science*, *46*(12), 2893-2907.
78. Xu, Z., He, L., Mu, R., He, S., Huang, G., & Cao, X. (2010). Hot corrosion behavior of rare earth zirconates and yttria partially stabilized zirconia thermal barrier coatings. *Surface and Coatings Technology*, *204*(21-22), 3652-3661.
79. Iqbal, A., Khan, M. J., & Moskal, G. (2022). A review on the degradation of coatings under hot corrosion process. *Contemporary problems of power engineering and environmental protection*, *27*.
80. Jones, R. L. (1997). Some aspects of the hot corrosion of thermal barrier coatings. *Journal of thermal spray technology*, *6*, 77-84.
81. Jones, R. L. (1996). Thermal barrier coatings. In *Metallurgical and ceramic protective coatings* (pp. 194-235). Dordrecht: Springer Netherlands.
82. Ozgurluk, Y., Doleker, K. M., & Karaoglanli, A. C. (2019). Investigation of the effect of V2O5 and Na2SO4 melted salts on thermal barrier coatings under cyclic conditions. *Anti-Corrosion Methods and Materials*, *66*(5), 644-650.
83. Kaplan, M., Uyaner, M., Ozgurluk, Y., Doleker, K. M., & Karaoglanli, A. C. (2019). Evaluation of hot corrosion behavior of APS and HVOF sprayed thermal barrier coatings (TBCs) exposed to molten Na 2 SO 4+ V 2 O 5 salt at 1000 C. *Engineering design applications*, 441-459.
84. Wei, Z. Y., Meng, G. H., Chen, L., Li, G. R., Liu, M. J., Zhang, W. X., ... & Li, C. J. (2022). Progress in ceramic materials and structure design toward advanced thermal barrier coatings. *Journal of advanced ceramics*, *11*(7), 985-1068.
85. Maloney, M. J. (2005). *U.S. Patent No. 6,924,040*. Washington, DC: U.S. Patent and Trademark Office.
86. Feng, J., Xiao, B., Zhou, R., & Pan, W. (2013). Thermal conductivity of rare earth zirconate pyrochlore from first principles. *Scripta Materialia*, *68*(9), 727-730.
87. Wan, C., Qu, Z., Du, A., & Pan, W. (2011). Order–disorder transition and unconventional thermal conductivities of the (Sm1−xYbx) 2Zr2O7 series. *Journal of the American Ceramic Society*, *94*(2), 592-596.
88. Wang, J. D., Pan, W., Xu, Q., Mori, K., & Torigoe, T. (2004). Thermal conductivity of the new candidate materials for thermal barrier coatings. *Key Engineering Materials*, *280*, 1503-1506.
89. Qiang, X., Wei, P., Jingdong, W., Longhao, Q., Hezhuo, M., Mori, K., & Torigoe, T. (2005). Preparation and thermophysical properties of Dy2Zr2O7 ceramic for thermal barrier coatings. *Materials Letters*, *59*(22), 2804-2807.
90. Qun-bo, F., Feng, Z., Fu-chi, W., & Lu, W. (2009). Molecular dynamics calculation of thermal expansion coefficient of a series of rare-earth zirconates. *Computational materials science*, *46*(3), 716-719.
91. Mayrhofer, P. H., Mitterer, C., & Musil, J. (2003). Structure–property relationships in single-and dual-phase nanocrystalline hard coatings. *Surface and Coatings Technology*, *174*, 725-731.
92. Yurov, V. M., Guchenko, S. A., Platonova, E. S., Syzdykova, A. S., & Lysenko, E. N. (2015, March). Multiphase composite coatings: structure and properties. In *IOP Conference Series: Materials Science and Engineering* (Vol. 81, No. 1, p. 012090). IOP Publishing.

93. Schmitt, M. P., Rai, A. K., Zhu, D., Dorfman, M. R., & Wolfe, D. E. (2015). Thermal conductivity and erosion durability of composite two-phase air plasma sprayed thermal barrier coatings. *Surface and Coatings Technology*, *279*, 44-52

3. EXPERIMENTAL PROCEDURE

3.1. State of the art experiment

The experimental procedure begins by analyzing the characterization of commercially available powders, followed by the deposition of coatings via plasma spray process. The powders characterization includes, Scanning Electron Microscopy (SEM), Electron Backscatter Diffraction (EBSD), X-ray Diffraction (XRD), Laser Diffraction via Mastersizer. Inframat® Advanced Materials™ supplied yttria- YSZ powder, featuring particle sizes ranging from 20 to 138 μm, while Skyworks provided LZO and LCO powder with particle sizes ranging from 26 to 190 μm. The gadolinium zirconate powder, encompassing similar particle sizes of 26–190 μm, was also acquired from Skyworks. The particle size distribution was determined using Mastersizer 3000 from Malvern Instrument LTD., a UK-based company equipped with a Hydro 2000S attachment. To analyze the particle size distribution within the tested powder, a detailed examination of the scattered light pattern, including factors such as light intensity and deflection angles, was performed and compared to an optical model.

The base of this optical model lies in Mie theory, also recognized as the Lorenz-Mie theory. This theory offers a comprehensive framework for elucidating light scattering phenomena when particles of diverse sizes are present, irrespective of their transparency characteristics. It stands as a notable progression beyond the traditional Rayleigh scattering theory, especially when addressing particles with dimensions surpassing the wavelength of the incident light. It is vital to note that the presented results stem from a combination of data derived from seven separate and independent measurements.

The next step was to deposit plasma spray (PS) coatings on Ni-based super alloys followed by the investigation of TBC coated samples at high temperatures. The substrate utilized in this study was a nickel-based superalloy, specifically Inconel (IN) 625, and its chemical composition is detailed in **Table 3.1.** This research focused on applying conventional and innovative TBC materials on NiCrAlY-BC. The Parameter used for BC and TC are given in

Table 3.2. The NiCrAlY-BC had been previously applied to the Ni-based superalloy IN 625 using an atmospheric plasma spray (APS) technique. The material for the NiCrAlY BC was derived from a metal powder with a particle size of 106 + 53 μm, obtained from Oerlikon Metco under the name Amdry 962. Across all instances, the BC consistently exhibited a thickness of approximately 125 μm. For ceramic TC, commercially available powders YSZ, LZO, GZO, LCO were employed. The substrate underwent preparatory operations, including grinding with silicon carbide (SiC) sheets and humid grit-blasting with alumina (220# mesh) at a pressure of 0.3 MPa before applying the BC. Subsequently, a degreasing operation occurred in a boiling aqueous solution of 50 g/L sodium hydroxide (NaOH) for 10 minutes, followed by ultrasonic cleaning in ethanol for an additional 10 minutes. Coatings were deposited on flat substrate and then cut into desired shape for characterization. Double powder feed systems were used to apply an insulating layer for the deposition. Importantly, the conclusion of this study resulted in the successful fabrication of three types of dual-phase ceramic layer 50/50 mole percentage composition of Lanthanum Zirconate based dual phase system (LZO+YSZ), Lanthanum Cerate based dual phase system (LCO+YSZ), and Gadolinium Zirconate based dual phase system (GZO+YSZ). **Figure 3.1**. shows the overall experimental flow sheet diagram.

Table 3.1. Chemical composition of IN 625 substrate alloy.

Wt%	**Fe**	**Nb + Ta**	**Mo**	**Cr**	**Ni**	**Ti**	**Mn**	**Co**	**Al**	**P**	**Si**	**S**
Inconel 625	4.8 max	3.10–4.10	9.5 max	19–22	57.0 min	0.39 max	0.49 max	1.0 max	0.40 max	0.15 max	0.49 max	0.14 max

Table 3.2. Technical Parameters for the Depositions of coatings.

Parameter	**Dual phase TBC System**
Burner type	F4MB

Argon [L/min]	40
Hydrogen [L/min]	20
Powder carrier [L/min]	2,6
Powder feeding [g/min]	15
Current [A]	600
Arc Voltage [V]	61.1–62.3
Burner power [KW]	37.2–38.1
Mixing	60
Rotation [RPM]	120
The diameter of the plasma torch	150
Feed Rate of Powder [mm/s]	10
Distance between nozzle and substrate [mm]	100
Number of program cycles	30

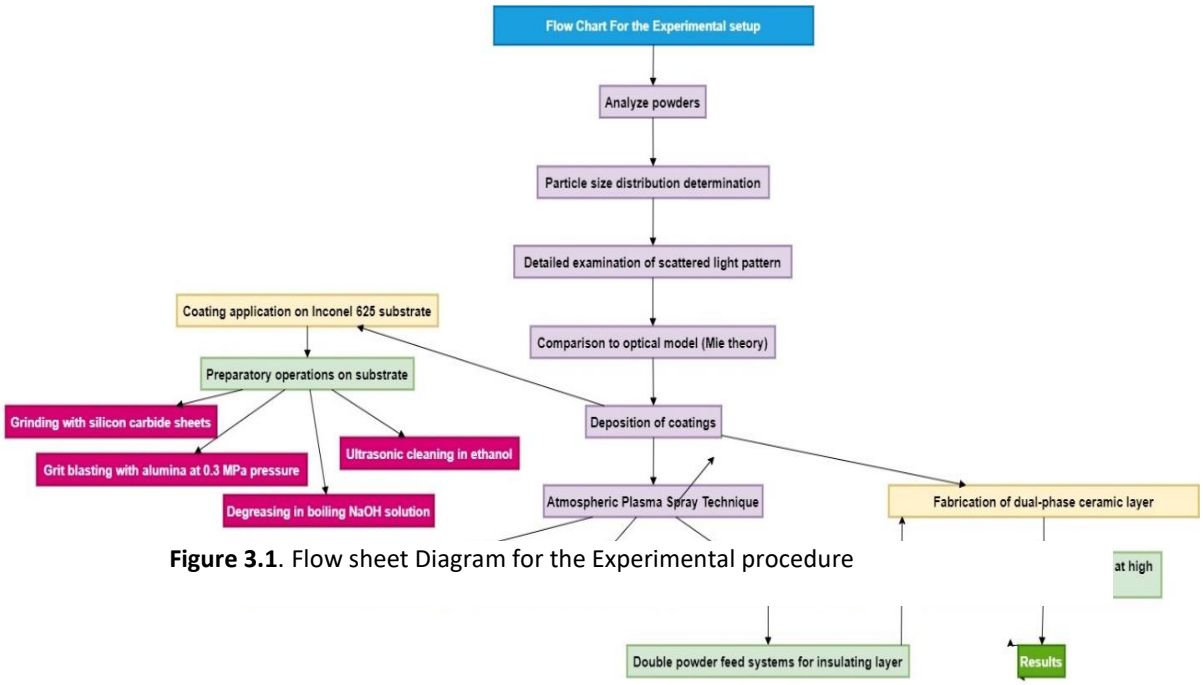

Figure 3.1. Flow sheet Diagram for the Experimental procedure

3.2. Hot corrosion – pure oxidation test

The hot corrosion and pure oxidation tests were conducted on three types of dual phase TBCs systems LZO+YSZ, GZO+YSZ, LCO+YSZ. The three types of dual phase system LZO+YSZ, GZO+YSZ, LCO+YSZ underwent hot corrosion and pure oxidation tests at the temperature ranges from 920 °C to 1100 °C. The experimental setup consisted in a carbolite tube furnace (Type and model; CTF 18/300) and controlled testing conditions were ensured. The hot corrosion experiment for all developed TBCs systems was performed in the presence of Na_2SO_4 salts and, for LZO+YSZ case, a mixture of Na_2SO_4 plus V_2O_5 was also evaluated. The experimental procedure involved exposing the coated samples, for 10 days - 240 hours, to a corrosive environment consisting of pure Na_2SO_4 maintained at 920°C. For LZO+YSZ, an environment Na_2SO_4+V_2O_5 (90/10 mol percentage) experiment was also performed at 920°C for 10 days - 240 hours. Following the 920°C exposure, corroded specimens LZO+YSZ, GZO+YSZ, LCO+YSZ were tested at a higher temperature of 970°C in the Na_2SO_4 environment. The further hot corrosion experiment time was (4 days – 96 hours) at 970 °C. TBCs dual phase systems LZO+YSZ, GZO+YSZ, LCO+YSZ were tested approximately in a total 342 hours of long-term exposure under hot corrosion of molten Na_2SO_4. For LZO+YSZ in the environment of Na_2SO_4+V_2O_5 (90/10 mol percentage) the experiment was also performed at 970 °C (Na_2SO_4+V_2O_5) for 3 days - 72 hours.

The pure oxidation tests were performed at higher temperatures for prolonged periods. LZO+YSZ (50/50) coatings were tested at high temperature at 1100°C for 10h, 72h, 134h, and 144h. Three types of GZO+YSZ (25/75, 50/50, 75/25) dual phase systems were examined under high temperature oxidation at 1100°C for 48h. 175h, 500h, 1000h, and 2000h. At our knowledge, this was the first time that pure oxidation, for approximately 2000 hours, of GZO+YSZ (25/75, 50/50, 75/25) based dual phase systems was reported. High temperature oxidation tests for LCO+YSZ (50/50) coatings were performed at 950 °C, 1000 °C, 1050 °C, and 1100 °C for 24 hours each interval.

The last hot corrosion experiment was conducted on dual-phase powder mixtures of LZO, LCO, and GZO with a YSZ-based dual phase system. The specific composition of powder mixture for dual phase ceramic powders was prepared and sintered at the temperature ranging from 800 °C to 1400 °C for 24 h of intervals. The powder mixture tablets were liquefied for 15 minutes at the recommended temperature in the first phase. Following that, the specimens were subjected to a cyclic pattern that included 24-hour

exposure cycles to the corrosive environment and a 1-hour pause outside the furnace to allow for cooling. Each pure ceramic powder and its salt-infused counterpart were carefully hand-mixed for 10 minutes using an agate mortar with pestle. Using a manual hydraulic press the combined material was crushed into cylindrical tablets with a diameter (ø) of 10 mm and a height of 2 mm, with a weight of 1 g. These tests on module powder were performed as a confirmatory test to the changes occurring in the dual phase coatings, and the composition of dual phase powders.

3.3. Characterization techniques

The powder specimens were characterized using complementary techniques to assess their properties. Morphology and microstructural features were examined with a Hitachi 3400 N scanning electron microscope (SEM) operated in backscattered electron (BSE) mode. Elemental composition was determined via inductively coupled plasma optical emission spectrometry (ICP-OES; Horiba Ultima 2). Carbon and sulfur content were quantified using a high-temperature combustion analyzer (ON-mat 8500, Strohlein-Labexchange). SEM equipped with an (INCA HKL Nordlys II) EBSD detector. The data acquisition was performed, with EBSD patterns indexed and analyzed using Channel 5 software Phase composition and crystal structure of the as sprayed and corroded samples were analyzed by X-ray diffraction (XRD; Panalytical X'Pert Pro) with Cu Kα radiation ($\lambda = 1.54178$ Å) at 40 kV and 30 mA. Diffraction patterns were collected over a 2θ range of 10°–90° with a step size of 0.02°. Phases were identified by matching the patterns to reference crystallographic data in the ICDD and PDF databases. The differential thermal analysis (DTA) analysis was done using the NETZSCH STA 449 F3 Jupiter thermal analyser. The temperature range of analysis was 40–1200 °C, and the heating and cooling rate was 20 °C min^{-1}.

4. LANTHANUM ZIRCONATE BASED TBCS

4.1. Introduction to LZO based TBCs

In the constant search for increased efficiency and performance in gas turbine and aerospace applications, it is essential to develop novel materials and contemporary thermal barrier coatings (TBCs) that can resist challenging operating environments [1]. TBCs are typically sprayed with a plasma spray process to improve the survival of hot portions of industrial gas turbines, such as blades, vanes, and combustion parts [2]. The components of TBCs are a ceramic topcoat (TC), a thermally sprayed bond coat (BC-MCrAlY), and a substrate composed of nickel-based superalloys. Zirconia stabilized with yttria is the conventional ceramic material used for the topcoat. However, YSZ loses its structural integrity and durability when exposed to high temperatures, reaching up to 1300 °C. This is due to a transition from tetragonal (t′) to monoclinic zirconia (m-ZrO_2) phases, causing a volume expansion of ~ 4 %. To enhance the performance of TBCs, it is vital to achieve lower thermal conductivity, higher thermal stability and cyclic competence, a higher melting point without phase transitions, and chemo-mechanical stability in corrosive environments [3-4]. In response to the increasing demands of the industrial sector, there is a need to explore new ceramic materials with enhanced properties like zirconates, perovskites, and hexaaluminates [5-7]. Lanthanum zirconate (LZO), considered as a promising material for topcoat applications, features a defective fluorite structure that exhibits exceptional thermos-chemical and chemo-mechanical characteristics. LZO can operate at elevated temperatures (>1200 °C) without undergoing phase transitions. In the event of a possible phase transition, typically observed between 1530–1550 °C (from fluorite to pyrochlore), there is minimal impact on the durability and integrity of the coatings [8].

LZO, with a pyrochlore structure, exhibits notable characteristics that make it promising for various applications. Interestingly, LZO exhibits phase structural stability up to an astounding melting temperature of 2300 °C, even at ambient temperature. It also has a lower coefficient of thermal expansion (CTE)— $9.1–9.7 \times 10^{-6}\,K^{-1}$ for LZO and $10.5–11.5 \times 10^{-6}\,K^{-1}$ for 8YSZ with NiCrAlY-BC: $15.0 \times 10^{-6}\,K^{-1}$) - and a lower thermal conductivity (about $\approx 1.5\,Wm^{-1}K^{-1}$) than YSZ ($\approx 2.1\,Wm^{-1}K^{-1}$). The material also

demonstrates resistance to sintering, ensuring its stability over time and maintaining phase stability [9-11]. The crack propagation and delamination occurrence in LZO-TBCs can be attributed to its comparatively lower fracture toughness, measuring at approximately ≈ 1.1 MPa $m^{-1/2}$ for LZO, as opposed to ≈ 2.0 MPa $m^{-1/2}$ for 8YSZ. This inferior fracture toughness reduces resistance to crack growth and separation of layers, ultimately resulting in poor thermal durability of the coatings [12]. Despite its potential, an in-depth examination of existing literature highlights certain limitations when LZO is used as a single-layer TBC. In contrast, employing a single layer of LZO does not meet the established TBC standards, which include a necessity for a higher thermal expansion coefficient, reduced chemical reactivity, and improved fracture toughness. Specifically, at elevated temperatures, a single layer of LZO may react with the thermally grown oxide (TGO) formed at the bond coat-ceramic topcoat interface, resulting in the formation of a porous layer of lanthanum aluminate ($LaAlO_3$) perovskite [13]. This kind of activity is detrimental to the effectiveness of TBCs.

Two recent developments in ceramic insulating layers use bilayer/multi-layer and dual-phase composite coatings. These bilayer/multi-layer coatings combine rare earth zirconate chemicals with conventional YSZ [14-15]. The utilization of two-phase ceramic coatings aims to enhance coating performance and versatility, offering potential advantages in terms of cost and sustainability. Limited literature is available on the behavior of two-phase ceramic TBC systems exposed to isothermal oxidation and hot corrosion environments. Inadequate research has been conducted on the dual-phase LZO + YSZ composite coatings, and the data available in the literature makes it challenging to make conclusive comments on their performance [16-17].

TBCs are prone to corrosion at high temperatures, including liquid salt deposits during corrosion and CMAS (calcium-magnesium-alumino-silicate) corrosion. Molten salts or liquid salt deposits corrosion occurs when contaminants such as Na, S, and V from low-quality fuels deposit on TBC surfaces, forming acidic or basic molten salts. A corrosive material comprising CaO, MgO, Al_2O_3, and SiO_2 causes CMAS corrosion. Glassy CMAS melts are created when siliceous elements, such as sand, dust, and volcanic ash, collect on the surface of hot section components over 1200 °C. Both types of corrosion pose challenges to the durability and performance of TBCs [18-19]. According to Liu et al. [20], the presence of V_2O_5 and Na_2SO_4 accelerates the corrosion process. It induces a phase transition within

two hours at temperatures 700 to 1000 °C. Nevertheless, no obvious reaction or phase shift was seen after two hours of exposure to pure Na_2SO_4 in the air at 900 °C and 1000 °C.

Vasen et al. [21] highlights the potential of using a YSZ/LZO double-layer TBC system; the inner layer provides thermal insulation while the outer provides superior thermo-mechanical properties and enhances the thermal durability of high-temperature components. Song et al. [22] designed the LZO/YSZ blended layer and proposed that these layers are more suitable for shielding the substrate from contact with corrosive conditions. One of the newest methods for ceramic insulating layers is dual-phase high-temperature ceramic composite coatings, which blend common YSZ with rare earth zirconate compounds. Few articles (where YSZ-LZO) on the behavior of dual-phase composite coatings YSZ/LZO in the form of TBC systems under a hot corrosion environment (Na_2SO_4 +V_2O_5) are investigated [16]. Jasik et al. [17] examined the iso-thermal oxidation of YSZ/LZO composite coatings and identified phase stability, mutual interaction between the two structural elements, and interface interactions in the spalt-to-spalt boundaries as critical elements to examine when examining the durability of composite systems.

Mousavi et al. [23] investigated the hot corrosion resistance of LZO + CSZ composite coatings at 950 °C in the presence of Na_2SO_4 + V_2O_5 molten salts (where CSZ= ceria stabilized zirconia-lanthanum zirconate). Microstructural analyses revealed that the combination of CSZ and LZO significantly improved the hot corrosion performance of the LZO coatings. Parchovianský et al. [24] presented their findings regarding dual-phase LC-YSZ composite coatings (where LC=$La_2Ce_2O_7$). La_2O_3-CeO_2-ZrO_2 (LCZ), a novel pyrochlore phase, emerged after the hot pressing of the LC-YSZ mixed powders due to interactions between YSZ and LC, detected by XRD patterns. The produced composites showed an average grain size of less than 1.1 μm, indicating a rather small-grained structure. The LC-40YSZ bulk sample has the lowest thermal conductivity in the 400–1000 °C temperature range.

To address current vulnerabilities in TBCs, the development of bi-layer/multi-layer ceramic TBCs, composite dual-phase TBCs, and modifications through thermal spray techniques are recommended solutions. Various deposition methods are employed for applying TBCs, including high-velocity oxygen fuel (HVOF), atmospheric plasma spraying (APS), vacuum plasma spraying (VPS), suspension plasma spray (SPS), and electron beam physical vapor deposition (EB-PVD) [25-26]. While APS is a faster, more affordable deposition method with better thermal insulation behavior than others, EB-PVD produces

coatings with higher strain tolerance and heat cycle oxidation life. [27]. This study expands the analysis of dual-phase TBCs under hot corrosion conditions; the research gaps include investigations on the composite LZO+YSZ. Previous works only focus on monolayers, FGCs, multi-layer coatings, and YSZ stabilizers; however, deep investigations on the mechanism of dual-phase hot corrosion are missing. In this study, the work investigates LZO+YSZ in both Na_2SO_4 and Na_2SO_4+V_2O_5 conditions, aiming at the enhancement of corrosion-resistant material performance in extremely harsh environments.

4.2. Results and discussion.

4.2.1. Characterization of feedstock powders

A thorough examination of powders used in the TBCs systems' deposition showed that the feedstock materials were of the highest quality. **Figure 4.1**. displays (SEM) images revealing the morphologies of the powders and an electron-dispersive X-ray spectroscopy graph illustrating the elemental compositions in the samples. These visuals confirm the powders' capacity to generate high-quality coatings and their compatibility with spray guns. The SEM microstructure of the powdered YSZ and LZO raw feedstock material is shown in **Figure 4.1**. S-3400N took powder SEM images to 25.0 kV at 100x magnification. These SEM images show a macroscopic perspective of the YSZ and LZO particles, exhibiting their surface forms and dispersion throughout the sample. YSZ and LZO powder materials have a spherical shape with voids and a varied size distribution. These materials demonstrate good influencing characteristics, including flowability, packing density, and sintering behavior. However, slight variations are visible on the outside of both samples, suggesting small aberrations in their geometry. Moreover, flattened granules and individual spherical particles are visible.

The tetragonal phase for the YSZ was seen in EBSD **Figure 4.1.** There are 137 space groups. This space group is represented by the Hermann-Mauguin notation as I41/amd, or 4/mmm. This space group represents a crystal with extra mirror planes and a 4-fold rotating axis. This space group is typical of tetragonal crystals. The space and Laue groups have the same tetragonal symmetry, which is 5. This suggests that the X-ray diffraction pattern of the crystal has 4/mmm symmetry. The value of the MAD is 0.264°.

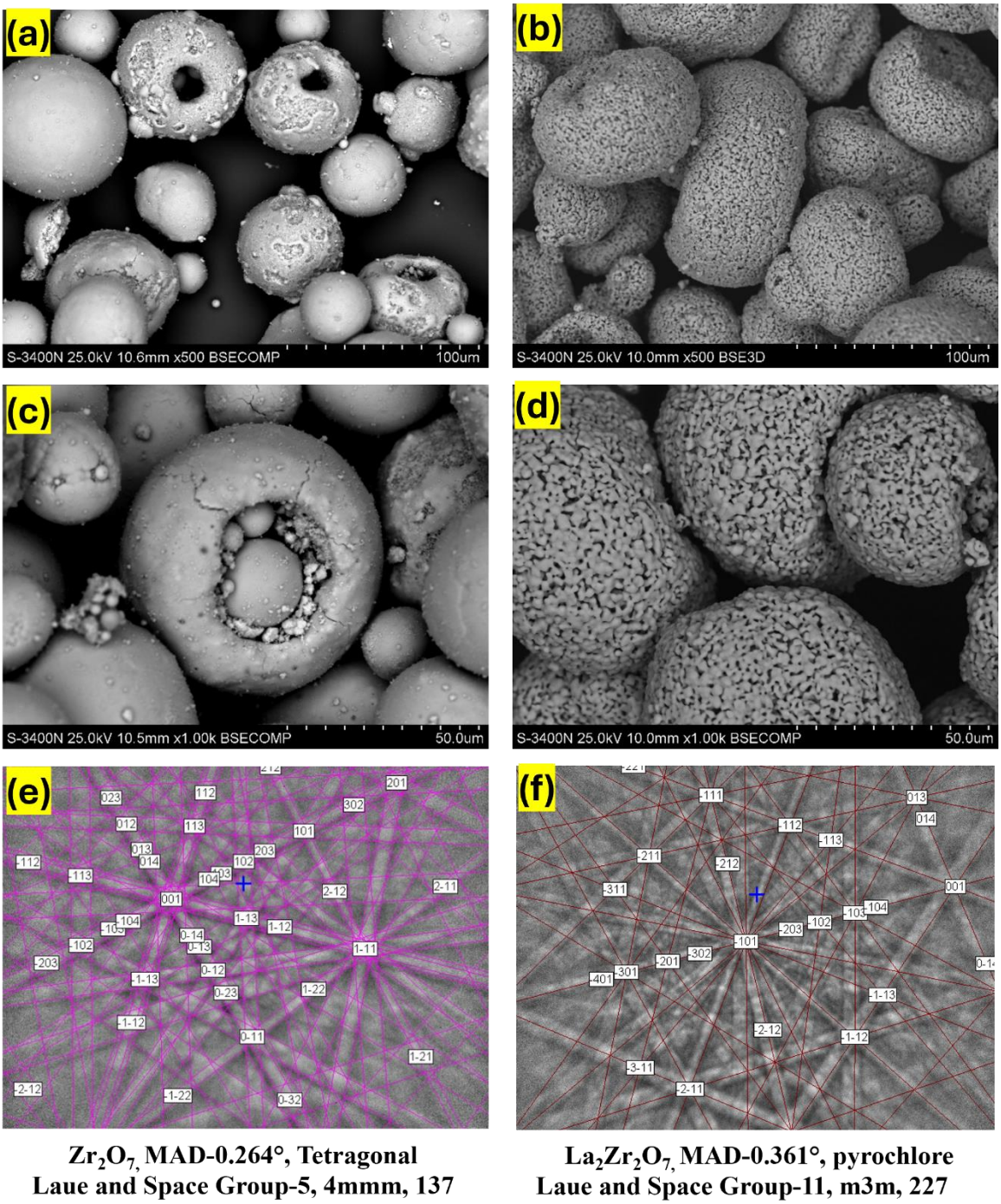

Figure 4.1. SEM micrographs of YSZ (a, c) and LZO (b, d) powders: high-resolution SEM images of powders at 100 µm and at 50 µm. Kikuchi lines: EBSD (electron backscattered diffraction) method. (e-YSZ), (f-LZO)

This number most likely represents the angular difference between anomalous diffraction data obtained at various X- ray wavelengths. However, compared to EBSD, LZO exhibits a pyrochlore structure, a distinctive crystal arrangement often characterized by a cubic lattice. The crystallographic properties of LZO were investigated using EBSD, revealing a mean angular deviation (MAD) of 0.361°.

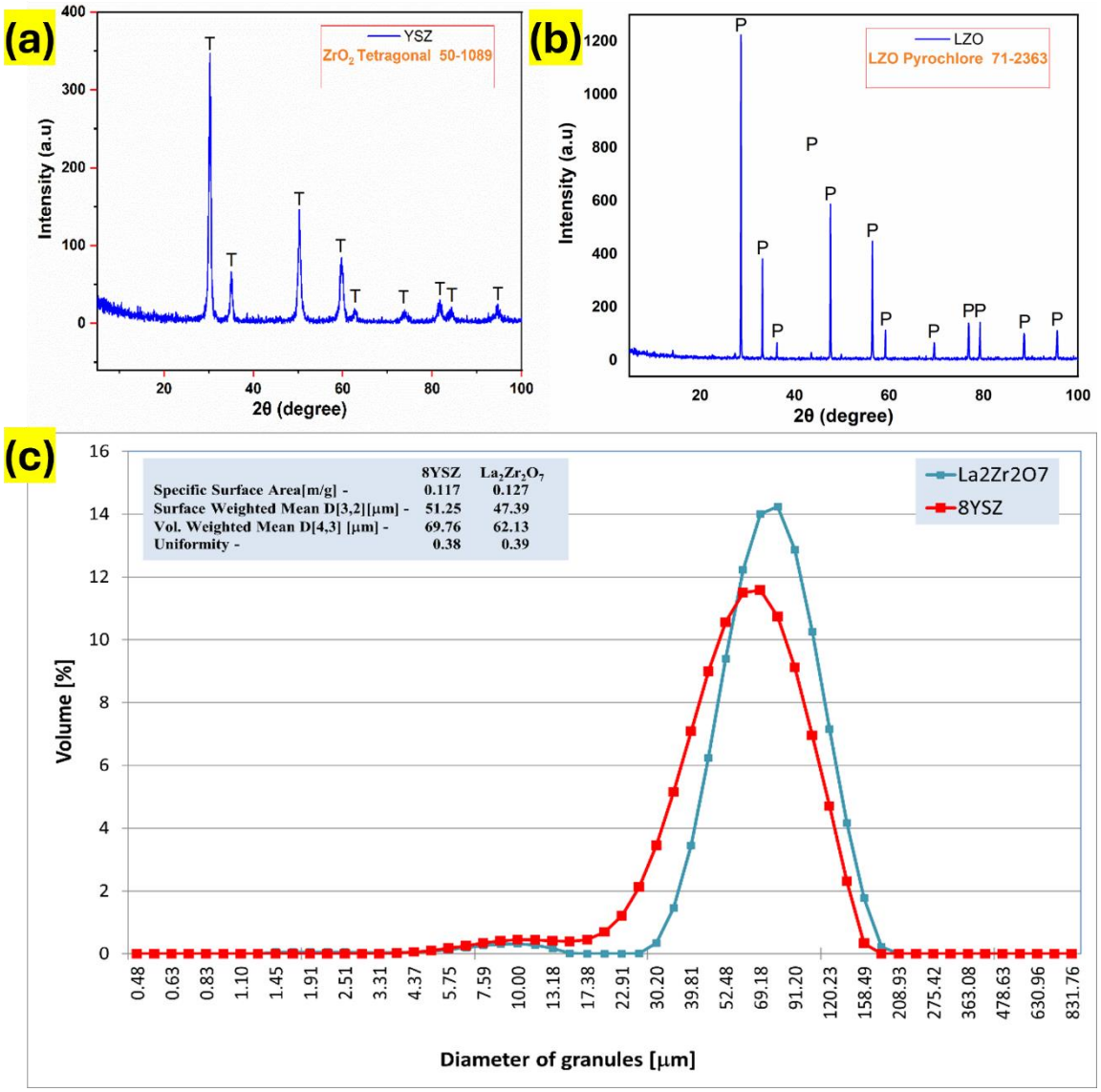

Figure 4.2. XRD Patterns for YSZ (a) and LZO (b) powders, indicating their phase composition. (c)Particle size measurement via Master Sizer

Regarding its symmetry, LZO belongs to the Laue Group 11 and has a space group denoted as m3m, with a corresponding space group number of 227. This signifies a cubic crystal lattice with high symmetry, providing valuable insights into the structural characteristics of this pyrochlore compound.

As illustrated in **Figure 4.2.** powder X-ray diffraction patterns were employed for phase composition analysis. The diffraction pattern for LZO revealed the presence of a cubic $La_2Zr_2O_7$ phase with a pyrochlore lattice structure, consistent with ICDD card number 71-2363. In contrast, the analysis of YSZ showed a tetragonal phase of zirconium oxide, with the predominant phase exhibiting a tetragonal lattice structure, as confirmed by ICDD card

number 50-1089. An additional crucial aspect regarding the powders utilized in APS-based coating deposition is the distribution of granule or particle sizes. This parameter holds particular significance, especially in the context of dual-phase composite coatings, particularly when diverse feedstock materials are employed. The primary concern is ensuring the microstructure's homogeneity, requiring a uniform distribution of structural elements. In this context, both powders under examination demonstrate high similarity, suggesting an anticipated even distribution of LZO and YSZ splats. As shown in **Figure 4.2.** the particle size distribution for both YSZ and LZO powders falls within the same range.

4.2.2. Characterization of as deposited and corroded samples

The fundamental objective of the experiment was to analyze the surface degradation mechanisms involved in the corrosion of TBC composite coatings, specifically those composed of a combination of lanthanum zirconate and zirconium oxide in a 50/50 ratio. The investigation was conducted in an environment consisting of liquid sodium sulfate (Na_2SO_4) and a mixture of 90% Na_2SO_4 and 10% V_2O_5. While there is a substantial body of literature on the corrosion of TBC systems, none has explored the influence of pure Na_2SO_4 and Na_2SO_4+V_2O_5 in the degradation process for the two-phase TBC composite systems. Furthermore, information is absent regarding the initial degradation processes in pure liquid deposits of various sulphate, such as sodium sulphte, especially in the context of emerging ceramic insulation layer materials like zirconates and cerates. This study emphasizes coatings involving composite mixtures of the YSZ+LZO system.

4.2.3. The overall strength and reliability of TBCs

Upon visual inspections of the top-coat surfaces in the insulation layer of TBCs-type YSZ+LZO coatings, no apparent microstructural alterations indicative of typical hot corrosion processes was observed. The surface integrity remained satisfactory, characterized by limited spallation and minimal effects associated with crack initiation and propagation along the edges. **Figure 4.3.(a-d)** illustrates the surface morphology of the deposited coatings. Backscattered electrons' colour contrast enables the differentiation of YSZ-related splats (appearing dark) from those associated with $La_2Zr_2O_7$ (appearing bright). The cross-sectional views of the TBCs system are shown in **Figure 4.4.(a-d)** Based on the microstructures and phase compositions observed, APS sprayed coatings were effectively fabricated with the specified $La_2Zr_2O_7$ + YSZ contents and orientations. Notably, the sole

observable impact on the surface of the insulation ceramic layer was a variation in colour among ceramic materials and slight cracking attributed to edge effects after 920 °C as the temperature increases from 920° to 970°C the robustness in a variation of colour and spallation, with a crack at the surface increases. These observations can be seen in **Figure 4.5.**—the macrographs from the conclusive visual inspection after exposure at temperatures of 920 °C and 970 °C.

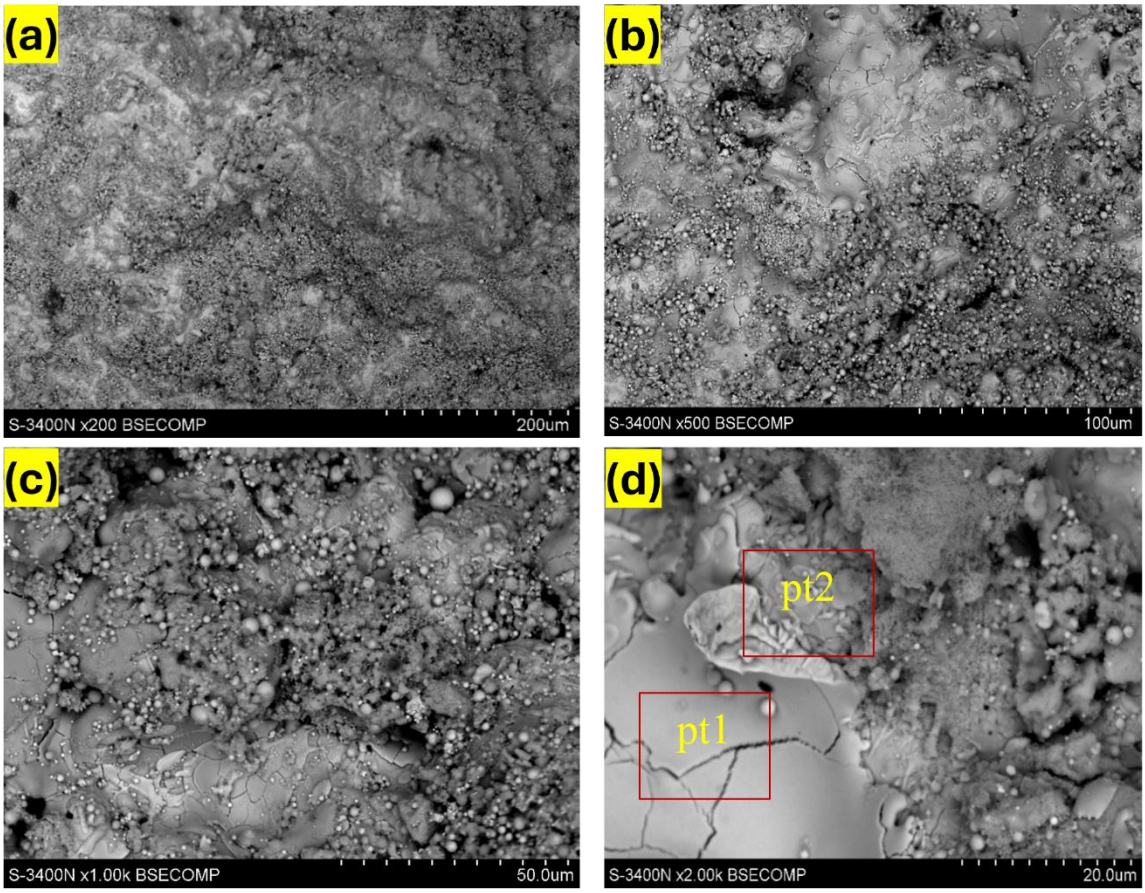

Weight %	O-K	Y-L	Zr-L	La-L
LZO+8YSZ_pt1	20.2	1.0	35.3	43.5
LZO+8YSZ_pt2	20.2	1.2	35.6	43.0

Atomic %	O-K	Y-L	Zr-L	La-L
LZO+8YSZ_pt1	63.9	0.6	19.6	15.9
LZO+8YSZ_pt2	63.9	0.7	19.7	15.7

Figure 4.3. SEM Micrographs of YSZ-LZO dual phase coatings: SEM top surface morphology, top surface EDX morphology

The top surface morphology **Figure 4.3.** included dual-phase splats, globular pores nestled between splats (originating from the entrapment of gas and non-molten particles), cracks within splats (stemming from stresses released during the rapid cooling of sprayed granules), and gaps (cracks) between splats (associated with poor wettability or adhesion among splats). The TBC cross-sections in **Figure 4.4.** rightly illustrates these structural components. **Figure 4.3.** represents the composite coatings' top morphology, comprising $La_2Zr_2O_7$ and 8YSZ in variable proportions, exhibited homogeneous microstructures with randomly dispersed regions of the two ceramic compounds. No apparent tendency was observed for substantial localization or clustering of individual ceramic constituents. The thickness of all coatings within this group remained consistent and uniform across the analyzed region. Another critical factor is the distribution of pores and voids. No significant porosity was detected, with pores, cracks being randomly distributed throughout all TBC cross-sections. The shape and morphology of pores were consistent across all the coatings samples.

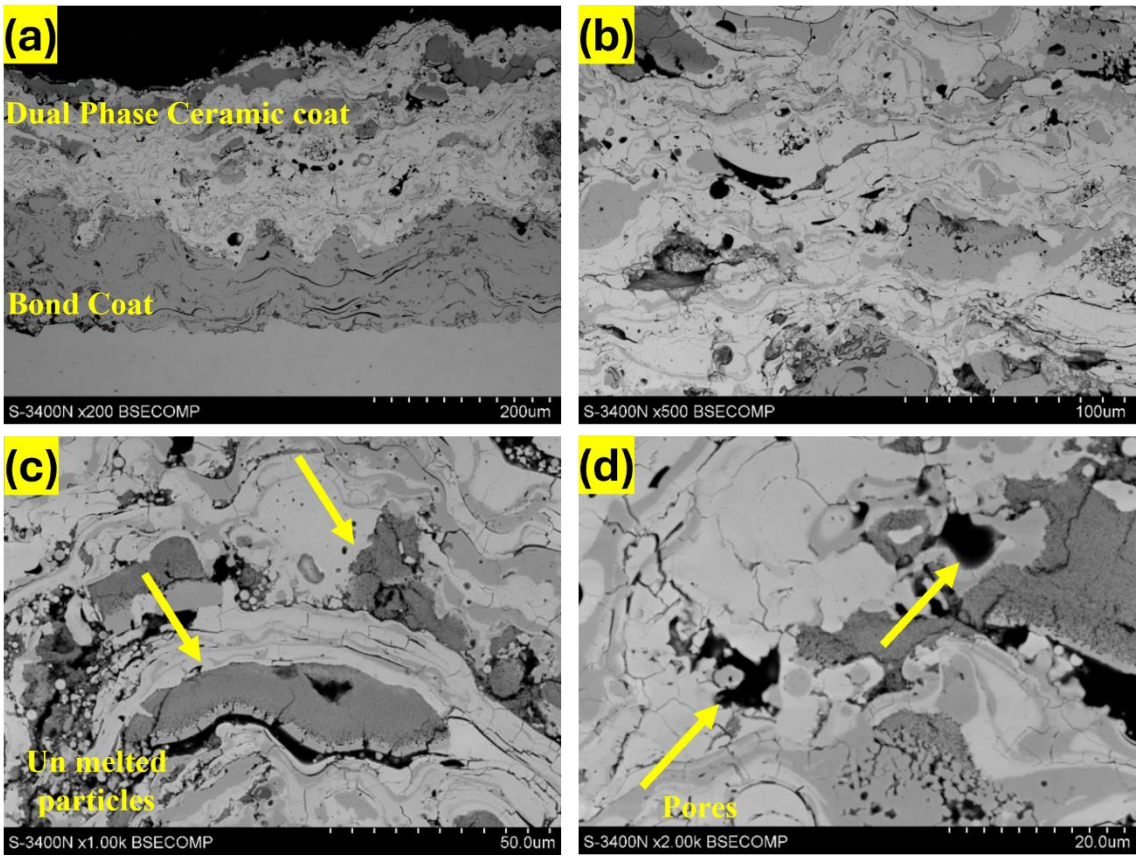

Figure 4.4. SEM micrographs of YSZ-LZO dual phase coatings: SEM cross sectional surface morphology

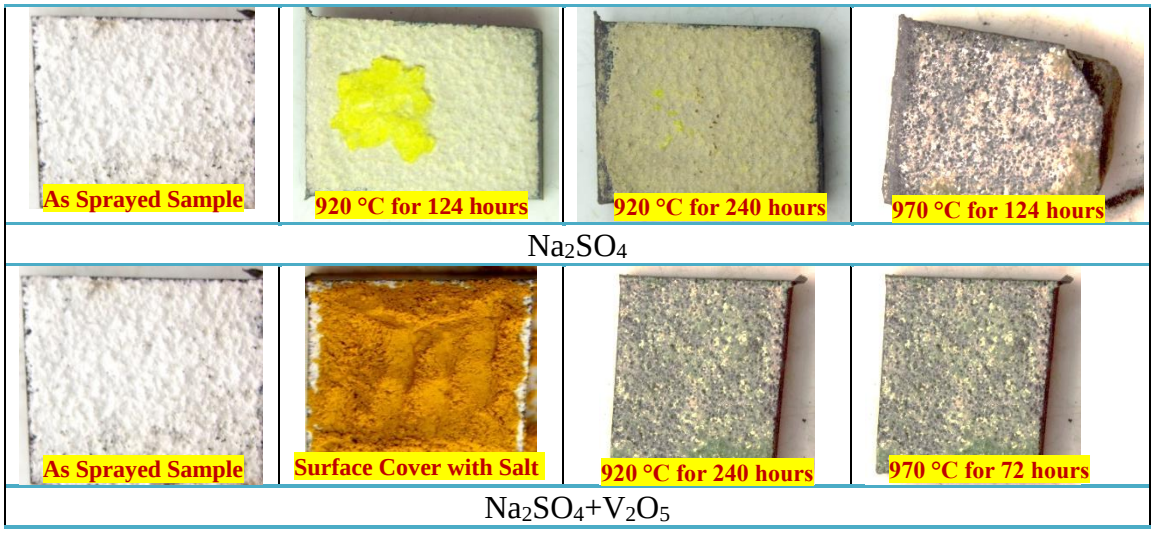

Figure 4.5. Stereomicrograph of YSZ-LZO dual phase coatings: Images of the examined surface coatings following exposure to high-temperature corrosion testing in (Na_2SO_4+V_2O_5) corrosion environment at temperatures of 920 °C for 240 hours and 970 °C for 72 hours.

4.2.4. Examining the stability of phases in LZO+YSZ

During XRD investigations of YSZ+LZO dual phase TBCs system, interesting phenomena were observed. YSZ+LZO dual phase TBCs demonstrated a high degree of dual phase stability at temperatures of 920 °C and 970 °C. After hot corrosion at 970 °C, secondary phases occur; however, the two primary phases, pyrochlore and tetragonal, do not initiate any mutual interaction during hot corrosion. This effect can be seen in **Figure 4.6.** which shows that pyrochlore zirconate in cubic system JCPDS 71-2363 and tetragonal zirconia JCPDS 50-1089 are not involved in the dissolution process with each other. Compared to our prior research on dual-phase composite systems like SZO+YSZ [28], NZO+YSZ [29], and GZO+YSZ [30], the dual-phase systems of samarium, neodymium and gadolinium were not stable under hot corrosion and even in pure oxidation. A regular observation has been made through our exploration of dual-phase systems based on varying mole percentages (25/75, 50/50, and 75/25). Specifically, it has been noted that the 50/50 mole percentage composition leads to robust chemical reactivity in these SZO, NZO, and specially in GZO -YSZ systems. This is also one of the reasons that this research was based on the 50/50 mol percentage LZO/YSZ; only the corrosion environment and temperature were varied.

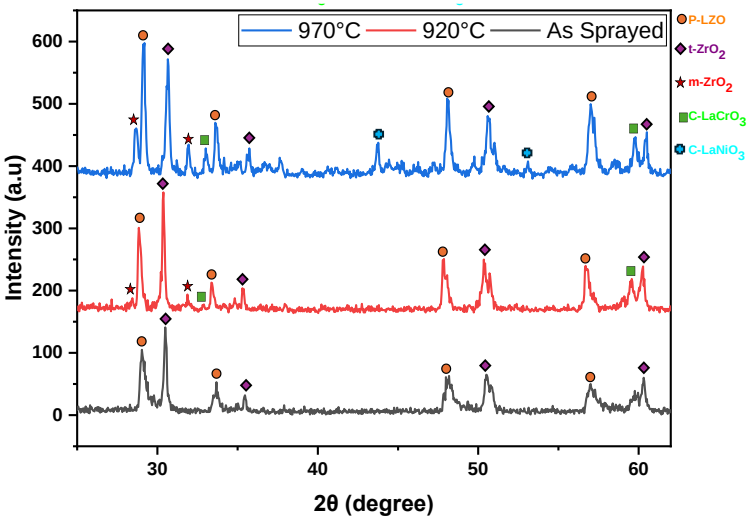

Figure 4.6. XRD patterns of 8YSZ + LZO coatings in as-sprayed condition and after exposure to Na_2SO_4 at 920°C and 970°C.

This discovery is significant, given that existing literature has not previously reported such occurrences in analogous coatings. It is important that these processes were conspicuously absent in monolayered 8YSZ and $La_2Zr_2O_7$ coatings. The TBCs systems under examination exhibit unique characteristics, introducing a novel aspect to discussing their structural behavior. The coatings are stable at higher temperatures with liquid salt deposits. However, this is not the only mechanism that degrades dual-phase TBCs systems; the literature references [31-33] suggest that as temperatures increase, various considerable processes contribute to the deterioration of TBCs. These include dissociating salt species and potentially introducing corrosive elements into the coating environment. Moreover, through further investigation, the formation of rare earth oxides, specifically $LaCrO_3$ (JCPDS 75-0441) and $LaNiO_3$ (JCPDS 33-0710), have been identified. These oxides exhibit a pronounced interaction with LZO and are diffused from the TGO zone. Importantly, the corrosion products, $LaCrO_3$ and $LaNiO_3$, prove detrimental to the LZO+YSZ zirconia system, leading to the conversion of pyrochlore LZO into a fluorite form. This comprehensive understanding of degradation mechanisms contributes to the broader discussion of structural behavior in advanced thermal barrier coatings.

Interestingly, this is the first publication to mention TGO interaction with topcoat ceramic zirconate in dual phase composite coatings; in our earlier research, we had not detected this interaction. Second, EDX investigations verify the aforementioned observations that the formation of corrosion products $LaCrO_3$ is identified at lower temperatures (920 °C) and $LaNiO_3$ is created at higher temperatures (970 °C) in the corrosion environment of pure Na_2SO_4. However, the same observation was different in the presence

of V_2O_5. These corrosion products' thermodynamic and kinetic properties determine distinct phases' stability and formation. The literature has extensively examined $LaNiO_3$ [34] at higher temperatures and $LaCrO_3$ [35] at lower temperatures; however, this is outside the scope of our work. The elemental mapping and EDX analysis in **Figures 4.7. and 4.8.** depict the top surface morphology that supports the formation of corrosion products during the degradation process.

To ascertain the elemental compositions of the hot corrosion products, an analysis using energy-dispersive X-ray spectroscopy was conducted at different regions on the surface of the topcoat after exposure to temperatures of 920 °C and 970 °C. The elemental analysis results for points 1, 2, 3, and 4 (as illustrated in **Figures 4.7. and 4.8.**) are presented. The dual phase system of LZO+YSZ is inert but considering the presence of clustered elements in the EDX maps and the environmental conditions involving Na_2SO_4, Na_2SO_4+V_2O_5, some other corrosion mechanisms come into play. In environments rich in vanadium and sulfate, vanadate corrosion products are frequently generated, which are indicated by XRD. Vanadate compounds have the capacity to accelerate corrosion by facilitating oxygen diffusion, thereby promoting rapid corrosion within the temperature range of 600-800 °C. The detection of clusters containing vanadium and other elements in the EDX maps implies that vanadate corrosion could significantly contribute to the observed corrosion effects. Sulfur compounds like sulfates have the propensity to react with metal components, forming sulphate compounds. These sulphates might account for the observed clustered regions in the EDX maps, thereby expediting corrosion processes, particularly in environments containing sulfur species. The presence of sodium in salt baths can influence melting temperatures, leading to the formation of molten layers atop the coating surfaces. Molten salt corrosion has the potential to modify corrosion effects by fostering the creation of corrosive species and impacting the stability of passivation layers. This mechanism might also be implicated in the clustering of elements seen in the EDX maps. Additionally, chromate, vanadate, or nickel-based compounds identified through pure XRD results from the study also contribute to corrosion effects. These compounds may engage with the coating material and substrate, instigating localized corrosion and the formation of element clusters in the EDX maps.

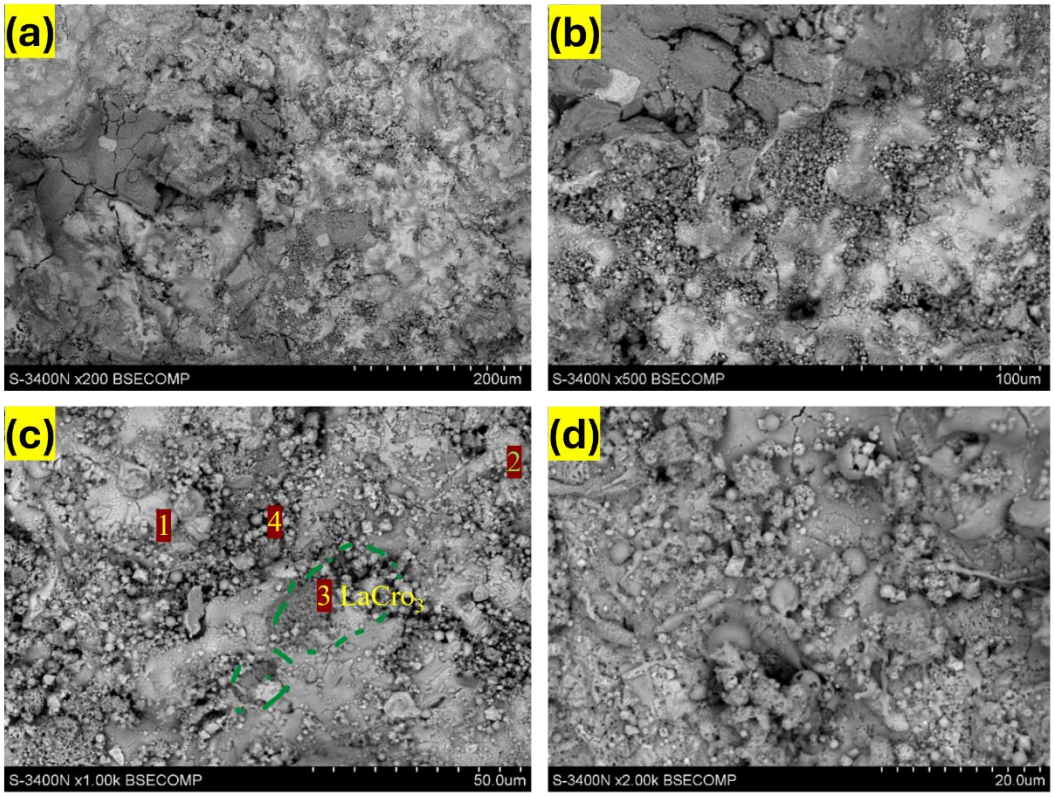

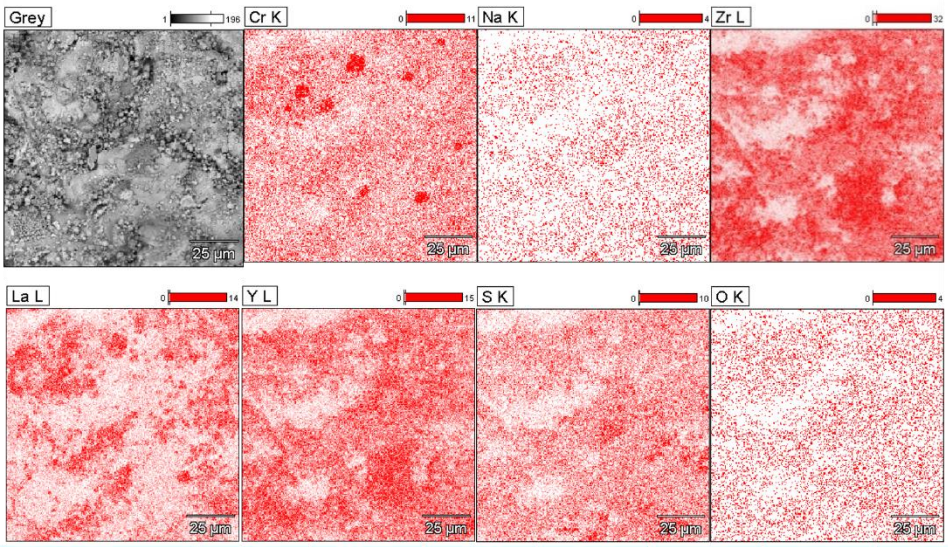

Weight %	O-K	Na-K	S-K	Cr-K	Y-L	Zr-L	La-L
Na_2SO_4-920C_pt1	20.9				2.2	39.4	37.5
Na_2SO_4-920C_pt2	23.7		0.2		3.7	55.5	16.9
Na_2SO_4-920C_pt3	28.0	1.1	5.1	4.1	2.7	51.5	7.5
Na_2SO_4-920C_pt4	23.9		0.6		3.0	54.4	18.2

Atomic %	O-K	Na-K	S-K	Cr-K	Y-L	Zr-L	La-L
Na_2SO_4-920C_pt1	64.2				1.2	21.2	13.3
Na_2SO_4-920C_pt2	65.5		0.3		1.8	27.0	5.4
Na_2SO_4-920C_pt3	65.3	1.7	5.9	2.9	1.1	21.0	2.0
Na_2SO_4-920C_pt4	65.7		0.8		1.5	26.2	5.8

Figure 4.7. Top surface morphology of YSZ-LZO dual phase coatings: SEM images of the examined top surface coatings following the exposure in pure sodium sulfate environment at temperatures of 920 °C for 240 hours. Elemental mapping images of TBCs.

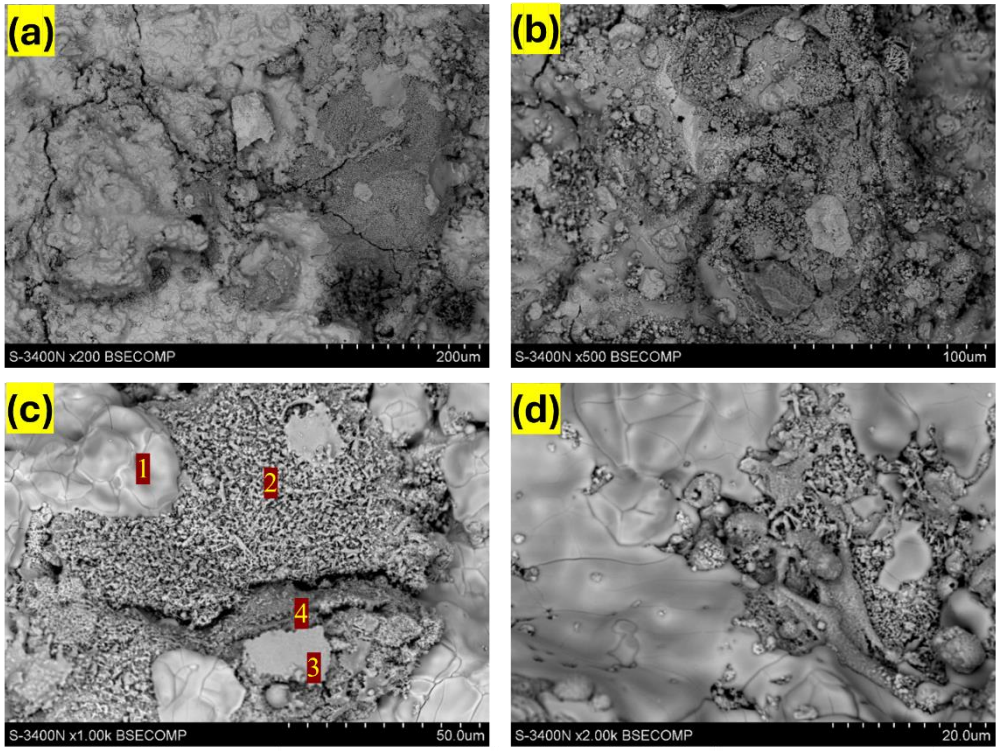

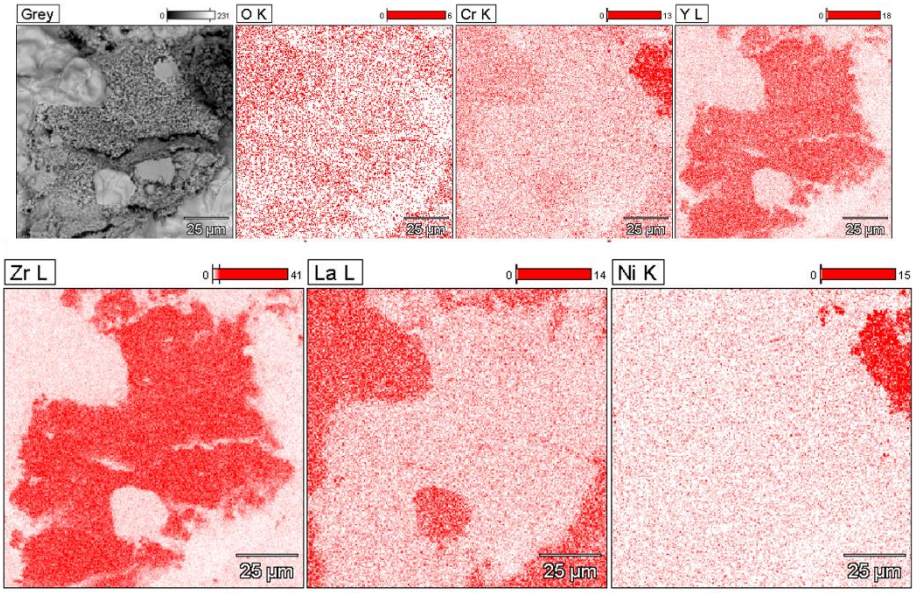

Weight %	O-K	Na-K	S-K	Y-L	Zr-L	La-L
Na_2SO_4-970C_pt1	8.6	0.3	49.4	0.5	6.7	34.5
Na_2SO_4-970C_pt2	26.8		2.1	3.4	61.8	5.9
Na_2SO_4-970C_pt3	27.1		2.5	4.2	60.5	5.8
Na_2SO_4-970C_pt4	27.8		3.3	4.1	59.4	5.5

Atomic %	O-K	Na-K	S-K	Y-L	Zr-L	La-L
Na_2SO_4-970C_pt1	38.4	1.1	37.0	0.4	5.3	17.8
Na_2SO_4-970C_pt2	67.0		2.7	1.5	27.1	1.7
Na_2SO_4-970C_pt3	67.1		3.1	1.9	26.3	1.6
Na_2SO_4-970C_pt4	67.5		4.0	1.8	25.3	1.5

Figure 4.8. Top surface morphology of YSZ-LZO dual phase coatings: SEM images of the examined top surface coatings following exposure in Na_2SO_4 at temperatures of 970 °C for 96 hours. Elemental mapping images of TBCs

The system LZO+YSZ was exposed to a more corrosive environment composed of 90 mol% sodium sulfate and 10 mol% vanadium oxide to evaluate additional stability. Surprisingly, the stability remained unaffected, and there was no observable mutual interaction between YSZ and LZO under these aggressive conditions. The details refer to **Figure 4.9** (P) JCPDS 71-2363, t-ZrO_2 JCPDS 50-1089.

Figure 4.9. - 4.11. present the outcomes of the investigation conducted in an environment containing Na_2SO_4 + V_2O_5. In the robustly corrosive setting with vanadium oxide, the fabricated coatings exhibit stability concerning their mutual interaction. However, other degradation processes, forming various corrosion products, are crucial in this environment. In **Figure 4.9.** at 920 °C, a notable transition was observed in the non-stoichiometric curve, which transformed into a stoichiometric curve around 2θ ≈ 30°. The analysis identifies the formation of lanthanum vanadate (JCPDS 50-0367) and monoclinic zirconia (JCPDS 50-1089) at 920 °C. The experiment was continued at 970 °C for only 3 days because a macroscopic examination revealed spallation initiation at the edges. In terms of XRD interpretation, final corrosion products including $LaCrO_3$ (JCPDS 75-0441), $LaNiO_3$ (JCPDS 33-0710), La_2O_2S (JCPDS 75-1930), and m-$LaVO_4$ (JCPDS 50-0367) have been identified. These investigations highlight the formation of $LaCrO_3$ and $LaNiO_3$ at higher temperatures (970 °C) in the presence of vanadium. This is attributed to vanadium undergoing other thermodynamically more stable reactions that XRD analysis can easily detect. Furthermore, the formation of $LaCrO_3$ [34], $LaNiO_3$ [35], La_2O_2S [36], and $LaVO_4$ [37] at higher temperatures is thermodynamically referenced in the literature.

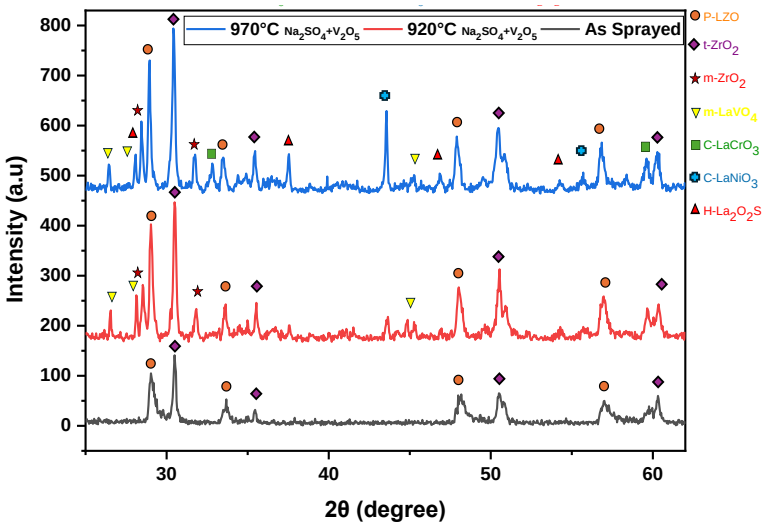

Figure 4.9. XRD patterns of 8YSZ + LZO coatings in as-sprayed condition and after exposure to Na_2SO_4 + V_2O_5 at 920°C and 970°C.

To ascertain the elemental compositions of the hot corrosion products, the same analysis using energy-dispersive X-ray spectroscopy (as used in previous case) was conducted at different regions on the surface of the topcoat after exposure to temperatures of 920 °C and 970 °C. The elemental analysis results for points 1, 2, 3, 4, 5, and 6 (as illustrated in **Figures 4.10. and 4.11.**) are presented. Hot corrosion, caused by molten salts, can damage protective oxide scales on materials, especially Ni-based superalloys. The fluxing mechanism, analogous to aqueous corrosion, involves a liquid phase that weakens and accelerates oxide breakdown.

Model systems composed of $La_2Zr_2O_7$, 8YSZ, and Na_2SO_4 powders were investigated further; to validate the obtained coatings results and confirmation was made through accelerated decomposition phenomenon. The model powder component proportions were 50/50 mol percentage, 45/45/10 mol percentage, and 45/45/9/1 mol percentage, respectively. The powders were homogenized, pressed into pellets, and subsequently subjected to heat treatment from 800 °C to 1400 °C for 24h, each reference temperature. The overall time duration for sintering was 168 hours as each pellets sintered for one cycle from 800 °C to 1400 °C.

Figure 4.12. (a, b, c) shows XRD patterns of the phase composition of 100 % 8YSZ, 90% 8YSZ +10% Na_2SO_4, and 90% 8YSZ +9% Na_2SO_4 + 1% V_2O_5. It is revealed that pure 8YSZ remains stable up to 1400 °C. However, when exposed to Na_2SO_4, decomposition begins at around 1000 °C, and its progression is described by the following equations below. However, in the presence of Na_2SO_4+ V_2O_5 minor peaks due to secondary phases around 2θ (28-30) degree, and same decomposition begins at around 1000 °C. But it is not severe as expected due to the very low percentage V_2O_5 (only 1 percent).

$$YSZ + SO3 \rightarrow Y2(SO4)_3 + m\text{-}ZrO_2 \text{ (Degradation)}$$

$$YSZ{+}{+} + 2NaVO3 \rightarrow 2YVO_4 + Na_2O + m\text{-}ZrO_2 \text{ (Degradation)}$$

Na_2SO_4 +V_2O_5 react at elevated temperatures, forming vanadates. These vanadates have significantly lower melting points compared to the individual reactants, typically starting around 535 °C. Additional metal oxides in the mixture can further decrease the melting point, creating molten salt deposits, which can trigger hot corrosion, a damaging process that accelerates material degradation. Molar ratios between Na_2SO_4 +V_2O_5 also influence the corrosion behavior, with specific ratios leading to more aggressive attack.

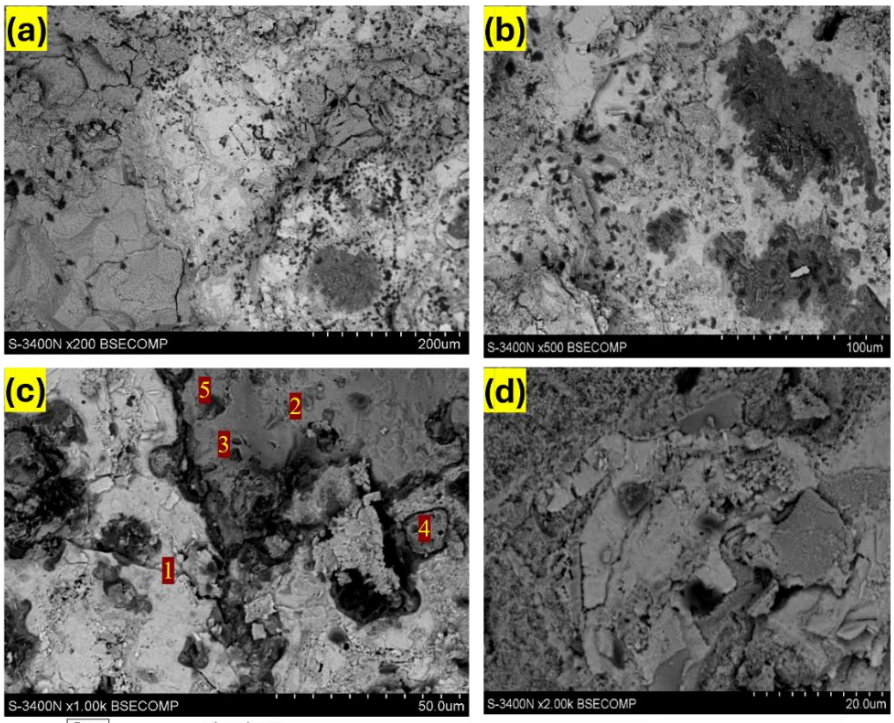

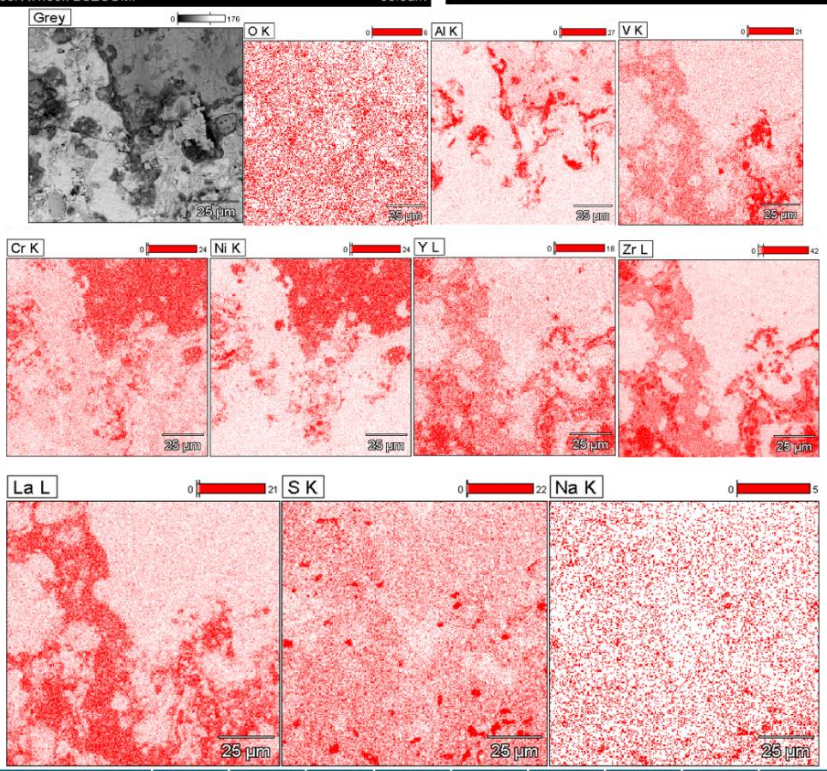

Weight %	O-K	Al-K	S-K	V-K	Cr-K	Ni-K	Y-L	Zr-L	La-L
LZO+YSZ-920C_pt1	20.9	0.4		0.3	2.9	6.2	1.4	29.3	38.6
LZO+YSZ-920C_pt2	25.2	1.0	0.2	0.3	19.4	47.7	0.1	3.6	2.5
LZO+YSZ-920C_pt3	25.4	1.9	0.3	0.3	18.3	45.9	0.5	4.3	3.2
LZO+YSZ-920C_pt4	25.5	1.8	0.2	0.5	19.0	43.7	0.3	5.2	3.7
LZO+YSZ-920C_pt5	33.7	21.3	1.0	0.5	6.4	13.6	6.7	8.9	8.1

Atomic %	O-K	Al-K	S-K	V-K	Cr-K	Ni-K	Y-L	Zr-L	La-L
LZO+YSZ-920C_pt1	62.2	0.8		0.2	2.7	5.0	0.7	15.2	13.2
LZO+YSZ-920C_pt2	54.8	1.3	0.3	0.2	13.0	28.3	0.1	1.4	0.6
LZO+YSZ-920C_pt3	55.2	2.4	0.3	0.2	12.2	27.1	0.2	1.6	0.8
LZO+YSZ-920C_pt4	55.5	2.3	0.2	0.3	12.7	25.9	0.1	2.0	0.9
LZO+YSZ-920C_pt5	59.9	22.4	0.9	0.3	3.5	6.6	2.1	2.8	1.6

Figure 4.10. Top surface morphology of YSZ-LZO dual phase coatings: SEM images of the examined top surface coatings following exposure in $Na_2SO_4 + V_2O_5$ at temperatures of 920 °C for 240 hours. Elemental mapping images of TBCs

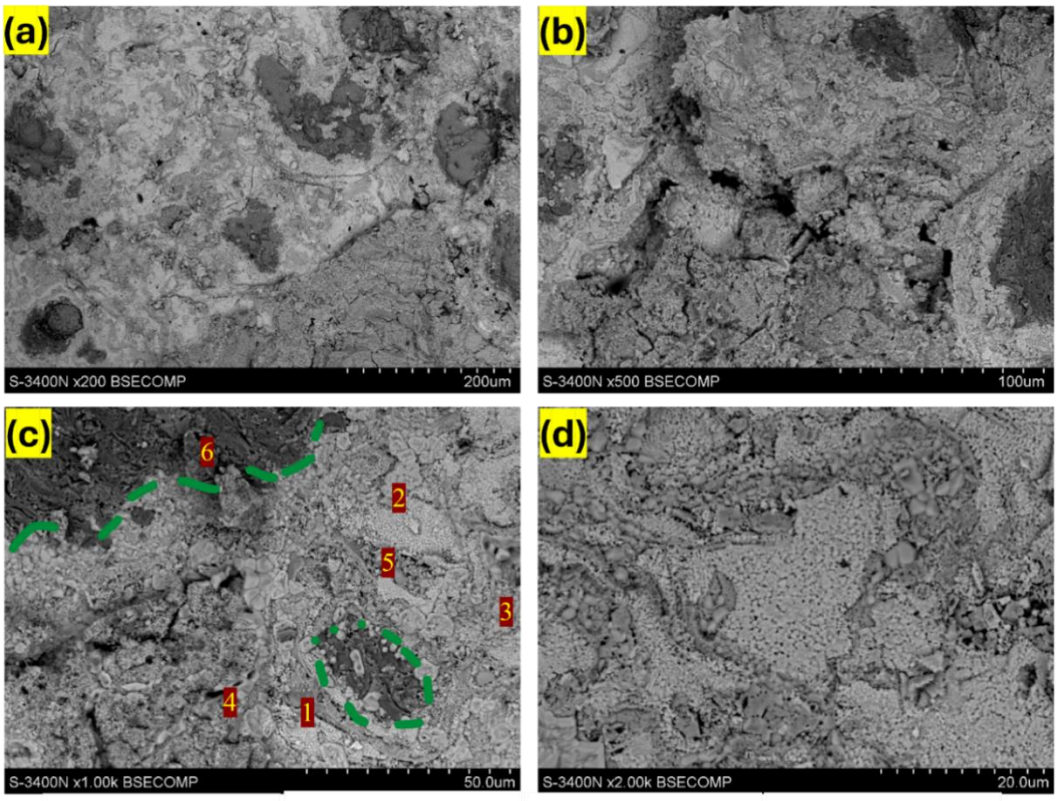

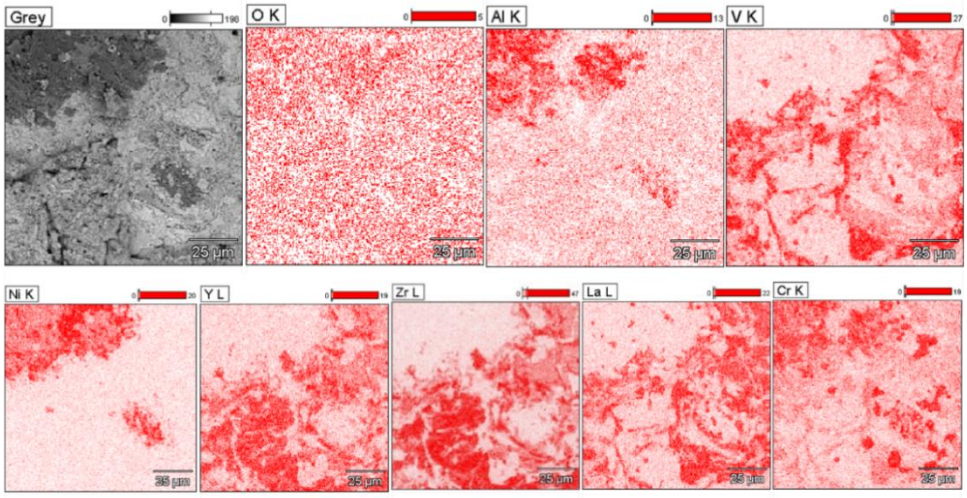

Weight %	O-K	Al-K	V-K	Cr-K	Mn-K	Ni-K	Y-L	Zr-L	La-L
LZO+YSZ-970C_pt1	20.9	0.1	1.6			2.9	1.4	32.3	40.8
LZO+YSZ-970C_pt2	21.9	0.1	1.2	16.9		4.5	0.7	12.3	42.5
LZO+YSZ-970C_pt3	24.7		1.8			4.7	4.5	54.6	9.6
LZO+YSZ-970C_pt4	25.4		2.4			3.5	2.6	58.4	7.7
LZO+YSZ-970C_pt5	24.9		1.5			3.8	2.7	58.0	9.1
LZO+YSZ-970C_pt6	25.8	3.6	0.7	15.5	0.2	41.3	0.5	7.6	4.6
Atom %	**O-K**	**Al-K**	**V-K**	**Cr-K**	**Mn-K**	**Ni-K**	**Y-L**	**Zr-L**	**La-L**
LZO+YSZ-970C_pt1	63.6	0.2	1.6			2.4	0.7	7.2	14.3
LZO+YSZ-970C_pt2	60.9	0.2	1.0	14.5		3.4	0.3	6.0	13.7
LZO+YSZ-970C_pt3	64.9		1.5			3.4	2.1	5.2	2.9
LZO+YSZ-970C_pt4	65.6		2.0			2.4	1.2	6.5	2.3
LZO+YSZ-970C_pt5	65.3		1.2			2.7	1.3	6.7	2.7
LZO+YSZ-970C_pt6	55.8	4.7	0.5	10.3	0.1	24.3	0.2	2.9	1.1

Figure 4.11 Top surface morphology of YSZ-LZO dual phase coatings: SEM images of the examined top surface coatings following exposure in $Na_2SO_4 + V_2O_5$ at temperatures of 970 °C for 72 hours. Elemental mapping images of TBCs

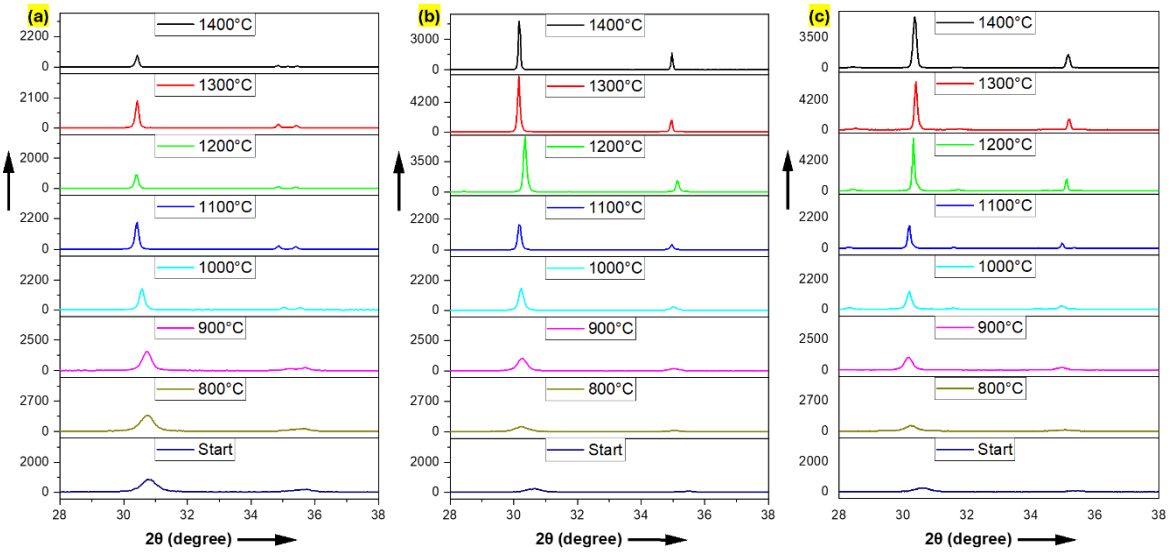

Figure 4.12. (a) XRD patterns for pellets 100% 8YSZ at 800°C,900 °C, 1000 °C, 1100 °C, 1200 °C, 1300 °C, and 1400 °C for 168 h. **(b)** XRD patterns for pellets 90% 8YSZ + 10% Na_2SO_4 annealed at 800°C,900 °C, 1000 °C, 1100 °C, 1200 °C, 1300 °C, and 1400 °C for 168 h. **(c)** XRD patterns for pellets 90% 8YSZ +9% Na_2SO_4 + 1% V_2O_5 annealed at 800°C,900 °C, 1000 °C, 1100 °C, 1200 °C, 1300 °C, and 1400 °C for 168 h.

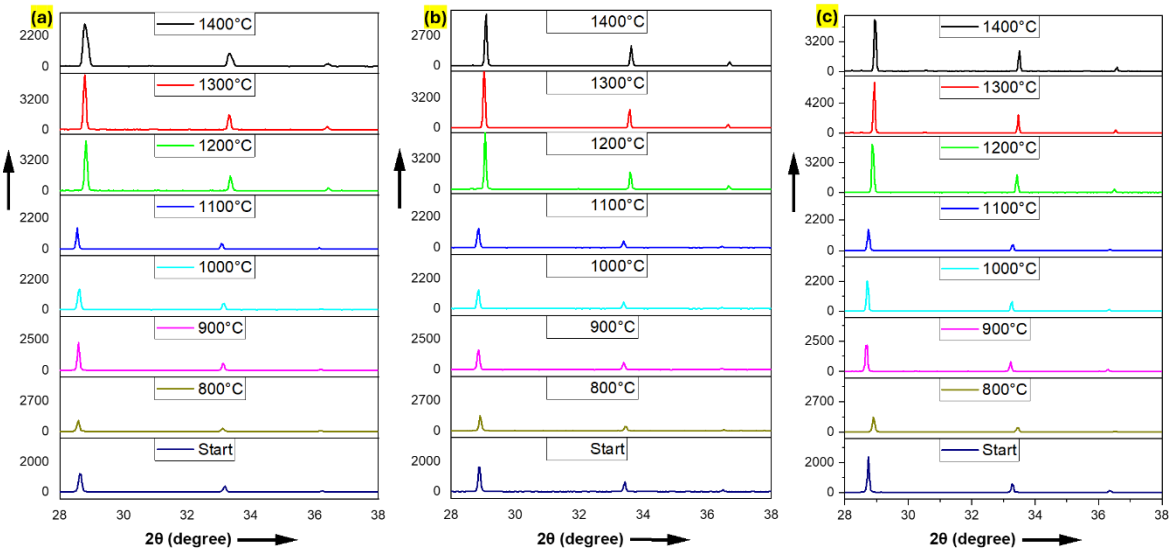

Figure 4.13. (a) XRD patterns for pellets 100% $La_2Zr_2O_7$ at 800°C,900 °C, 1000 °C, 1100 °C, 1200 °C, 1300 °C, and 1400 °C for 168 h. **(b)** XRD patterns for pellets 90% $La_2Zr_2O_7$ + 10% Na_2SO_4 annealed at 800°C,900 °C, 1000 °C, 1100 °C, 1200 °C, 1300 °C, and 1400 °C for 168 h. **(c)** XRD patterns for pellets 90% $La_2Zr_2O_7$ + 9% Na_2SO_4 + 1% V_2O_5 annealed at 800°C,900 °C, 1000 °C, 1100 °C, 1200 °C, 1300 °C, and 1400 °C for 168 h.

Figure 4.13 (a, b, c) shows XRD patterns of the phase composition of 100% LZO, 90% LZO +10% Na_2SO_4, and 90% LZO +9% Na_2SO_4 + 1% V_2O_5. It is revealed that pure LZO remains stable up to 1400 °C. However, when exposed to Na_2SO_4, and Na_2SO_4+ V_2O_5 minor peak appear which suggest presence of defected pyrochlore phases around 2θ (28-30) degree. Both the process YSZ and LZO favor the decomposition in the presence of liquid salts deposits. The XRD patterns of the phase composition of 50/50 mol % $La_2Zr_2O_7$ + 8YSZ

pellets are presented in **Figure 4.14. (a, b, c)**. It suggests that the decomposition due to dual phase interaction between two ceramic LZO and YSZ is absent which is the confirmation of above coatings results.

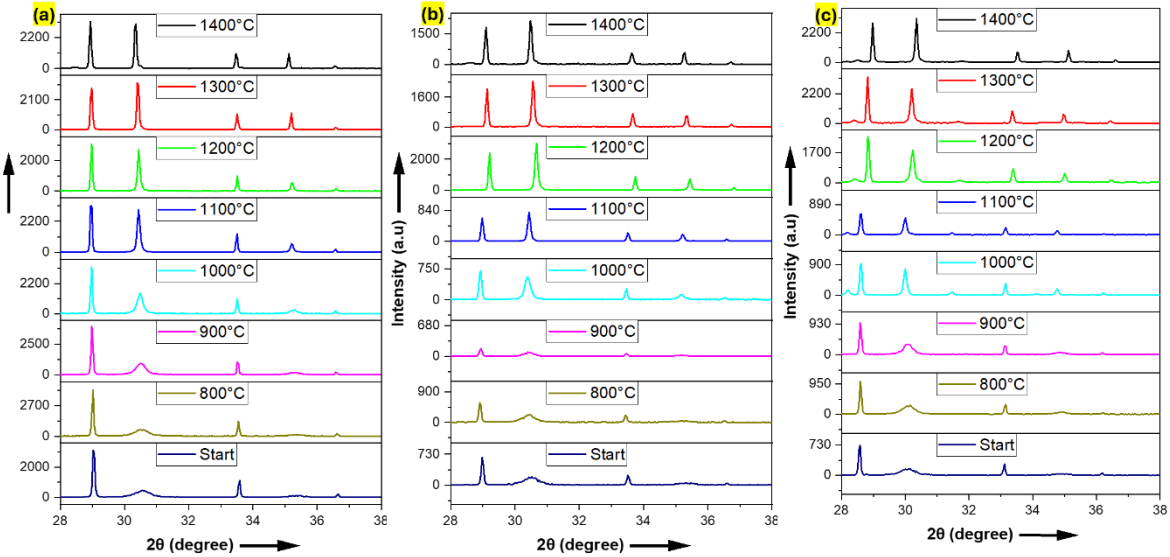

Figure 4.14. (a) XRD patterns for pellets 50 % 8YSZ – 50 % $La_2Zr_2O_7$ annealed at 800°C,900 °C, 1000 °C, 1100 °C, 1200 °C, 1300 °C, and 1400 °C for 168 h. **(b)** XRD patterns for pellets 45 % 8YSZ + 45 % $La_2Zr_2O_7$ + 10% Na_2SO_4 annealed at 800°C, 900 °C, 1000 °C, 1100 °C, 1200 °C, 1300 °C, and 1400 °C for 168 h. **(c)** XRD patterns for pellets 45 % 8YSZ + 45 % $La_2Zr_2O_7$ + 9% Na_2SO_4 + 1% V_2O_5 annealed at 800°C,900 °C, 1000 °C, 1100 °C, 1200 °C, 1300 °C, and 1400 °C for 168 h.

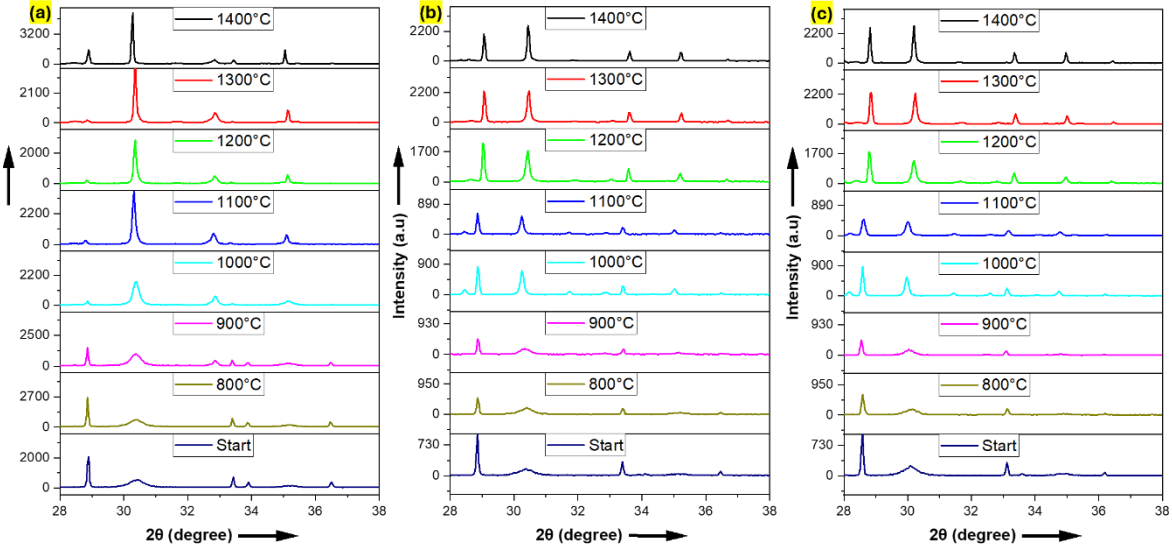

Figure 4.15. (a) XRD patterns for pellets 33.3 % 8YSZ + 33.3 % $La_2Zr_2O_7$ +33.3 % Cr_2O_3 annealed at 800°C,900 °C, 1000 °C, 1100 °C, 1200 °C, 1300 °C, and 1400 °C for 168 h. **(b)** XRD patterns for pellets 40 % 8YSZ + 40 % $La_2Zr_2O_7$ +10% Cr_2O_3+ 10% Na_2SO_4 annealed at 800°C,900 °C, 1000 °C, 1100 °C, 1200 °C, 1300 °C, and 1400 °C for 168 h.**(c)** XRD patterns for pellets 40 % 8YSZ + 40 % $La_2Zr_2O_7$ + 10% Cr_2O_3+ 9% Na_2SO_4 +1% V_2O_5 annealed at 800°C,900 °C, 1000 °C, 1100 °C, 1200 °C, 1300 °C, and 1400 °C for 168 h.

This system is a highly stable system even up to 1400°C. No comparable reactions were observed in the $La_2Zr_2O_7$ + 8YSZ + Na_2SO_4 model system (under hot corrosion conditions), albeit within a narrower temperature range.

Figure 4.14 (a) pure two-ceramic materials, (b) two-ceramic materials in the presence of Na_2SO_4, and (c) two-ceramic materials in the presence of Na_2SO_4+V_2O_5, all of the three cases suggest the stability of the systems, however they are other minor peak related to Na_2SO_4+V_2O_5 phases especially for (c) two-ceramic materials in the presence of Na_2SO_4+V_2O_5 around 2θ (20-30) degree, which due to Vanadium based compounds.

The XRD patterns of the phase composition of 33.3% 8YSZ + 33.3% $La_2Zr_2O_7$ +33.3% Cr_2O_3 pellets are presented in **Figure 4.15. (a, b, c)**., and the phase composition of 33.3% 8YSZ + 33.3% $La_2Zr_2O_7$ +33.3% NiO pellets are presented in **Figure 4.16. (a, b, c)**. There is minor decomposition due to dual phase interaction and with chromium in pure oxidation 15 (a), but in all other cases there is no effect on the dual phase decomposition between two ceramic LZO and YSZ is absent which is the again confirmation of above coatings results. It also suggests that formation of chromites promotes (at the 2 theta 33 degree) the destabilization of LZO, and it transformed into defective fluorite phase (P to F). Differential Thermal Analysis (DTA) experiments were conducted to explore further thermal effects. The analysis involved using a sample mass of 0.1 grams in an air atmosphere, with a heating rate of 10 degrees Celsius per minute. The maximum temperature reached during the experiment was 1200 degrees Celsius. **Figure 4.17.** shows that there is no thermal effect in any case LZO+YSZ, LZO+ Al_2O_3, LZO+ Y_2O_3; there is no interaction between dual phase composite system, and the system remains inert. There is minor chemical reaction in the composition of $La_2Zr_2O_7$ and YSZ compared with Cr_2O_3, NiO which was not detected by XRD and DTA analysis. Further confirmation was made from the dual phase TBCs coatings under pure oxidation at 1100°C for 360 hours of regular time interval sintering. Under pure oxidation there are two ways of transport, the transport of oxygen molecules (O2), through interfacial cracks, pores, splat to splat boundary and oxygen ion (O^{-2}) through dual phase ceramic coatings. The ionic conductivity of LZO is comparatively low up to 100 times at 1000 °C than YSZ, and it reduces the ionic conductivity of dual phase composite system, and an ideal candidate for the dual phase TBCs as compared to other zirconates (ln2Zr_2O_7 where ln =lanthanide series).

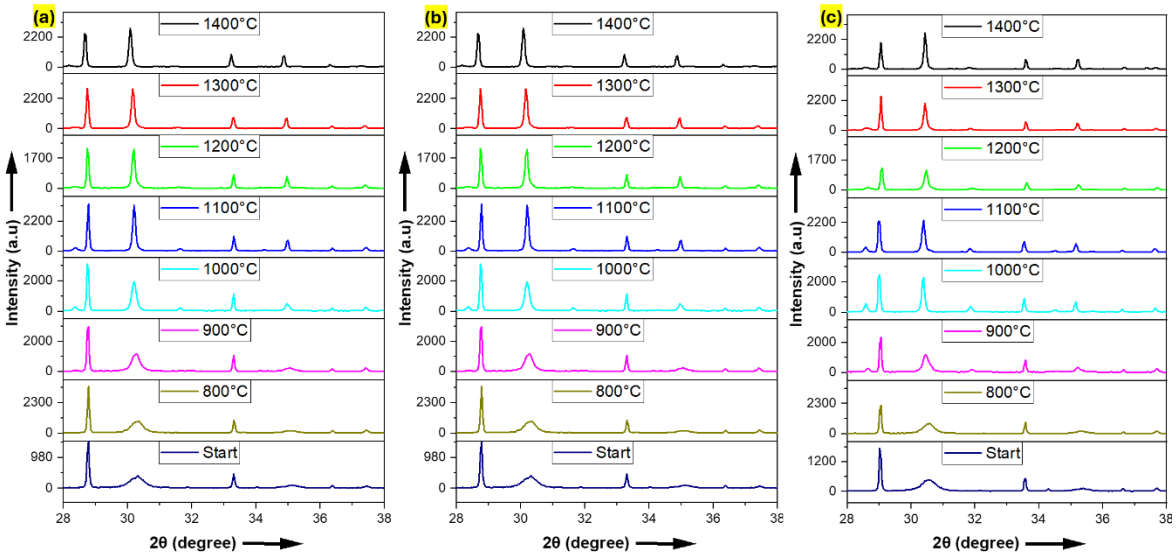

Figure 4.16. **(a)** XRD patterns for pellets 33.3 % 8YSZ + 33.3 % $La_2Zr_2O_7$ +33.3 % NiO annealed at 800°C,900 °C, 1000 °C, 1100 °C, 1200 °C, 1300 °C, and 1400 °C for 168 h.**(b)** XRD patterns for pellets 40 % 8YSZ + 40 % $La_2Zr_2O_7$ +10% NiO + 10% Na_2SO_4 annealed at 800°C,900 °C, 1000 °C, 1100 °C, 1200 °C, 1300 °C, and 1400 °C for 168 h. **(c)** XRD patterns for pellets 40 % 8YSZ + 40 % $La_2Zr_2O_7$ + 10% NiO + 9% Na_2SO_4 +1% V_2O_5 annealed at 800 °C,900 °C, 1000 °C, 1100 °C, 1200 °C, 1300 °C, and 1400 °C for 168 h.

After several hours of long-term pure oxidation, it was concluded that eventually, any observed phase instabilities are likely attributable to the mutual dissolution or decomposition of one or both phases, with the coexisting phase acting as a catalyst in this process. Similar analyses conducted on composite systems of $Sm_2Zr_2O_7$+8YSZ, $Gd_2Zr_2O_7$+8YSZ, $Nd_2Zr_2O_7$+8YSZ- types [38] suggested the potential occurrence of such phenomena. In these cases, the decomposition of the pyrochlore $ln_2Zr_2O_7$ phase into the fluorite type was observed following exposure to high temperatures, specifically 1100 °C for long term pure oxidation and molten salt corrosion. In the analyzed case of the $La_2Zr_2O_7$ + 8YSZ TBC system, a reaction between the two phases was not detected, which confirmed the XRD data for 50% $La_2Zr_2O_7$ + 50% 8YSZ TBC system after 3600 h of exposure at 1100 °C (**Figure 4.18.**). The SEM and XRD analysis of this TBCs system under liquid molten deposits did not confirm the phenomena related to mutual interaction between both phases. These findings led to the evaluation for LZO+YSZ as a good candidate for TBCs applications in high-temperature environments where stability and resistance to phase instabilities are paramount.

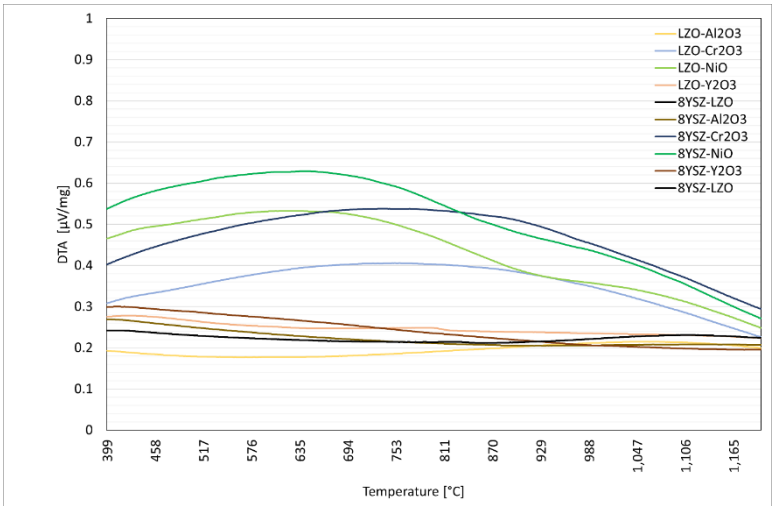

Figure 4.17. DTA tract of $La_2Zr_2O_7$ and 8YSZ compared with pure Al_2O_3, Cr_2O_3, NiO, Y_2O_3

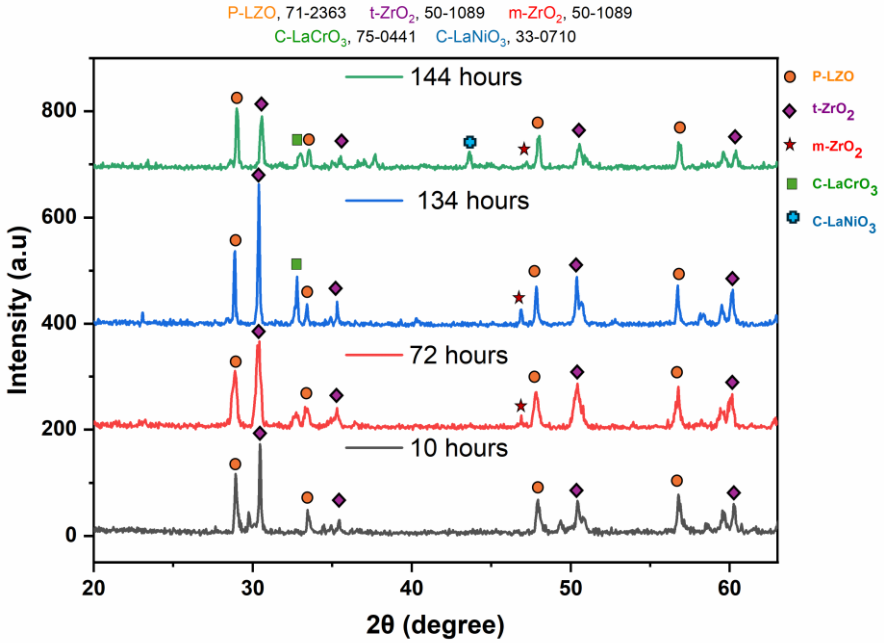

Figure 4.18. Phase composition of the ceramic topcoat of 50% $La_2Zr_2O_7$ + 50% 8YSZ TBC composite after oxidation test at 1100 °C with 360 h of exposure.

4.3. Summary

The investigations presented here have revealed primary symptoms of the interaction between liquid sodium sulfate salt and multi-phase TBC coatings comprising 8YSZ and $La_2Zr_2O_7$ ceramics: Surface displays on the topcoat, characterized by the emergence and proliferation of numerous small pits and textural roughness. Internal occurrences within the ceramic coating, evidenced by chemically reconstituted voids, diffusion of elements from TGO zone towards ceramic topcoat resulting in voids, microcracks, or interfacial changes.

Phenomena observed in the topcoat and substrate material region, associated with the formation of corrosion products. The module powders composition were synthesized for the confirmation of the observed phenomena interaction between TGO zone and dual phase composition. Furthermore, DTA and pure oxidation investigation support the stability of system. The XRD analysis of a TBC system with an composite layer showed stability of the pyrochlore phase at temperatures up to 1100 °C over 360 hours, at temperatures up to 920 °C to 970 °C over long term in molten sulphate and vanadium.

4.4. Conclusion

The APS-sprayed LZO + YSZ TBC system showed stability in different corrosive environments, while previous works on the instability of dual-phase systems such as SZO, and NZO, reported the formation of non-stoichiometric fluorite compounds through the decomposition of pyrochlore. In the LZO + YSZ system, no mutual interactions or transitional compounds were formed, even at high temperatures or in the presence of vanadium oxide. Furthermore, metallic elements such as Al, Cr, Mn, and Ni were added, which more significantly enhanced oxidation resistance, thermal stability, and mechanical properties of the coating, thus acting as a strong candidate for very high-temperature applications. Further stability was confirmed in the investigation of model powders corresponding to analyzed TBCs systems, where the obtained results are comparable. Analysis of phase transformation in 8YSZ, LZO and 8YSZ+LZO systems without and with the addition of Na_2SO_4 and V_2O_5 aggressive salts revealed only the partially thermal decomposition of tetragonal zirconia to its monoclinic lattice form. The presence of Na_2SO_4 and V_2O_5 compounds did not accelerate those reactions.

Another interesting piece of information observed during the analysis of powder systems under pure oxidation and hot corrosion conditions is related to the aggressive influence of oxides, such as NiO and Cr_2O_3, formed in the TGO zone. The formation of lanthanum chromites manifested that influence already at temperature ca. 800°C. This effect was slowed in assists of Na_2SO_4 and $Na_2SO_4 + V_2O_5$. In the case of NiO presence, only the accelerated decomposition of tetragonal zirconia to monoclinic form was detected. This fact

opens a new area of TBC systems investigations related to the harmful influence of the TGO scale on the phase stability of ceramic compounds forming the insulation layer.

Returning to the analysis of the results obtained for TBCs systems - the next investigation question arises regarding where the yttria went (why strong diffraction peaks covered by monoclinic zirconia were detected ?); the yttria was neither vaporized at high temperature (this effect was not detected under powders high-temperature annealing) nor consumed with any other element because XRD did not detect any interaction (both for TBC systems and mixed powders). Possibly, it may be secondary dissolved in the pyrochlore compound LZO with final formation of a more complex pyrochlore compound of LYZO type $(La,Y)_2Zr_2O_7$).

4.5. References:

1. Jesuraj, S. A., Kuppusami, P., Kirubaharan, A. K., & Rajasekaramoorthy, M. (2023). Advanced thermal barrier coatings for aerospace gas turbine engine applications. In *Advanced Ceramic Coatings for Emerging Applications* (pp. 151-183). Elsevier.
2. PANȚURU, M., Chicet, D., LUPESCU, Ș., Istrate, B., & Munteanu, C. (2018). Applications of ceramic coatings as TBCs on the internal combustion engine valves. *ACTA TECHNICA NAPOCENSIS-Series: APPLIED MATHEMATICS, MECHANICS, and ENGINEERING*, *61*(1).
3. Thompson, J. A., & Clyne, T. W. (2001). The effect of heat treatment on the stiffness of zirconia top coats in plasma-sprayed TBCs. *Acta materialia*, *49*(9), 1565-1575.
4. Ballard, J. D., Davenport, J., Lewis, C., Doremus, R. H., Schadler, L. S., & Nelson, W. (2003). Phase stability of thermal barrier coatings made from 8 wt.% yttria stabilized zirconia: A technical note. *Journal of Thermal Spray Technology*, *12*, 34-37.
5. Iqbal, A. (2023). An overview of the current status and emerging trends in thermally sprayed barrier coatings. In B. Balon (Ed.), *Interdyscyplinarne badania młodych naukowców* (No. 987; pp. 165–177).
6. Luo, X., Huang, S., Xu, C., Hou, S., & Jin, H. (2023). Rare-earth high-entropy aluminate-toughened-zirconate dual-phase composite ceramics for advanced thermal barrier coatings. *Ceramics International*, *49*(1), 766-772.
7. Iqbal, A., & Moskal, G. (2023). Recent Development in Advance Ceramic Materials and Understanding the Mechanisms of Thermal Barrier Coatings Degradation. *Archives of Computational Methods in Engineering*, 1-42.
8. Vassen, R., Cao, X., Tietz, F., Basu, D., & Stöver, D. (2000). Zirconates as new materials for thermal barrier coatings. *Journal of the American Ceramic Society*, *83*(8), 2023-2028.
9. Feng, J., Xiao, B., Zhou, R., Pan, W., & Clarke, D. R. (2012). Anisotropic elastic and thermal properties of the double perovskite slab–rock salt layer Ln2SrAl2O7 (Ln= La, Nd, Sm, Eu, Gd or Dy) natural superlattice structure. *Acta Materialia*, *60*(8), 3380-3392.
10. Dwivedi, G., Viswanathan, V., Sampath, S., Shyam, A., & Lara-Curzio, E. (2014). Fracture toughness of plasma-sprayed thermal barrier ceramics: influence of processing, microstructure, and thermal aging. *Journal of the American Ceramic Society*, *97*(9), 2736-2744.
11. Vaßen, R., Jarligo, M. O., Steinke, T., Mack, D. E., & Stöver, D. (2010). Overview on advanced thermal barrier coatings. *Surface and Coatings Technology*, *205*(4), 938-942.
12. Xu, Z., He, L., Mu, R., He, S., & Cao, X. (2010). Preparation and characterization of La2Zr2O7 coating with the addition of Y2O3 by EB-PVD. *Journal of Alloys and Compounds*, *492*(1-2), 701-705.
13. Gong, Y., Zhong, X., Ouyang, R., Xu, X., Fang, X., Xu, J., & Wang, X. (2023). Fabrication of Ln2Zr2O7 Fluorite and LnAlO3 Perovskite (Ln= La, Nd, Sm) Compounds to Catalyze the OCM Reaction: On the Temperature-Induced Phase Transformation and Oxygen Vacancy. *Inorganic Chemistry*, *62*(37), 15234-15248.
14. Naga, S. M., Awaad, M., El-Maghraby, H. F., Hassan, A. M., Elhoriny, M., Killinger, A., & Gadow, R. (2016). Effect of La2Zr2O7 coat on the hot corrosion of multi-layer thermal barrier coatings. *Materials & Design*, *102*, 1-7.
15. Yugeswaran, S., Kobayashi, A., & Ananthapadmanabhawn, P. V. (2012). Hot corrosion behaviors of gas tunnel type plasma sprayed La2Zr2O7 thermal barrier coatings. *Journal of the European Ceramic Society*, *32*(4), 823-834.
16. Jasik, A. (2019). Surface condition of la2zr2o7 based tbc system after hot corrosion in molten sulfate na2so4 salts. Ochrona Przed Korozją, 1(3), 18-21. https://doi.org/10.15199/40.2019.3.4
17. Jasik, A., Moskal, G., Mikuśkiewicz, M., Tomaszewska, A., Jucha, S., Migas, D., & Myalska, H. (2020). Oxidation behavior of the monolayered La2Zr2O7, Composite La2Zr2O7+ 8YSZ, and double-ceramic layered La2Zr2O7/La2Zr2O7+ 8YSZ/8YSZ thermal barrier coatings. *Materials*, *13*(14), 3242.
18. Shifler, D. A. (2017). The increasing complexity of hot corrosion. *Journal of Engineering for Gas Turbines and Power*.

19. Iqbal, A. (2023). An overview of the current status and emerging trends in thermally sprayed barrier coatings. In B. Balon (Ed.), *Interdyscyplinarne badania młodych naukowców* (No. 987; pp. 165–177).
20. Liu, Z. G., Ouyang, J. H., Zhou, Y., & Li, S. (2010). High-temperature hot corrosion behavior of gadolinium zirconate by vanadium pentoxide and sodium sulfate in air. *Journal of the European Ceramic Society*, *30*(12), 2707-2713.
21. Vaßen, R., Jarligo, M. O., Steinke, T., Mack, D. E., & Stöver, D. (2010). Overview on advanced thermal barrier coatings. *Surface and Coatings Technology*, *205*(4), 938-942.
22. Song, D., Song, T., Paik, U., Lyu, G., & Jung, Y. G. (2020). Hot corrosion behavior in thermal barrier coatings with heterogeneous splat boundary. *Corrosion Science*, *163*, 108225.
23. Mousavi, B., Farvizi, M., Rahimipour, M. R., & Pan, W. (2022). Comparison of the hot corrosion behavior of the LZ, CSZ and LZ/CSZ composite thermal barrier coating. *Surface and Coatings Technology*, *437*, 128324.
24. Parchovianský, M., Parchovianská, I., Hanzel, O., Netriová, Z., & Pakseresht, A. (2022). Phase Evaluation, Mechanical Properties and Thermal Behavior of Hot-Pressed LC-YSZ Composites for TBC Applications. *Materials*, *15*(8), 2839.
25. Ang, A. S. M., & Berndt, C. C. (2014). A review of testing methods for thermal spray coatings. *International Materials Reviews*, *59*(4), 179-223.
26. Tejero-Martin, D., Rezvani Rad, M., McDonald, A., & Hussain, T. (2019). Beyond traditional coatings: a review on thermal-sprayed functional and smart coatings. *Journal of Thermal Spray Technology*, *28*, 598-644.
27. Feuerstein, A., Knapp, J., Taylor, T., Ashary, A., Bolcavage, A., & Hitchman, N. (2008). Technical and economical aspects of current thermal barrier coating systems for gas turbine engines by thermal spray and EBPVD: a review. *Journal of Thermal Spray Technology*, *17*(2), 199-213.
28. Moskal, G., Jucha, S., Mikuśkiewicz, M., Migas, D., & Jasik, A. (2020). Atypical decomposition processes of Sm2Zr2O7+ 8YSZ dual-phase TBCs during hot corrosion. *Corrosion Science*, *170*, 108681.
29. Migas, D., Moskal, G., & Jucha, S. (2022). Hot corrosion behavior of double-phase Nd2Zr2O7-YSZ thermal barrier coatings. *Surface and Coatings Technology*, *449*, 128955.
30. Iqbal, A., Moskal, G., Głowacka, H. M., Pawlik, T., & Cavalerio, A. (2023). Phase decompositions of Gd2Zr2O7+ 8YSZ TBC systems under the condition of long-term high-temperature oxidation. *Surface and Coatings Technology*, *462*, 129471.
31. Di Girolamo, G. (2018). Current Challenges and Future Perspectives in the Field of Thermal Barrier Coatings. In *Production, Properties, and Applications of High Temperature Coatings* (pp. 25-59). IGI Global.
32. Evans, A. G., Mumm, D. R., Hutchinson, J. W., Meier, G. H., & Pettit, F. S. (2001). Mechanisms controlling the durability of thermal barrier coatings. *Progress in materials science*, *46*(5), 505-553.
33. Kumar, V., & Balasubramanian, K. (2016). Progress update on failure mechanisms of advanced thermal barrier coatings: A review. *Progress in Organic Coatings*, *90*, 54-82.
34. Zinkevich, M., & Aldinger, F. (2004). Thermodynamic analysis of the ternary La–Ni–O system. *Journal of alloys and compounds*, *375*(1-2), 147-161.
35. Yokokawa, H., Sakai, N., Kawada, T., & Dokiya, M. (1991). Chemical thermodynamic considerations in sintering of LaCrO3-based perovskites. *Journal of the Electrochemical Society*, *138*(4), 1018.
36. Yang, P., Bu, Z., An, Y., Zhou, H., Li, Y., & Chen, J. (2022). A systematic study on Na2SO4-induced hot corrosion behavior of plasma-sprayed La2 (Zr0. 75Ce0. 25) 2O7 coating. *Surface and Coatings Technology*, *429*, 127979.
37. Mousavi, B., Farvizi, M., Rahimipour, M. R., & Pan, W. (2022). Comparison of the hot corrosion behavior of the LZ, CSZ and LZ/CSZ composite thermal barrier coating. *Surface and Coatings Technology*, *437*, 128324.
38. Iqbal, A., Moskal, G., Cavaleiro, A., & Amjad, A. (2024). The current advancement of zirconate based dual phase system in thermal barrier coatings (TBCs): New modes of the failures: Understanding and investigations. *Alexandria Engineering Journal*, *91*, 161-196.

5. GADOLINIUM ZIRCONATE BASED TBCS

5.1. Introduction to GZO based TBCs

The driving force behind the development of new materials dedicated to modern gas turbines, including materials intended for thermal barrier coatings (TBCs), are primarily aspects related to increasing the efficiency of turbines, but also economic and environmental aspects [1]. TBC systems consist of a Ni-based superalloy substrate, a thermally sprayed interlayer (BC—MCrAlY) and an insulating ceramic outer coating (TC). The standard material for the outer ceramic layer is yttria-stabilized zirconium oxide, particularly 8YSZ (8 mass % $Y_2O_3 \times ZrO_2$). After the spraying process, 8YSZ is characterized by a metastable tetragonal *t′*-type structure with thermal stability up to a maximum temperature of 1300 °C, above which it undergoes a secondary transformation to a monoclinic structure. This primary to secondary transformation involves a volume change of 3 to 5%, which generates a high state of stress, and consequently, the falling off the ceramic layer, especially in conditions of long-term exposure at high temperature. Therefore, research in this area focuses on new materials with a thermal conductivity lower than 8YSZ, resistance to cyclic temperature changes, higher melting and higher phase stability under high-temperature conditions and in an aggressive working environment. The development of such a material would allow for a safe increase in the operating temperature of gas turbines [2-3]. From many new advanced ceramic materials, one of such materials are zirconates of rare earth elements with the general formula $A_2B_2O_7$, intensively researched for several years by the aviation industry. The group of these materials includes gadolinium zirconate $Gd_2Zr_2O_7$ (GZO), which can operate at temperatures exceeding 1200 °C without showing any tendency to undergo phase changes. Order to disorder transformation occurs in the temperature range 1530–1550 °C [4]. GZO is characterized by a thermal expansion coefficient of approximately $10.5 \times 10^{-6}\ K^{-1}$ (in the case of 8YSZ, it is approximately $11.7 \times 10^{-6}\ K^{-1}$), which negatively impacts the level of thermal stresses in the coating.

Moreover, GZO has a thermal conductivity of 1.1–1.7 $Wm^{-1}K^{-1}$, much lower than in the case of 8YSZ (approx. 2.1 $Wm^{-1}K^{-1}$) at a temperature of 1000 °C [5]. Literature analysis shows that single-layer GZO TBC systems are characterized by significant limitations related to the high tendency to crack and collapse of this type of ceramic layer. Additionally, at high temperatures, the GZO TBC coating was characterized by visible interaction effects between GZO and Al_2O_3 in the TGO zone, creating a porous $GdAlO_3$ perovskite layer [6-7].

An essential advantage of pyrochlores, including GZO, is the resistance of this type of compound to hot corrosion phenomena, including in the presence of highly aggressive vanadium oxide. Jonnalagadd et al. [8] analyzed GZO-YSZ composite coatings and examined their corrosion behavior. They hypothesized that GZOs effectively prevent the diffusion of molten salts (mitigation effect), which causes salts to accumulate at the edges of the coating and causes severe corrosion, but only in this area. Ozgurluk et al. [9] investigated TBCs systems obtained by EB-PVD (YSZ, GZO and YSZ/GZO). Significant progress in corrosion degradation was found under exposure to a mixture of 55% V_2O_5 and 45% Na_2SO_4 salts at a temperature of 1000 °C. As stated in the study, the increased V_2O_5 content accelerates corrosion by generating the transformation of the tetragonal YSZ phase to the monoclinic form with the simultaneous formation of the YVO_4 phase (Y_2O_3 consumption). At the same time, GZO coatings and YSZ/GZO coatings showed mono-clinic zirconium oxide and $GdVO_4$ structures. Despite lower crack resistance than 8YSZ TBCs systems, leading to early cracking, GZO coatings seem promising for TBCs operating in high-temperature corrosion conditions.

GZO's phase stability characteristics in hot corrosion conditions suggest an increasing thermal and chemical stability. According to Liu et al. [10], V_2O_5 in the presence of Na_2SO_4 accelerates the GZO corrosion process and causes a phase transformation within two hours of exposure at 700 °C. However, at 900 °C and 1000 °C for two hours, no reaction was observed in the presence of pure Na_2SO_4. The study in [11] aimed to increase the corrosion resistance of the TBCs system by introducing nanostructured GZO. The nanostructure improved hot corrosion resistance due to its denser and more compact coating structure. Due to Gd_2O_3's higher acidity compared to Y_2O_3, the reaction driving force for $Gd_2O_3 + NaVO_3$ was lower than for $Y_2O_3 + NaVO_3$, which confirmed that GZO showed better hot corrosion resistance compared to YSZ.

One study [12] assessed the corrosion resistance of suspension plasma sprayed TBCs, particularly multilayer GZO/YSZ and single-layer YSZ coatings, exposed to a corrosive environment at 900 °C. GZO-based coatings showed reduced reactivity with aggressive salts. Nevertheless, their columnar microstructure facilitated their penetration, generating numerous corrosion products and extensive cracks. A dense layer of GZO on top did not improve corrosion resistance; the damage was concentrated in the lower part of the layer due to the infiltration of aggressive salts. However, the reference YSZ coating showed better corrosion resistance due to limited salt penetration, specific microstructure and higher crack resistance. Vassen et al. [13] analyzed single-layer TBCs systems of the YSZ-type and double-layer GZO/YSZ systems at extremely high temperatures, up to 1550 °C. The results showed that the dense GZO/YSZ coatings showed poor resistance, while the porous films performed better. The porous and dense YSZ coatings also performed well, although they had a slightly shorter service life than the porous GZO/YSZ systems.

In the existing research, the hot corrosion resistance of composite two-phase TBC coatings of the YSZ/GZO type in the environment of pure sodium sulphates was investigated [14]. Previous research on the pure oxidation [15] focused on examining the behavior of the two-phase YSZ/GZO composite system during long-term isothermal oxidation at a temperature of 1100 °C for 2000h is one the novel and first reported data. The main goal of hot corrosion-pure oxidation work was to explain the degradation mechanism of this type of coating. The origin of this phenomenon was attributed to the complex interaction of both phases, indicating the processes of decomposition of the pyrochlore phase to form fluorite with different stoichiometry and enrichment of the 8YSZ phase by dissolving gadolinium oxide.

This study, motivated by the observations obtained that dual phase system has low thermal conductivity, but there are other degradation routes that occur in the dual phase system, has yet to be investigated to better understand the credibility of multi-phase TBCs. It is worth noting that a low amount of data regarding the hot corrosion phenomena of composite coatings of this type is available in the literature under the influence of pure sulphate salts [16-17].

5.2. Results and discussion.

5.2.1. Characterization of feedstock powders

Figures 5.1. to 5.3. illustrate SEM images showing the morphology, i.e. size, shape, surface condition and chemical composition of powders used in the APS spraying process of TBCs

type 8YSZ/GZO systems, as well as their phase composition and granule size distribution. The morphology of YSZ and GZO powder materials is spherical with voids and has various size distributions, which shows good technological properties such as flowability. The morphology of 8YSZ is typical for the plasma remelting process and GZO for spray drying technology (**Figure 5.1. a-d**). Phase composition analysis used powder X-ray diffraction patterns, as depicted in **Figure 5.2.** The diffraction pattern for gadolinium zirconate indicated the presence of a cubic $Gd_2Zr_2O_7$ phase with a fluorite lattice structure, consistent with ICDD card number 80–0471. In contrast, the analysis of 8YSZ revealed a tetragonal phase of zirconium oxide ZrO_2. The predominant phase exhibited a tetragonal lattice structure, as confirmed by ICDD card number 50–1089. In EBSD studies, **Figure 5.3.** a revealed a tetragonal phase for YSZ powder. The space group number is 137. In Hermann–Mauguin notation, this space group is I41/amd, also known as 4/mmm. This space group denotes crystal with a fourfold rotation axis and additional mirror planes. The MAD value is given as 0.264°. **Figure 5.3.** b illustrates the cubic phase of GZO. The space group number is 225. In Hermann–Mauguin notation, this space group is denoted as Fm 3 m (or m3m for short). This space group indicates a crystal with cubic symmetry and a surface-centred cubic (FCC) structure of the fluorite type. The MAD value is given as 0.446°. The granule or particle size distribution is another important aspect of the powders used in depositing APS- based coatings which can be seen in **Figure 5.4.**

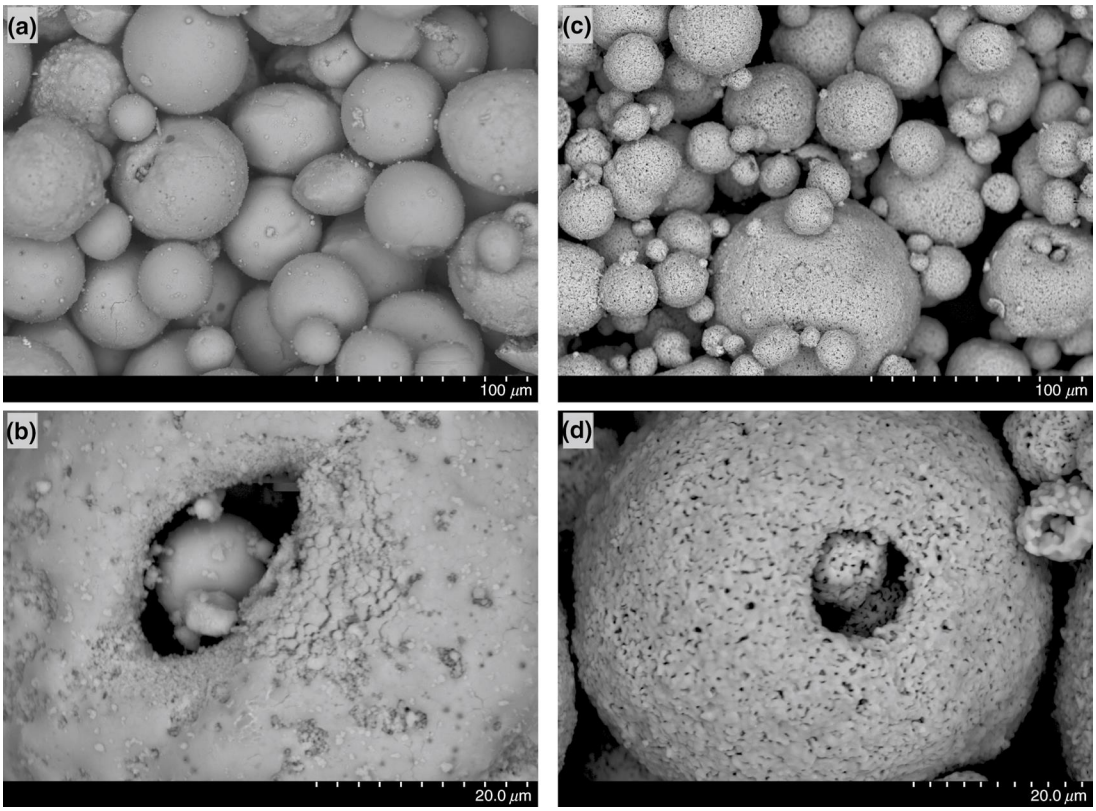

Figure 5.1. SEM micrographs of YSZ and GZO powders: **a**,**b** top-surface images of YSZ and GZO powders, **c**,**d** cross-sectional views of YSZ and GZO powders

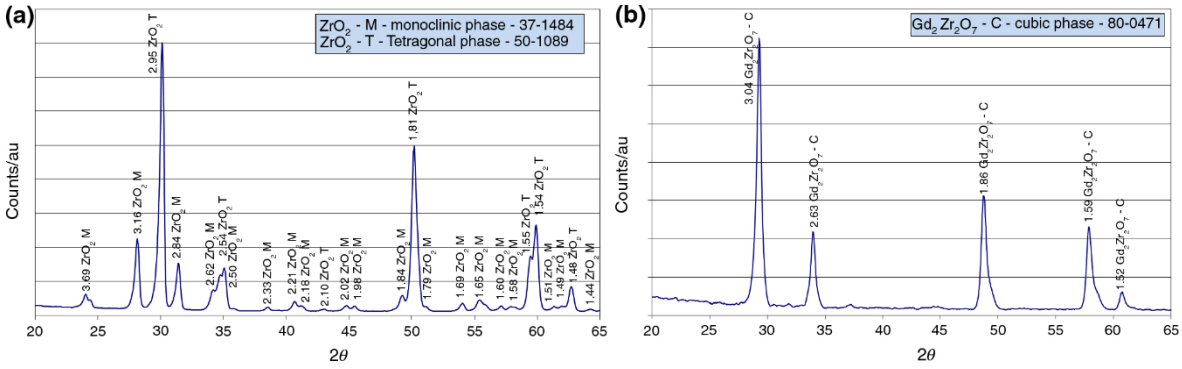

Figure 5.2. X-ray diffraction patterns of **a** yttria-stabilized zirconia and **b** gadolinium zirconates feedstock powders used in the APS process

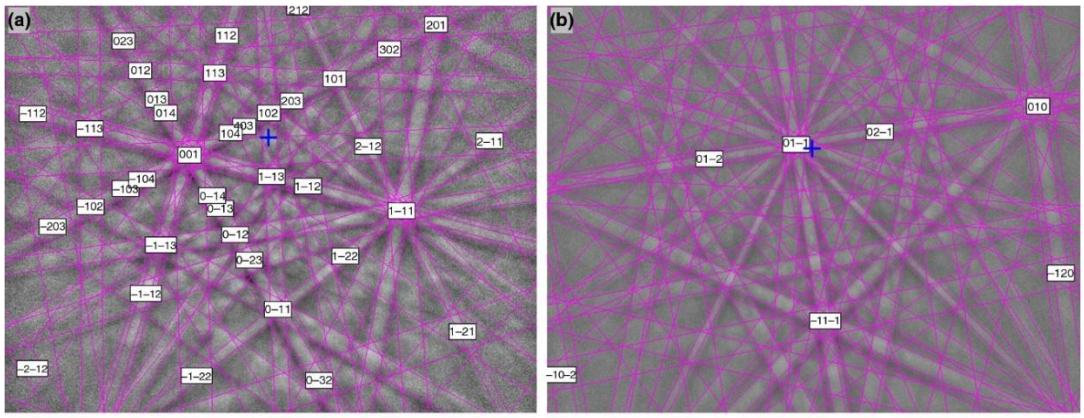

Figure 5.3. The EBSD patterns of **a** yttria-stabilized zirconia, **b** gadolinium zirconates, and their crystallographic details

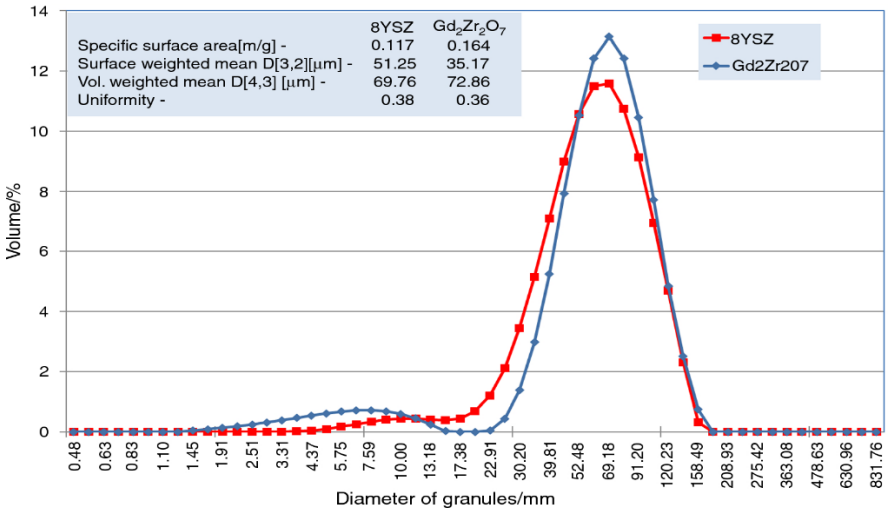

Figure 5.4. The granule size distribution of sprayed feedstock powders

5.2.2. Characterization of coatings samples

Figure 5.5. to 5.6. shows visual examinations of the surfaces of TBC systems analyzed after thermal spraying. The coatings' condition is typical for this process. No effects were found that could accelerate the destruction processes in hot corrosion conditions. No delamination or microcracks were found, only microcracks typical of the APS process. The results of metallographic tests on the cross section are presented in **Figure 5.5.**

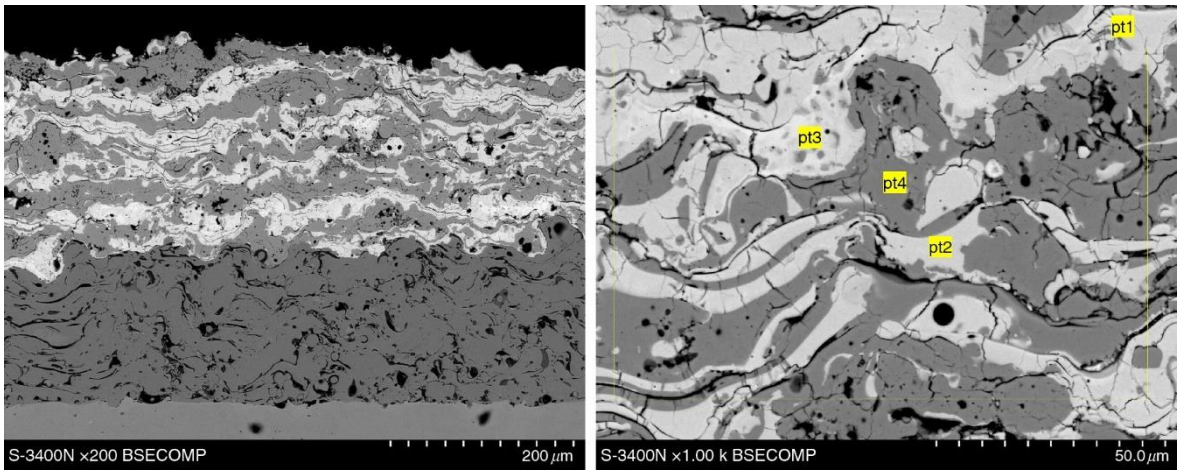

Figure 5.5. Cross-section analysis of 8YSZ/GZO dual-phase TBCs with chemical composition analysis in characteristic micro-areas

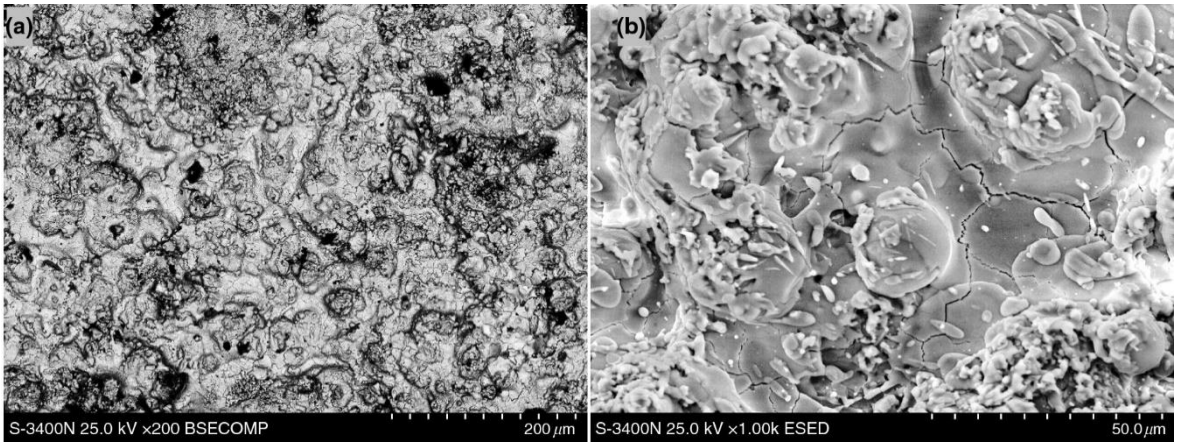

Figure 5.6. Top surface morphology of 8YSZ/GZO dual-phase as-sprayed coatings

5.2.3. Degradation mechanism in GZO+YSZ systems

The final stage of the research was the analysis of the degradation mechanisms of the 8YSZ/GZO two- phase TBC coatings. From the point of view of visual assessment, the main effect related to the progress of corrosion processes is a change in the colour of the coatings from white to various shades of brown yellow. Additionally, small cracks also appeared in the edge areas. These observations were based on the sample presented in **Figure 5.7.** It should be noted that the intensity of destruction is much more significant in the case of higher exposure temperature in liquid Na_2SO_4 salt deposits, i.e. at 970 °C. Microscopic analysis of the surface of the insulating layer tested at a temperature of 920 °C (**Figure 5.8.**) showed the presence of dominant areas whose chemical composition would correspond to either the 8YSZ or GZO compound. The presence of regions corresponding to Ni–Al–O type oxides was also found; most likely, they are spinel compounds of the $NiAl_2O_4$ type.

The presence of areas rich in Sulphur and sodium (Na_2SO_4) with simultaneous enrichment in chromium is also clearly visible, consistent with the observations presented in the work [18]. It indicated the mechanism described by Rapp [19] as the cause of the observed destruction processes in two-phase TBC coatings. A similar effect was also observed in the case of corrosion resistance tests at a temperature of 970 °C (**Figure 5.9.**). Diffraction studies of the phase composition **Figure 5.10**., performed on the surface of the tested samples, showed relatively small differences in both temperature variants of hot corrosion resistance tests in the environment of liquid Na_2SO_4 salt deposits. The main symptom of degradation processes in two-phase 8YSZ/GZO systems is the formation of non-stoichiometric zirconate phases, which is manifested by the shift of diffraction peaks towards larger values of the 2-theta angle. In an extreme case, creating a cubic ZrO_2 phase with a very high Gd_2O_3 content would be possible. At the same time, with the formation of intermediate Gd–Zr–O phases, the ZrO_2 phase disappears, which indicates its dissolution in the pyrochlore matrix and a relative decrease in the Gd_2O_3 concentration in the parent phase. There are no broader reports on this specific phenomenon of decomposition of pyrochlore phases in TBCs systems. However, some literature emphasizes that phase transformations and interactions between the components of TBCs systems are important factors contributing to the degradation of coatings [20].

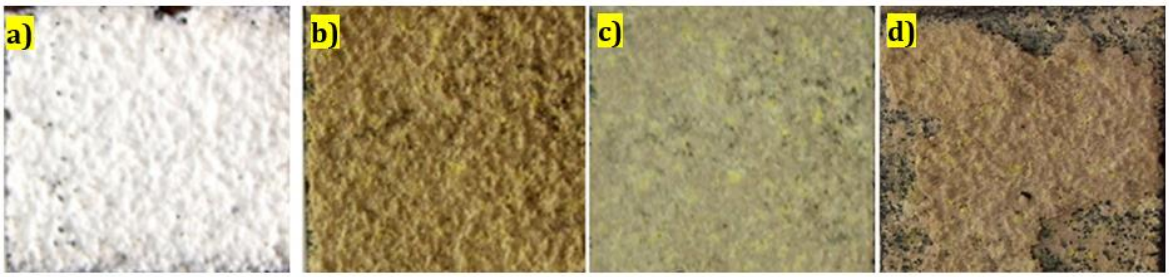

Figure 5.7. Visualization of the examined top surfaces of 8YSZ/GZO TBC systems in the as-sprayed condition and after hot corrosion testing in a pure sodium sulphate (Na_2SO_4) environment at temperatures of 920 °C for 124 (b), 240 h (c) and 970 °C for 124 h (d)

Dudnik et al. [21] emphasized the importance of the YSZ-type intermediate layer due to the relationships resulting from the ZrO_2–Gd_2O_3–Al_2O_3 system. A significant concern raised in the text is the possibility of solid-phase interactions between Gd2Zr2O7 and Al_2O_3, i.e. the chemical reaction described as $Gd_2Zr_2O_7 + Al_2O_3 \leftrightharpoons ZrO_2 + GdAlO_3$.

Understanding these mechanisms is critical to designing TBC coatings with longer service life and developing strategies to mitigate their effects in aggressive operating environments in practical applications. The addition of a YSZ interlayer can prevent these interactions in the solid phase. In our previous studies on the decomposition of samarium zirconate (SZO) in the system with 8YSZ [18], it was found that under the conditions of analogous tests at 920 °C and 970 °C, the composition of 8YSZ/SZO coatings (50/50% by mass) changed dramatically. It consisted of changing the initial state from the pyrochlore form of $Sm_2Zr_2O_7$ to various forms of fluorite lattice. At the same time, a gradual disappearance of 8YSZ was observed. Compared to the current 8YSZ/GZO system research, the observed changes occurred slower than in the analyzed case. This 8YSZ/GZO composition showed strong susceptibility to mutual interaction activated by temperature and aggressive environments. This decomposition resulted in various corrosion products, mainly gadolinium zirconates of the fluorite type. These final compounds (after testing at 970 °C), designated as $Gd_{0.30}Zr_{0.63}O_{1.82}$, $Gd_{0.37}Zr_{0.63}O_{1.82}$ and $Gd_{0.46}Zr_{0.54}O_{1.77}$ (Respectively designated as 4, 5 and 6 in **Figure 5.10.**), show the culmination of complex chemical interactions and transformations inside the 8YSZ/GZO TBC system. It is also worth considering that pyrochlore compounds (zirconates of rare earth elements) show strong phase stability even at high temperatures [22]. This refers to the $GdO_{1.5}$—ZrO_2 binary phase diagram **Figure 5.11.**, which illustrates the formation of the pyrochlore GZO phase from the fluorite phase. Interestingly, for some pyrochlores with larger rare earth cation radii, the pyrochlore phase forms directly from the liquid phase. Notably, the stability of the pyrochlore phase in GZO, as shown in the phase diagram, reaches approximately 1550 °C, thus exceeding typical engine surface temperatures. Moreover, it was found that the transformation from pyrochlores to fluorite compounds in GZO has no adverse effect on the integrity of the TBCs because the cubic phase is retained. A similar interaction of components was also observed in the case of high-temperature oxidation of TBC coatings type 8YSZ/GZO [15]. However, a stable GZO to YSZ concentration ratio was observed in this case, with the simultaneous formation of various fluorite-type gadolinium zirconate compounds. This suggests a different mechanism for forming the fluorite compound related to the simultaneous dissolution of Gd_2O_3 in 8YSZ and $ZrO_2(Y_2O_3)$ in GZO (Table in **Figure 5.8.**).

Assuming, in pure oxidation conditions, the observed phenomenon of pyrochlore compounds decomposition has a typical thermally activated diffusional feature. Still, in the case of the hot corrosion process in the Na_2SO_4 environment, the observed diffusional

process is significantly accelerated. This acceleration can be attributed to a phenomenon known as the fluxing mechanism, previously described by Rapp [19] and slightly modified (for the needs of zirconate compounds) based on the analysis of $Sm_2Zr_2O_7$ + 8YSZ systems [18]. In this mechanism, the corrosion process involves the interaction of liquid Na_2SO_4 salt deposits with a ceramic mixture of $Gd_2Zr_2O_7$ and 8YSZ. Corrosion occurs through both acidic and alkaline dissolution of oxides. Notably, corrosion is observed when thin layers of dissolved salts are present. These thin layers facilitate the transport of oxidizing gases and ions, which are consistent with the results of our study. Na_2SO_4 decomposition products play a key role in the dissolution of oxides under the influence of specific chemical reactions presented in Equation 1-4. Thermodynamic calculations confirm the reality of such a process. The reaction described in equation (4) offers a potential explanation for the lack of phase diffraction peaks present in the products of earlier reactions (1-3). Additionally, it is responsible for the formation of defective fluorite phases. The reprecipitation of Na_2SO_4 and Gd_2O_3 plays a key role in the self-sustaining reaction known as "synergistic hot corrosion" and "synergistic degradation".

(1) $Na_2SO_4 \rightarrow Na_2O(l)+SO_3(g)$

The reaction's calculated enthalpy change (ΔH) is -786.2 kJ/mol.

(2) $Na_2O(l)+Gd_2O_3 \rightarrow 2NaGdO_2$ Basic reaction

The reaction's calculated enthalpy change (ΔH) is -1220.8 kJ/mol.

(3) $ZrO_2+2SO_3(g) \rightarrow Zr(SO_4)_2$ Acidic reaction

The reaction's calculated enthalpy change (ΔH) is -1224.9 kJ/mol.

Then, salts can re-precipitate if they react with one another, as shown in Equation 4

(4) $8NaGdO_2+2Zr(SO_4)_2 \rightarrow Gd_2Zr_2O_7+4Na_2SO_4+3Gd_2O_3$

The reaction's calculated enthalpy change (ΔH) is -6116.6 kJ/mol.

The evaporation process can also enhance the effect of decreasing the Gd_2O_3 concentration, which is typical for rare earth oxides [22]. These three pathways may form new non-stoichiometric compounds resulting from decomposition (Eq. 1–3 or evaporation of Gd_2O_3) and reprecipitation (Eq. 4).

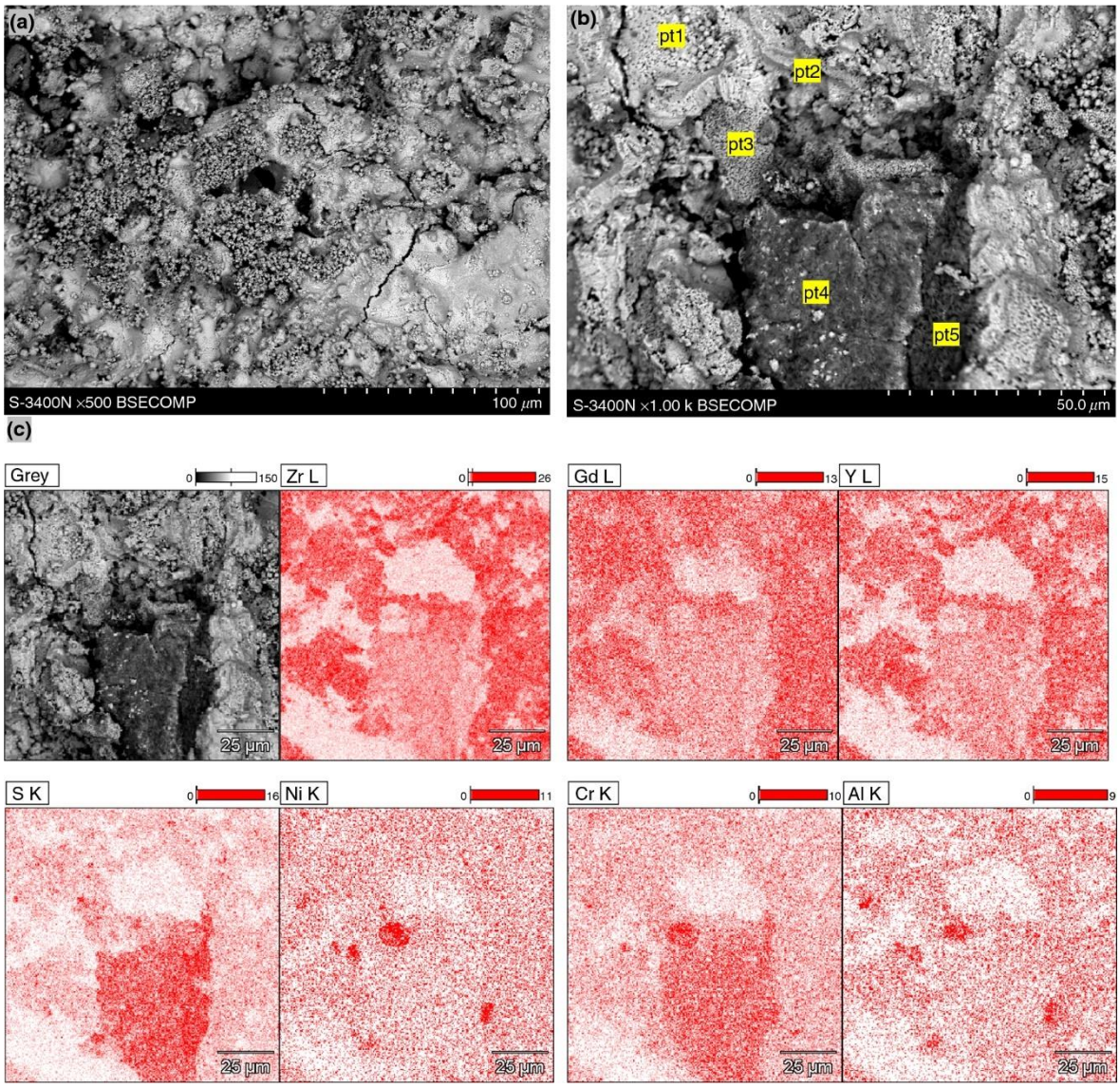

Weight %	*O-K*	*Na-K*	*S-K*	*Cr-K*	*Ni-K*	*Y-L*	*Zr-L*	*Gd-L*
pt1	18.5			1.1		1.4	30.9	48.0
pt2	21.0	0.5	1.7	2.0		1.9	33.9	39.0
pt3	18.2				2.0	1.8	29.3	48.6
pt4	23.4	1.0	5.9	10.2		1.2	24.9	33.4
pt5	25.6	1.3	8.4	10.9	1.3	1.4	22.1	29.2
Atomic %	*O-K*	*Na-K*	*S-K*	*Cr-K*	*Ni-K*	*Y-L*	*Zr-L*	*Gd-L*
pt1	63.0			1.2		0.8	18.4	16.6
pt2	63.6	1.0	2.6	1.9		1.1	17.9	12.0
pt3	62.4				1.9	1.1	17.6	16.9
pt4	61.3	1.8	7.8	8.2		0.6	11.4	8.9
pt5	61.7	2.2	10.1	8.1	0.9	0.6	9.3	7.2

Figure 5.8. Top surface morphology and chemical composition in characteristic micro-areas of 8YSZ/GZO TBC systems after hot corrosion at 920 °C for 240 h

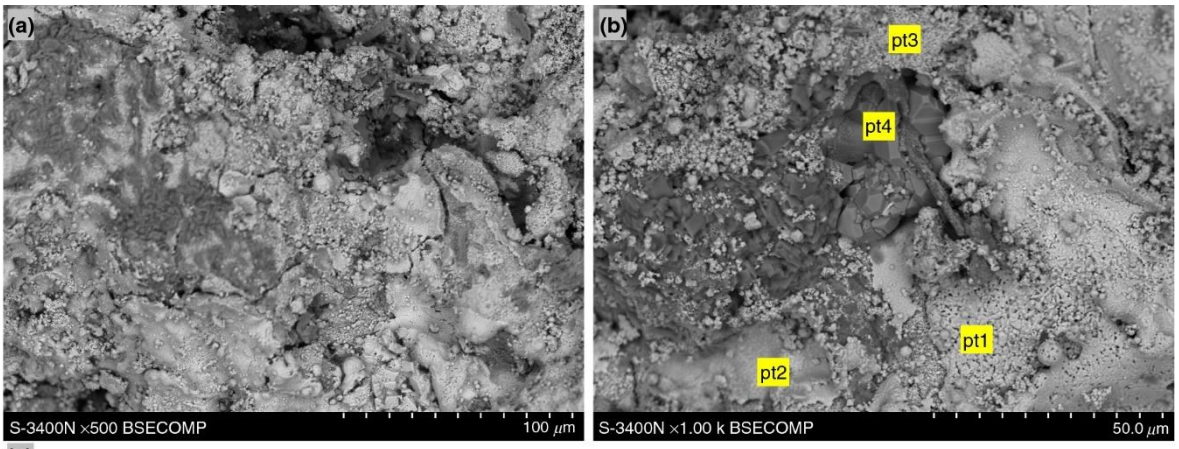

(c)

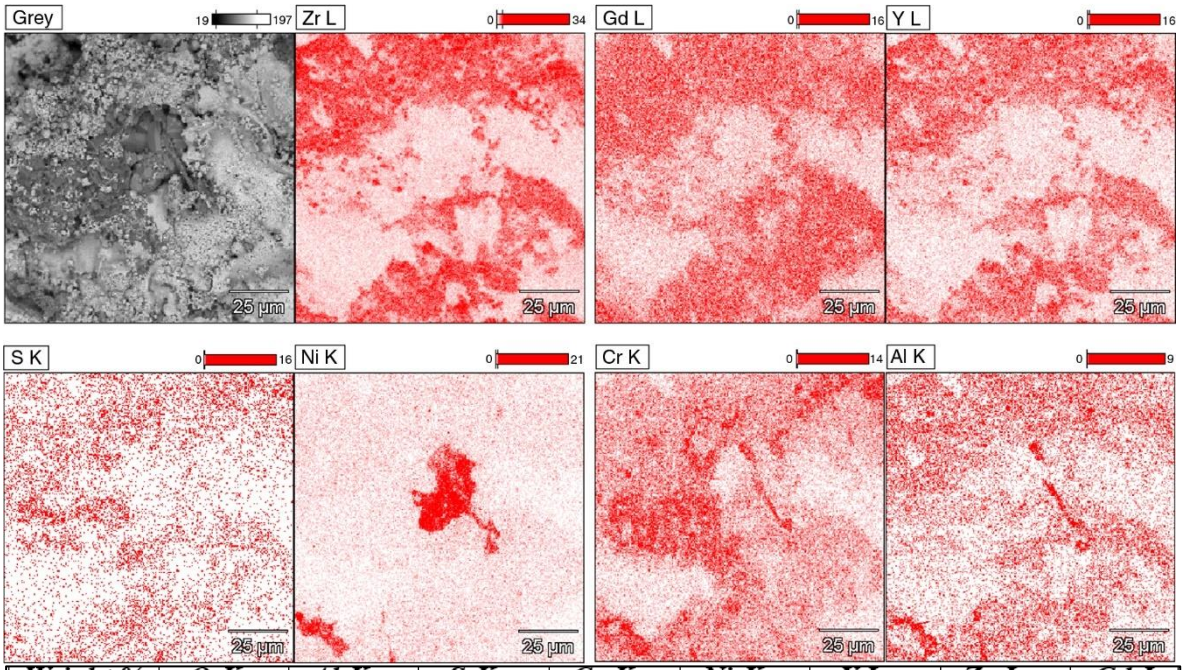

Weight %	*O-K*	*Al-K*	*S-K*	*Cr-K*	*Ni-K*	*Y-L*	*Zr-L*	*Gd-L*
pt1	18.1	0.1			1.5	1.2	26.3	52.7
pt2	19.2			2.7	4.3	1.1	27.5	45.3
pt3	19.6			1.9	1.9	1.7	31.7	43.2
pt4	21.4	0.3	0.1	3.4	53.1	0.3	7.8	13.6
Atomic %	*O-K*	*Al-K*	*S-K*	*Cr-K*	*Ni-K*	*Y-L*	*Zr-L*	*Gd-L*
pt1	62.9	0.2			1.4	0.8	16.1	18.6
pt2	62.4			2.7	3.8	0.6	15.6	14.9
pt3	63.3			1.9	1.7	1.0	18.0	14.2
pt4	53.5	0.5	0.1	2.6	36.3	0.1	3.4	3.5

Figure 5.9. Top surface morphology and chemical composition in characteristic micro-areas of 8YSZ/GZO TBC systems after hot corrosion at 970 °C for 124 h

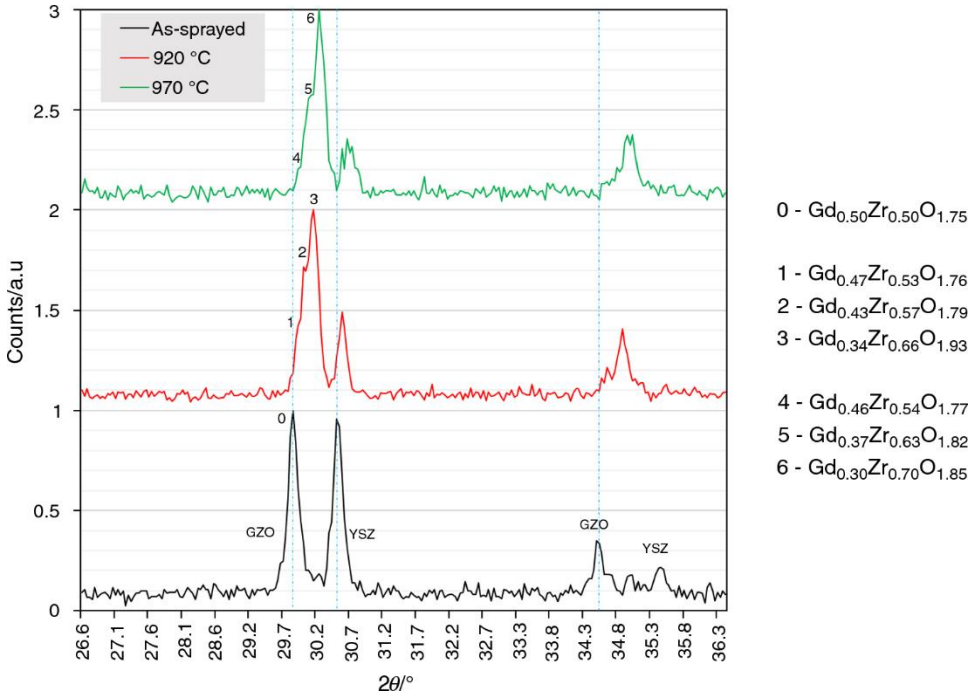

Figure 5.10. Phase constituent of 8YSZ/GZO TBC systems after hot corrosion tests

To further explain the decomposition phenomena in the 8YSZ/GZO TBC system, tests were performed on model systems based on an equimolar system of the same powders. The results of high-temperature annealing in the temperature range of 800–1400 °C in the form of changes in phase components described by XRD analysis are shown in **Figure 5.12**. Surprisingly, although the final result is the same (changes in phase components with the formation of non-stoichiometric zirconate compounds), the decomposition mechanism seems to be different than in the 8YSZ/GZO TBC systems manufactured using the APS method. In the case of sintered powders, contrary to the case of APS TBC, a decrease in the intensity of the GZO peaks is detected while shifting them to a higher value of the 2-theta angle—reducing the d value. The opposite situation is observed in the case of the main YSZ peak, which has a stable intensity but also shifts to the left (lower value of two theta). At the end of the process, the coexistence of Gd_2O_3-rich tetragonal ZrO_2 compounds and Gd_2O_3-depleted fluorite compounds Gd–Zr–O (or zirconium oxide—GdYSZ). It should be possible to obtain uniform single-phase materials if sufficient annealing temperature and/or time is used. These phenomena correspond to the data presented in [15], where the mutual dissolution of YSZ and various zirconates was observed during high temperature annealing in air (**Table in Figure 5.9.**).

An additional element presented in the analysis of powder systems research is the description of the influence of sodium sulphate on accelerating decomposition at

temperatures higher than 800 °C. The addition of sulphate salt strongly reduces the intensity of GZO diffraction peaks, which suggests a stronger tendency towards decomposition reactions and the formation of fluorite phases. However, the mechanism of this process cannot be explained by Eqs. 1—4, because the ratio of GZO to YSZ intensity is different than in the case of the APS TBC system. As suggested in [23-24], in the case of sintered materials, the inter-grains boundary's wetting effect is significant, allowing for the easy implementation of the intergranular diffusion process (a stronger diffusional mechanism). The splat-to-splat interface is much more complex with APS TBC systems, with pores and cracks between the splats. It can significantly slow down thermally activated diffusion processes, facilitating the penetration of liquid sulphide salts through pores and cracks (stronger Rapp mechanism). A similar effect (influence of grain boundary morphology) was observed in work [25], where different decomposition effects were observed in $La_2Zr_2O_7 + 8YSZ$ TBC systems depending on the form of powders used for thermal spraying—properly ground and mixed.

The analysis of the DTA results **Figure 5.13**, performed on the equimolar mixture of the feedstock 8YSZ and GZO powders with and without the addition of sulphate sale, does not include the thermal effects indicated for the course related to phase transformations. The slight thermal effect is achieved by melting sulphate salt. These results suggest that powder analysis's dominant mechanism of degradation phenomena is related to diffusional processes.

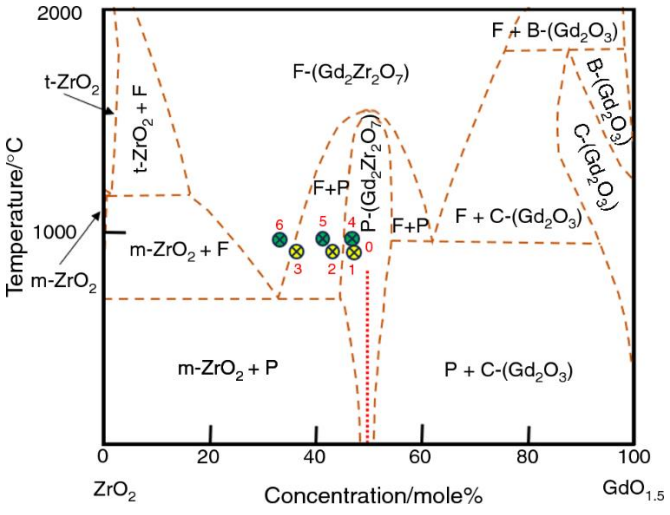

Figure 5.11. Fluorite new-formed compounds localization in ZrO -GdO

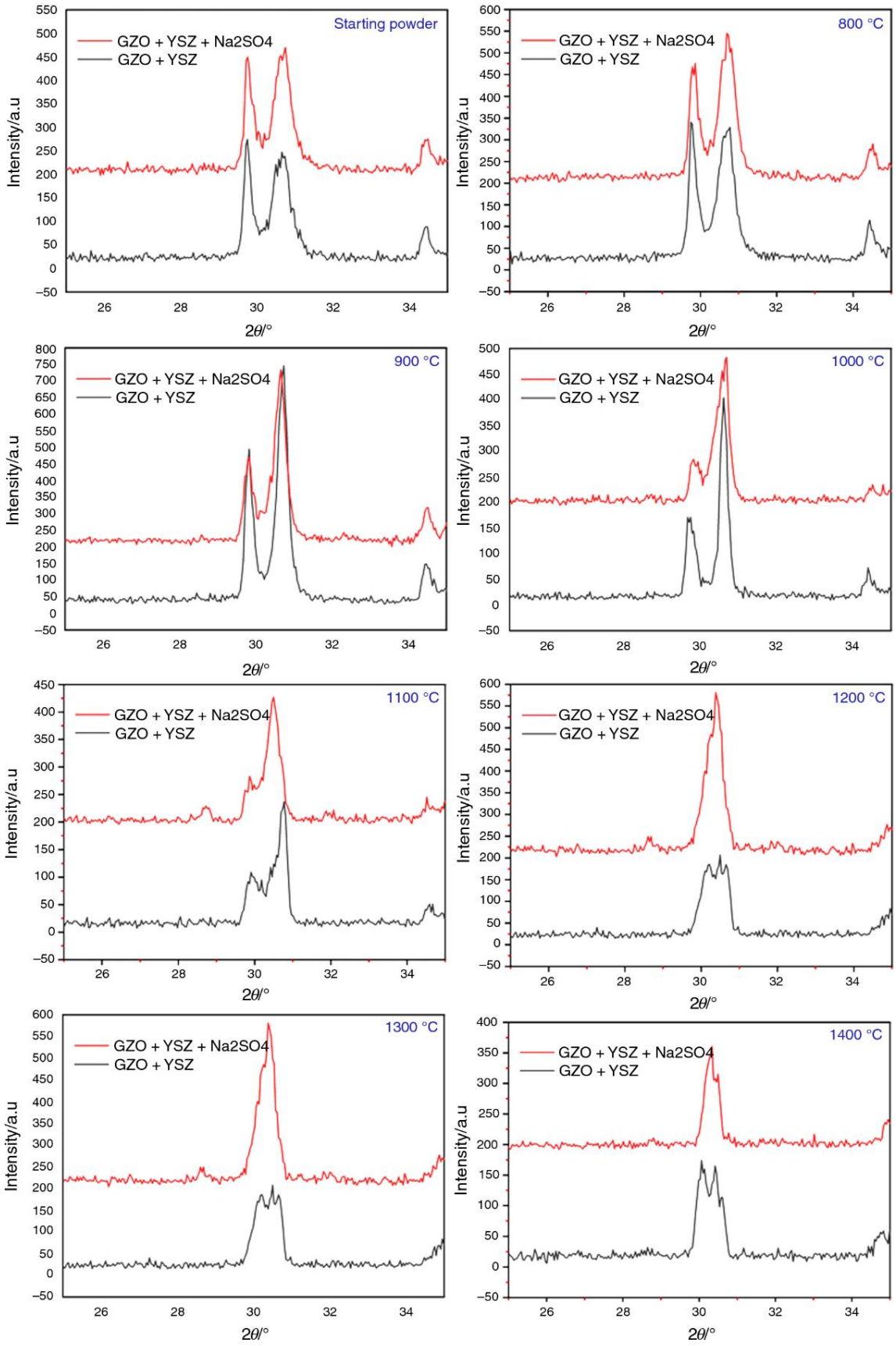

Figure 5.12. XRD analysis of powder-based GZO + 8YSZ and GZO + 8YSZ + Na_2SO_4 systems under high-temperature annealing at temperature range 800–1400 °C

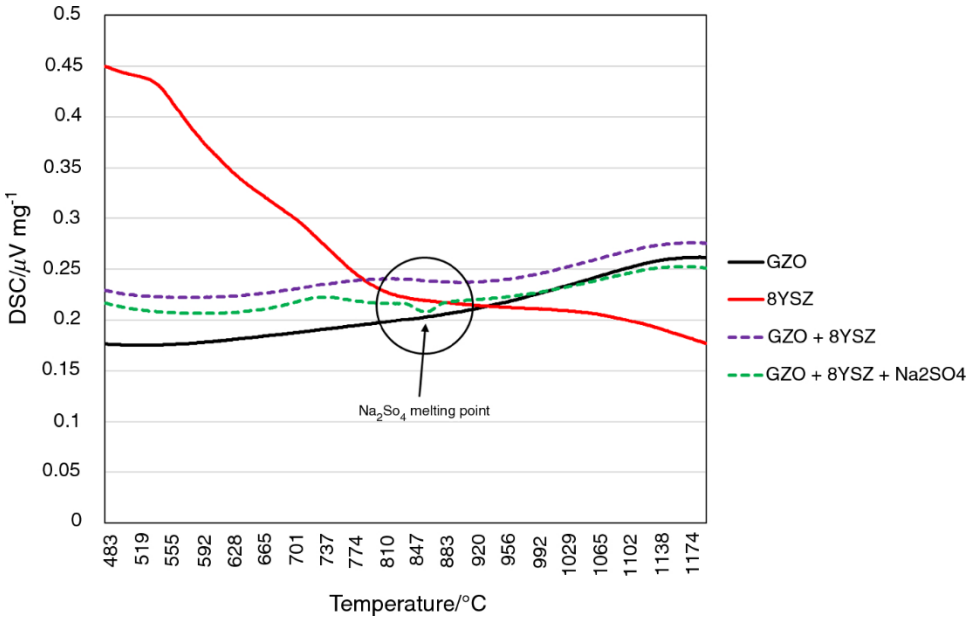

Figure 5.13. DTA characterization of mutual interactions between 8YSZ and GZO powders and Na_2SO_4 salt at temperature range 25–1200 °C

The further experiment on GZO+YSZ for pure oxidation test were performed on three composition 25/75, 50/50 and 75/25 (YSZ-GZO). The results of the tests characterizing the changes in phase composition in 8YSZ + GZO TBC systems under oxidation conditions at 1100 °C in the time range of 2 to 2000 h are shown in **Figure 5.14., Figure 5.15., Figure 5.16**. These figures show a fragment of X-ray diffraction covering the strongest 8YSZ phase reflections (tetragonal and monoclinic) and zirconate phases. The analysis of the results presented in **Figure 5.14**. clearly shows that with the lapse in the annealing time at temperature 1100 °C, appear from a different type of structural elements from the $Gd_2Zr_2O_7$ phases and the tetragonal ZrO_2 oxide. These are gadolinium zirconates with a lower amount of gadolinium oxide and the tetragonal or cubic phase of ZrO_2 enriched with the released gadolinium oxide. Analyzing the state immediately after thermal spraying, the diffraction tests showed the presence of peaks of diffraction at the angle of $2\Theta = 29.280$ and a value of $d = 3.046$, which corresponds to the $Gd_2Zr_2O_7$ phase with a fluorite network according to the ICDD 04–086-5075 card number; and the reflex at an angle of $2\Theta = 30.399$ and the value of $d = 2.937$, which corresponds to the tetragonal phase of ZrO_2 according to the ICDD card number 50–1089. After 2000 h of exposure at a temperature of 1100 °C, the analogous diffraction reflections take the values of the angles $2\Theta = 29.458$ and $d = 3.028$ as well as $2\Theta = 30.113$ and $d = 2.964$, respectively. These displacements indicate the depletion

of gadolinium zirconate into gadolinium oxide and the secondary enrichment of tetragonal zirconium with the same gadolinium oxide (in addition to the already present yttrium oxide). In this case, the presence of a zirconate phase of type $Gd_{0.4}Zr_{0.6}O_{1.80}$ (ICDD - 04-020-5942) or a zirconate with a higher content of gadolinium oxide (not described in ICDD database) and the tetragonal phase of type $Gd_{0.06}Zr_{0.94}O_{1.97}$ (ICDD 04-024-8446) type is possible. Furthermore, additional weaker diffraction reflections were identified at angle values 2Θ = 29.787 and d = 2.996 as well as 2Θ = 29.962 and d = 2.979.

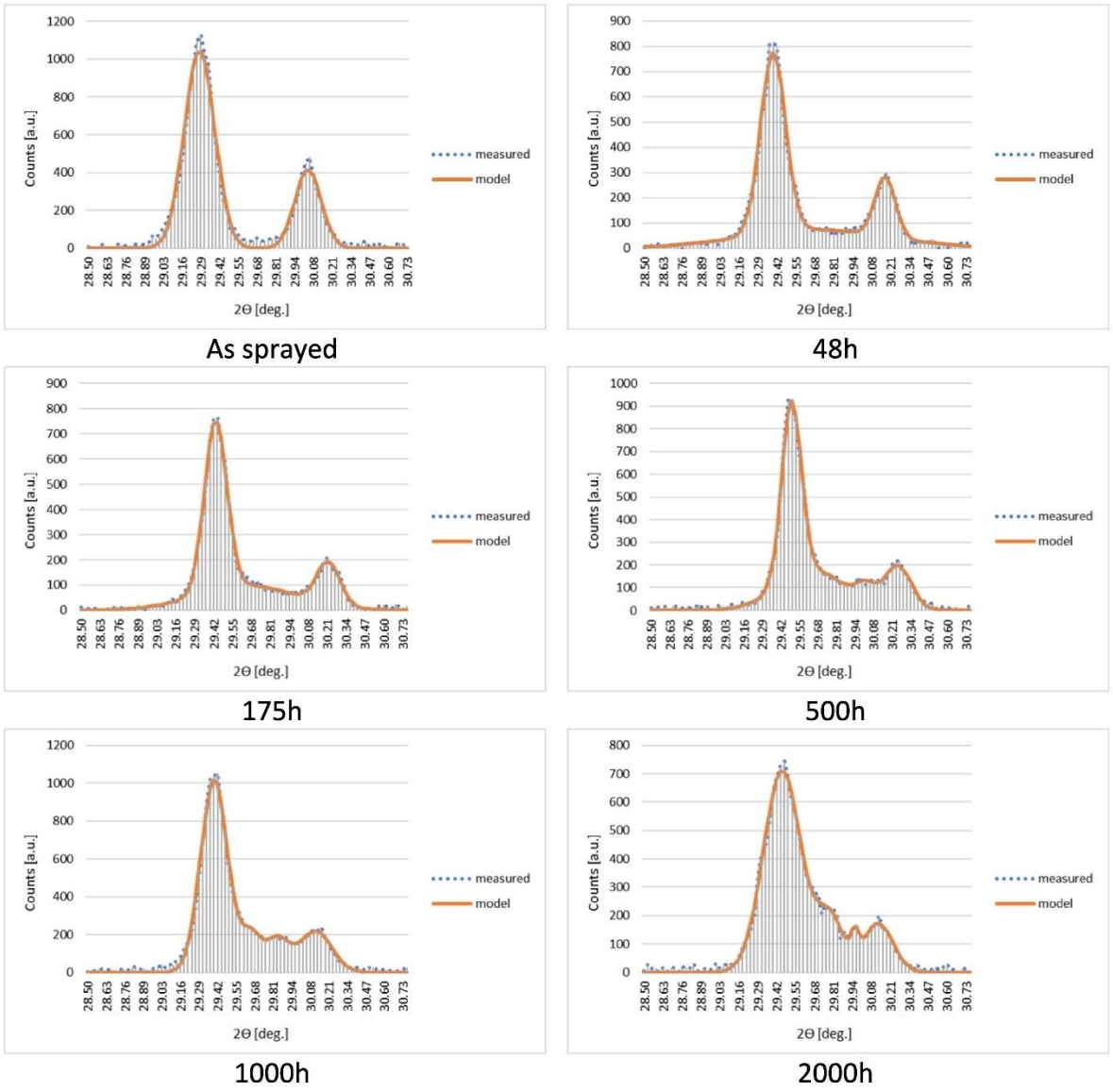

Figure 5.14. Phase constituent of the 25 % 8YSZ + 75 % GZO TBC system after long-term oxidation at temperature 1100 °C.

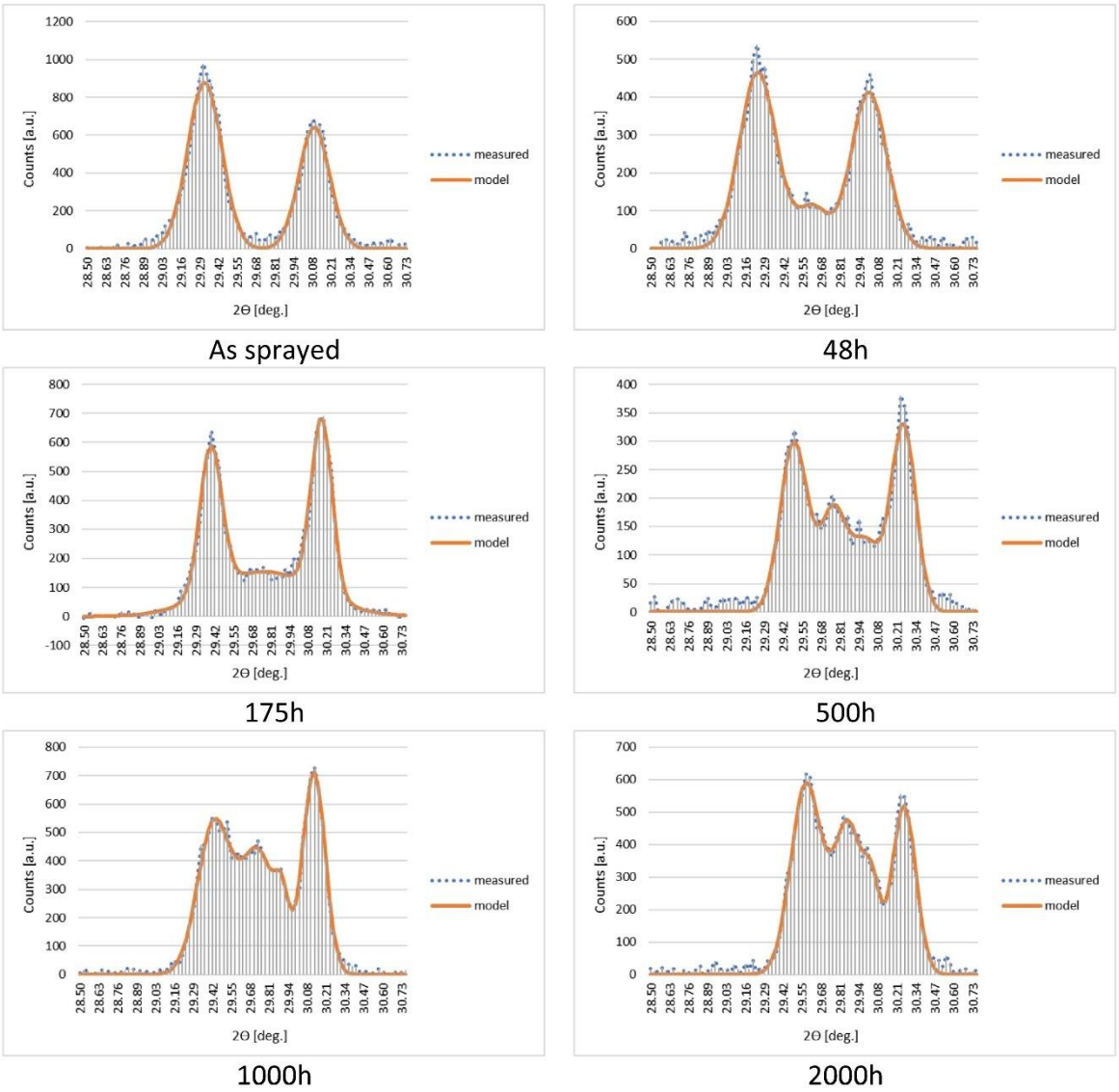

Figure 5.15. Phase component of 50 % 8YSZ + 50 % GZO TBC system after long-term oxidation at temperature 1100 °C.

This indicates the appearance of new phases resulting from the decomposition of the original $Gd_2Zr_2O_7$ and 8YSZ phases into the $Gd_{0.3}Zr_{0.7}O_{1.85}$ phase with a fluorite network (ICDD 04–010-3280) and the oxide $Gd_{0.05}Zr_{0.95}O_{1.975}$ (ICDD 04–020-5945) with a tetragonal type of lattice (essentially an oxide also containing yttrium - $(Y,Gd)_{0.05}Zr_{0.95}O_{1.975}$). It is also possible, in this case, to have a cubic phase with the ZrO_2 fluorite lattice and the formula $Gd_{0.18}Zr_{0.82}O_{1.91}$ (ICDD 04–011-7284). An analogous development of the phase component decomposition process was also observed in the case of the analyzed TBC coatings in the 50 % 8YSZ + 50 % GZO variant, as shown in **Figure 5.15.** The analysis of the degradation processes of the last type of coating is similar to that

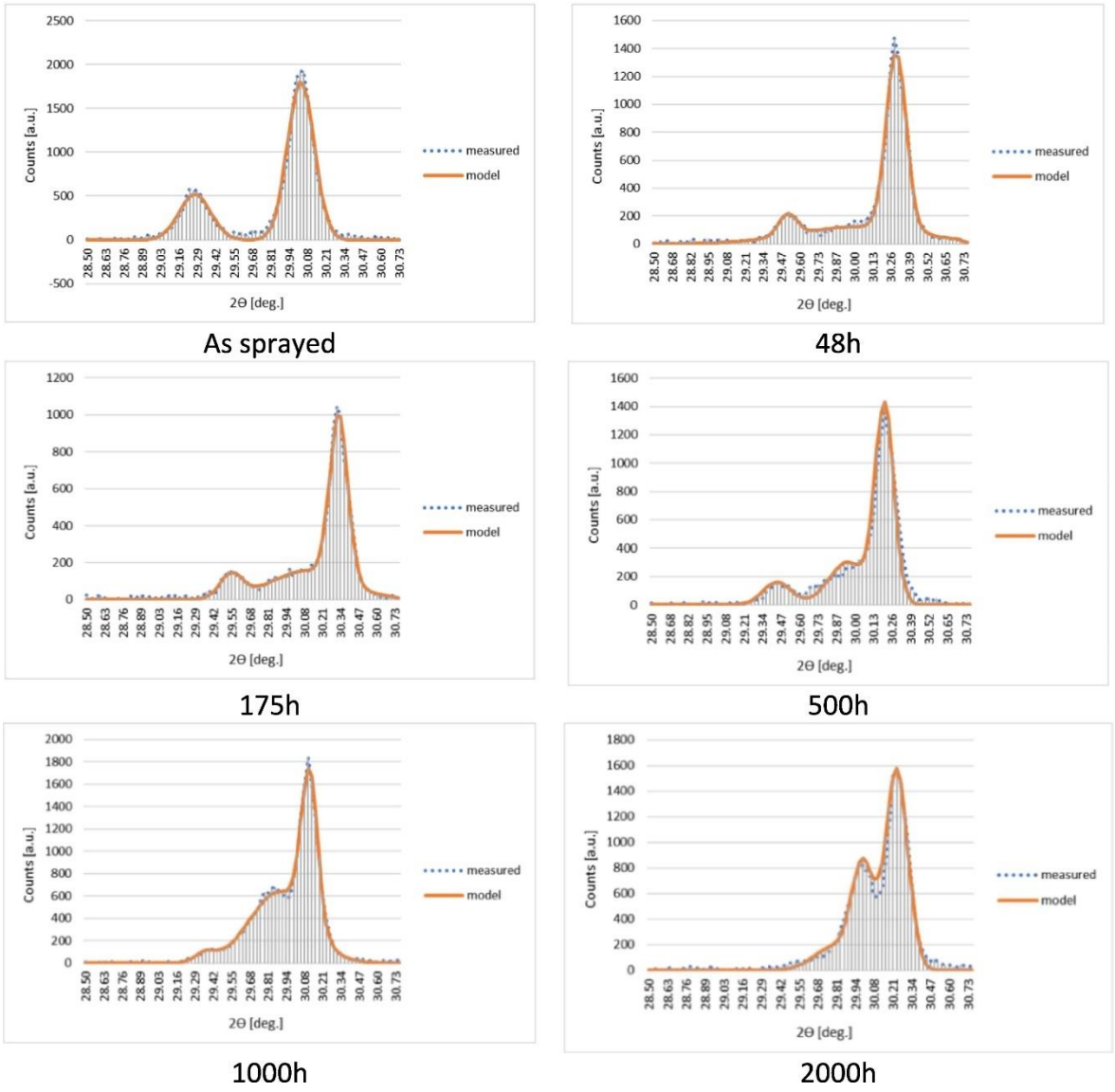

Figure 5.16. Phase component of 75 % 8YSZ + 25 % GZO TBC system after long-term oxidation at temperature 1100 °C.

of the previous cases, but note that, in the case of a lower content of gadolinium zirconate, this compound completely decomposes into the form of fluorite phase, and this form also disappears, giving the gadolinium oxide to zirconium oxide. A similar effect was not observed in the case of the system with a lower 8YSZ content. Of course, the amount of zirconium oxide decreased, but after 2000 h of exposure, its content in the TBC coatings was still high. In the 75 % 8YSZ + 25 % GZO variant, the final phase composition of the coating is as follows: tetragonal zirconium oxide modified with yttrium oxide with a variable content of Gd_2O_3 oxide. In its extreme form, it can also be the cubic form of zirconium oxide. important from the point of view of the operation processes of two-phase thermal barrier coatings. For this purpose, tests were carried out on model powders of the $Gd_2Zr_2O_7$ and

8YSZ types. The main question is at what temperature the decomposition process becomes important from the point of view of the operation processes of two-phase thermal barrier coatings. For this purpose, tests were carried out on model powders of the $Gd_2Zr_2O_7$ and 8YSZ types. The powders were mechanically mixed and homogenized and finally annealed in the form of pure powders and mixtures for 24 h in the temperature range of 800 to 1400 °C. The results of XRD diffraction studies illustrating changes in the phase composition are shown in **Figure 5.17.** The results of these studies confirm the observed phenomena in the form of gadolinium zirconate decay to forms with a lower concentration of Gd_2O_3 oxide, with its simultaneous incorporation into the structure of the 8YSZ phase and generation of tetragonal (possibly cubic) zirconium oxide with increased content of gadolinium oxide.

The data presented in **Figure 5.17.** show that the decomposition process in the 8YSZ + GZO system begins at a temperature of 1000 °C, which is indicated by a slight distortion of the diffraction reflection of the zirconate phase. At a temperature of 1100 °C and above, the scale of this effect is already very large, causing the disappearance of the pyrochlore GZO phase at 1300 °C and its complete transformation into gadolinium zirconates with a fluorite lattice and with a lower content of Gd_2O_3 oxide. At the same time, the tetragonal ZrO_2 phases are formed enriched with the oxide Gd_2O_3 and the primary Y_2O_3.

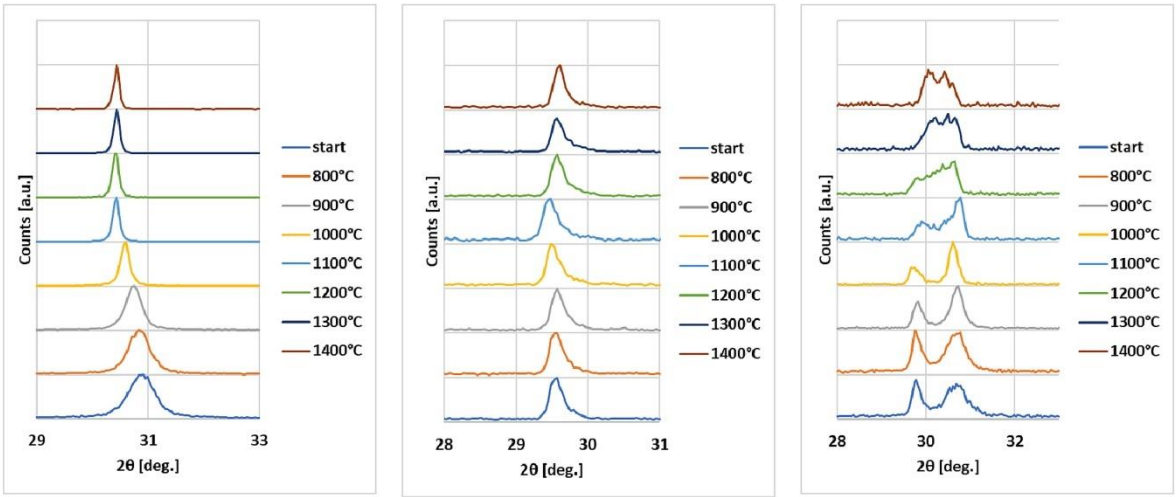

Figure 5.17. Phase constituent of pure 8YSZ and GZO powders, as well as the equally weighted mixture 8YSZ + GZO, as a function of temperature.

5.3. Summary

The results of YSZ+GZO dual phase composition research by XRD suggesting the formation of numerous phases with a lower concentration of Gd_2O_3 than in the base compound $Gd_2Zr_2O_7$, also it indicate the diffusion character of the decomposition processes of the basic compounds of the GZO + 8YSZ coatings. The revealed changes were practically only located in the zirconate phase. However, in the 8YSZ phase, they practically did not take place. This indicates the decomposition mechanism associated only with the transformation of the zirconate phase.

The phenomenon of phase decay was not observed in the case of single-phase oxidation of the GZO TBC system (results not presented in this publication) nor in the tests of modelled powders. The decomposition effect was observed only in the two-phase 8YSZ + GZO coatings and analogously in the mixture of model powders. This indicates that the driving force of the observed diffusion decay phenomena is the formation of thermodynamically more favorable tetragonal or cubic oxide phases based on zirconium oxide. An additional effect that accelerates the decomposition of the zirconate phase may be related to the vaporization of gadolinium oxide due to the higher vapour pressure of Gd_2O_3 compared to ZrO_2 [26], which is a typical phenomenon for this type of material and has been confirmed in numerous studies in the literature. Preferential vaporization of Gd_2O_3 during plasma spraying of $Gd_2Zr_2O_7$ would result in a deviation in the coating composition from the feedstock powders [27-28]. The loss of Gd_2O_3 in the non-stoichiometric GZO coating could induce phase instability, thus reducing the lifetime of TBCs due to the impurity phase.

Taking into account the phenomena in the system 8YSZ + SZO and 8YSZ + NZO (where SZO - $Sm_2Zr_2O_7$ and where NZO - $Nd_2Zr_2O_7$) described in [29], [18] as a reference point, it was assumed that the factor determining the stability of two-phase systems of this type is the cationic diameter of the rare earth element in the zirconate compound. Taking into consideration the research results presented in the work [30], it was assumed that the decreasing diameter of the lanthanide cations from lanthanum to lutetium would determine the decreasing stability of the phase composition in the 8YSZ system. It was also assumed that the expected decomposition phenomena will not require the assistance of liquid sulfate salts as in the case of the 8YSZ + SZO and NZO system [29], [18] and will be already intensive under the conditions of long-term oxidation in the air atmosphere.

5.4. Conclusion

Based on the results from both hot corrosion and pure oxidation studies, it can be noted that the degradation in the 8YSZ/GZO system involves complex, multi-step mechanisms that depend on thermal and chemical interactions. Sodium sulfate accelerates the formation of non-stoichiometric zirconate compounds in hot corrosion through various mechanisms, including synergistic degradation and the decomposition-reprecipitation mechanism described by Rapp. This degradation is not a simple additive effect of individual phases but includes interactions leading to specific compositional and morphological changes. In pure oxidation, the dominant process includes the thermally activated dissolution of zirconium oxide from 8YSZ into GZO, resulting in the decomposition of the pyrochlore structure into fluorite forms with a reduction in the 8YSZ phase. These interactions expose the sensitivity of the system to environmental and phase boundary conditions, whereby different dominant mechanisms emerge if it is in the presence of corrosive agents or in purely oxidative conditions. The dual-phase TBC system containing $Gd_2Zr_2O_7$ and 8YSZ has exhibited significant thermal instability during long-term oxidation at 1100 °C as a result of the mutual-interaction between the two phases. The literature reports interactions between $Gd_2Zr_2O_7$ and 8YSZ, resulting in non-stoichiometric zirconate compounds, Gd_2O_3 diffusion, and pore network formation driven by potential gradients and the evaporation of mobile components like Gd_2O_3 under high temperatures. The instability depends on such factors as the Madelung energy of the pyrochlore structure: in this respect, zirconia is more stable than gadolinium zirconates due to a greater strength of ionic interactions
n ZrO_4 tetrahedra. Extensive research studies are required in order to solve these problems and increase the stability of dual-phase TBC systems.

5.5. References.

1. Jesuraj, S. A., Kuppusami, P., Kirubaharan, A. K., & Rajasekaramoorthy, M. (2023). Advanced thermal barrier coatings for aerospace gas turbine engine applications. In *Advanced ceramic coatings for emerging applications* (pp. 151-183). Elsevier.
2. Thompson JA, Clyne TW. The effect of heat treatment on the stiff- ness of zirconia top coats in plasma-sprayed TBCs. Acta Mater. 2001;49(9):1565–75.
3. Ballard, J. D., Davenport, J., Lewis, C., Doremus, R. H., Schadler, L. S., & Nelson, W. (2003). Phase stability of thermal barrier coatings made from 8 wt.% yttria stabilized zirconia: A technical note. *Journal of Thermal Spray Technology*, *12*, 34-37.
4. Lashmi PG, Majithia S, Shwetha V, Balaji N, Aruna ST. Improved hot corrosion resistance of plasma sprayed YSZ/$Gd_2Zr_2O_7$ thermal barrier coating over single layer YSZ. Mater Charact. 2019;147:199–206.
5. Iqbal, A., Khan, M. J., & Moskal, G. (2022). A review on the deg- radation of coatings under hot corrosion process. Contemporary problems of power engineering and environmental protection, 27.

6. Leckie RM, Krämer S, Rühle M, Levi CG. Thermochemical com- patibility between alumina and ZrO_2–$GdO_{3/2}$ thermal barrier coat- ings. Acta Mater. 2005;53(11):3281–92.
7. Iqbal, A., & Moskal, G. (2023). Recent development in advance ceramic materials and understanding the mechanisms of thermal barrier coatings degradation. *Archives of Computational Methods in Engineering*, *30*(8), 4855-4896.
8. Jonnalagadda KP, Mahade S, Kramer S, Zhang P, Curry N, Li XH, Peng RL. Failure of multilayer suspension plasma sprayed thermal barrier coatings in the presence of Na_2SO_4 and NaCl at 900 C. J Therm Spray Technol. 2019;28:212–22.
9. Ozgurluk Y, Doleker KM, Karaoglanli AC. Hot corrosion behav- ior of YSZ, $Gd_2Zr_2O_7$ and YSZ/$Gd_2Zr_2O_7$ thermal barrier coat- ings exposed to molten sulfate and vanadate salt. Appl Surf Sci. 2018;438:96–113.
10. Liu ZG, Ouyang JH, Zhou Y, Li S. High-temperature hot corro- sion behavior of gadolinium zirconate by vanadium pentoxide and sodium sulfate in air. J Eur Ceram Soc. 2010;30(12):2707–13.
11. Bahamirian M, Hadavi SMM, Farvizi M, Rahimipour MR, Key- vani A. Enhancement of hot corrosion resistance of thermal bar- rier coatings by using nanostructured $Gd_2Zr_2O_7$ coating. Surf Coat Technol. 2019;360:1–12.
12. Jonnalagadda KP, Mahade S, Curry N, Li X-H, Markocsan N, Nylén P, Stefan Björklund R, Peng L. Hot corrosion mechanism in multi-layer suspension plasma sprayed $Gd_2Zr_2O_7$ /YSZ ther- mal barrier coatings in the presence of V_2O_5 + Na_2SO_4. J Therm Spray Technol. 2017;26(1–2):140–9.
13. Vaßen R, Bakan E, Mack D, Schwartz-Lückge S, Sebold D, Sohn YJ, Guillon O. Performance of YSZ and $Gd_2Zr_2O_7$/YSZ double layer thermal barrier coatings in burner rig tests. J Eur Ceram Soc. 2020;40(2):480–90.
14. Iqbal, A., Moskal, G., & Witala, B. (2024). Degradation mechanism of dual-phase thermal barrier coatings Gd2Zr2O7+ 8YSZ under hot corrosion in pure Na2SO4. *Journal of Thermal Analysis and Calorimetry*, 1-15.
15. Iqbal, A., Moskal, G., Głowacka, H. M., Pawlik, T., & Cavalerio, A. (2023). Phase decompositions of Gd2Zr2O7+ 8YSZ TBC systems under the condition of long-term high-temperature oxidation. *Surface and Coatings Technology*, *462*, 129471.
16. Senderowski C, Cinca N, Dosta S, Cano IG, Guilemany JM. The effect of hot treatment on composition and microstructure of HVOF iron aluminide coatings in Na2SO4 molten salts. J Therm Spray Technol. 2029;28(7):1492–510.
17. Barwinska I, Kopec M, Kukla D, Senderowski C, Kowalewski ZL. Thermal barrier coatings for high-temperature perfor- mance of nickel-based superalloys: a synthetic review. Coatings. 2023;13(4):769.
18. Moskal G, Jucha S, Mikuśkiewicz M, Migas D, Jasik A. Atypical decomposition processes of Sm2Zr2O7+ 8YSZ dual- phase TBCsduring hot corrosion. Corros Sci. 2020;170: 108681.
19. Rapp, R. A. (2002). Hot corrosion of materials: a fluxing mechanism?. *Corrosion science*, *44*(2), 209-221.
20. Xu Z, He L, Mu R, He S, Huang G, Cao X. Hot corrosion behavior of rare earth zirconates and yttria partially stabilized zirconia thermal barrier coatings. Surf Coat Technol. 2010;204(21–22):3652–61.
21. Dudnik EV, Lakiza SN, Hrechanyuk NI, Ruban AK, Red'ko, V. P., Hlabay, M. S., & Myloserdov, A. B. The Gd2Zr2O7-based materials for thermal barrier coatings. Powder Metall Met Ceram.2018;57:301–15.
22. Mahade, S. (2018). Functional performance of gadolinium Zirconate/Yttria stabilized zirconia multi-layered thermal barrier coatings (Doctoral dissertation, University West).
23. Cao XQ, Vassen R, Jungen W, Schwartz S, Tietz F, Stover D. Thermal stability of lanthanum zirconate plasma-sprayed coating. J Am Ceram Soc. 2001;84(9):2086–90.
24. Liu XY, Che JW, Yi H, Liang GY. Chemical compatibility between Ln2Zr2O7 (Ln= Nd, Sm, Gd) and tetragonal yttria stabilized zirconia after annealing at high temperatures. Mater Lett. 2019;234:159–62.
25. Liu XY, Che JW, Yi H, Liang GY. Influence of powder states on the composition and phase stability of LZ/YSZ composite thermal barrier coatings. Ceram Int. 2018;44(16):20291–8.
26. Schulz, U., Saruhan, B., Fritscher, K., & Leyens, C. (2004). Review on advanced EB-PVD ceramic topcoats for TBC applications. *International journal of applied ceramic technology*, *1*(4), 302-315.
27. Mauer, G., Sebold, D., Vaßen, R., & Stöver, D. (2012). Improving atmospheric plasma spraying of zirconate thermal barrier coatings based on particle diagnostics. *Journal of thermal spray technology*, *21*, 363-371.
28. Bakan, E., Mack, D. E., Mauer, G., & Vaßen, R. (2014). Gadolinium zirconate/YSZ thermal barrier coatings: plasma spraying, microstructure, and thermal cycling behavior. *Journal of the American Ceramic Society*, *97*(12), 4045-4051.
29. Migas, D., Moskal, G., & Jucha, S. (2022). Hot corrosion behavior of double-phase Nd2Zr2O7-YSZ thermal barrier coatings. *Surface and Coatings Technology*, *449*, 128955.
30. Poerschke, D. L., & Levi, C. G. (2015). Effects of cation substitution and temperature on the interaction between thermal barrier oxides and molten CMAS. *Journal of the European Ceramic Society*, *35*(2), 681-691.

6. LANTHANUM CERATE BASED TBCS

6.1. Introduction to LCO based TBCs

Thermal barrier coatings (TBCs) play a crucial role in boosting the performance and longevity of modern gas turbines, flame tubes, marine propulsion systems, rockets, ramjets, aerojet fuel engines, Vanes, blades, and combustion chambers where elevated temperatures are essential for optimal power generation [1]. Conventional yttria-stabilized zirconia (YSZ) is frequently utilized as a TBCs material due to its ability to provide robust protection against high temperatures for underlying substrates. But YSZ encounters restrictions that impede its extended applications, notably in terms of phase transitions at high temperatures (t'-phase→ cubic phase) typically below 1200 °C (and subsequently to monoclinic phase during cooling) [2]. Moreover, at high temperatures as the splats become denser and porosity diminishes, the strain tolerance decreases while the elastic modulus values increase. These all of the processes collectively accelerate the spallation process to the topcoat YSZ layer [3].

In addition to the aforementioned YSZ limits, the growing need for enhanced thrust and elevated operating temperatures in the gas turbines, nuclear reactors, gas barrels, combustion chambers of modern jets necessitate the development of next-generation thermal barrier ceramic materials. Several approaches are being explored, such as incorporating stabilizers with lower reactivity, investigating alternative ceramic materials with unique crystal structures like rare earth niobates, rare earth tantalates, rare earth zirconates, new strategies and design of solid-state depositions, advanced thermal spray techniques and multi-phase to functional graded systems (FGS). These strategies are currently in the research and development phase [4],[5]. Pyrochlore multi-functional materials $A_2B_2O_7$ (where A represents a +3 cation ranging from La to Lu and B represents a +4 cation such as Hf, Ce, Zr) substituting the anion within an ionic crystal with different elements leads to

phonon dissipation, resulting in an exceptionally low thermal conductivity for these compounds. Especially advanced ceramic zirconates in replacement to conventional ceramic are highly valued for their many applications, including solid oxy-fuel cells (SOFC) [6], advanced protective catalysis [7], potential for clean energy [8], thermoelectric properties [9], and for high temperature stability [10]. Several ceramic materials (pyrochlore, fluorite, perovskites and garnets) are currently under research consideration for thermal barrier materials, namely gadolinium zirconate ($Gd_2Zr_2O_7$), lanthanum zirconate ($La_2Zr_2O_7$), yttrium aluminum garnet ($Y_3Al_5O_{12}$), lanthanum hexaaluminate ($LaAl_{11}O_{18}$), lanthanum hafnate ($La_2Hf_2O_7$), magnesium zirconate ($MgZrO_3$), lanthanum magnesium aluminate $LaMgAl_{11}O_{17}$, lanthanum cerate ($La_2Ce_2O_7$), and strontium zirconate ($SrZrO_3$) [4]. Among various ceramic barrier materials, lanthanum cerate ($La_2Ce_2O_7$) has received widespread attention as a promising material for high temperature applications due to its exceptional thermophysical properties, including extremely low thermal conductivity (ranging between 0.5 and 1.02 W/m^{-1} K^{-1} at 1200 °C), an unusually high thermal expansion coefficient (12.3–12.6 × 10^{-6}/K at 300–1200 °C) for stress relief during thermal cycling, and excellent thermal phase stability (high melting point (2251–2297 °C)) [11]. LC stands out as one of the few cubic fluorite materials capable of performing effectively as a single layer in TBC coatings due to high phase stability and higher thermal expansion coefficient compared to YSZ, attributed to its defect fluorite structure with a 1/8 vacancy at the oxygen site.

LC holds promise as a TBCs, but its interaction with alumina (Al_2O_3) from TGO (thermally grown oxide) at high temperatures presents a challenge. This reaction, occurring around 1250 °C, forms lanthanum aluminate ($LaAlO_3$). $LaAlO_3$ exists in a stable phase at room temperature, but transforms to a less desirable bauxite structure above 450°C. Upon cooling, this bauxite $LaAlO_3$ undergoes a further transformation to a rhombohedral form, creating a heterogeneous microstructure with internal stresses within the $LaAlO_3$ layer. This weakens the LC coating, potentially reducing its thermal conductivity and increasing the risk of cracking and spallation [12].

Singh et al. [13] investigate the hot corrosion mechanism of three types of coatings $La_2Ce_2O_7$ (LC), $La_2Ce_2O_7$ -1 wt% GNP (LCG), and $La_2Ce_2O_7$ - 0.5 wt% CNT - 1 wt% GNP (LCGC) prepared via APS experimented against harsh vanadate-sulfate-containing molten salt environment at 1350 °C for varying time durations (where GNP; graphene nanoparticles, and CNT; carbon nanotubes). Through meticulous analysis, it was found that all three coatings, particularly the CNT/GNP-reinforced LCGC composite coating, displayed

promising resistance against aggressive corrosion. Notably, LCGC coatings exhibited the highest resistance to molten salt penetration, attributed to their dense and pore-free structure. Moreover, the inclusion of GNP and CNT within the LC matrix significantly bolstered the coatings' durability, evident from the reduced porosity levels and enhanced thermal stability post-hot corrosion testing.

Consequently, alternative materials or strategies may be necessary for LC-based TBCs in applications exceeding these critical temperatures. The hot corrosion properties of bilayer ceramic topcoats, specifically lanthanum cerium oxide (LCO)/YSZ and LCO/cluster paired zirconia (Gd,Dy,Y)SZ plasma sprayed, corrosion resistance under Type I conditions were investigated by P.G. Lashmi [14]. Results showed that the LCO/(Gd,Dy,Y)SZ bilayer coating with a 100 μm LCO thickness exhibited superior hot corrosion resistance compared to the LCO/YSZ system. Notably, the phase transformation from t′-ZrO_2 to m-ZrO_2 was significantly reduced by 60% in the LCO/(Gd,Dy,Y)SZ TBC compared to LCO/YSZ. Praveen et al. [15] examined LC and role of the rare earth oxide (REOs) dopants powder and coatings, where it was concluded that YSZ coatings experienced complete infiltration by molten Volcanic ashes (VA), leading to microstructural densification and phase alterations, while VA mitigation of all LC and other REOs doped LC coatings demonstrated resistance to infiltration by forming a phase-rich La-Ce apatite sealing layer. Yttrium oxide doped LC coating exhibited the least infiltration, followed by ytterbium and gadolinium oxide doped LC, attributed to the composition of their La-Ce apatite phase. In contrast to the YSZ TBCs, the LC TBCs effectively prevented CMAS penetration by forming a dense interaction layer between CMAS deposits and the LC coating. Initially, CMAS infiltrated LC through open pores and cracks, reacting chemically at 1250 °C to form the interaction layer. This layer comprised various compounds, including $Ca_2(La_xCe_{1-x})_8(SiO_4)6O_{6-4x}$ (rod phase), CeO_2 (globular phase), $CaAl_2Si_2O_8$, and $MgAl_2O_4$. The region affected by CMAS initially expanded but stabilized after 40 hours, indicating the growth of the interaction layer. The formation of the interaction layer proceeded in two stages: initial infiltration and reaction, sealing pores, followed by further reaction with CMAS leading to slow growth over time [16].

Hot corrosion is a particularly severe kind of material deterioration that affects TBCs. This deterioration is further accelerated in corrosive settings, which are frequently caused using low-quality fuels and byproducts. Fuels with sodium and vanadium-based compounds

are the principal sources of hot corrosive action, resulting in the creation. To address current TBCs vulnerabilities, it is suggested to develop bi-layer/multi-layer ceramic TBCs, composite dual-phase TBCs, and make modifications using thermal spray techniques. However, the existing literature has yet to investigate the hot corrosion tendencies of composite dual-phase TBCs YSZ/LCO coatings in molten sulphates produced through plasma spraying methods. Author antecedent research group revolved around an in-depth investigation of the long-term isothermal oxidation, and hot corrosion behavior of a dual-phase composite system comprising GZO+YSZ [17], NdZO+YSZ [18], and SmZO+YSZ [19] composition over an extended temporal span. The primary focus of this earlier work encompassed elucidating the intricate phenomenon of phase decomposition occurring within this ceramic tandem. The genesis of this phenomenon was attributed to the intricate interplay and reciprocal influences in terms of mutual interaction existing between the constituent ceramic materials, namely GZO, NdZO, SmZO and YSZ.

Motivated by the insights gleaned from the preceding research, the present study endeavors to extend the analytical purview to a distinct but interrelated realm, namely the domain of hot corrosion analysis. In particular, the interest herein lies in dissecting the corrosion mechanisms exhibited by the LCO+YSZ dual-phase composite in an environment typified by the presence of pure sodium sulfate (Na_2SO_4). Notably, a conspicuous dearth of comprehensive literature pertains to the specialized investigation of hot corrosion phenomena exclusively in the context of dual-phase TBCs and pure sodium sulfate. The current composite system sprayed via APS is to address the existing knowledge gap, further elucidate the intricacies of hot corrosion behavior, and contribute to the broader scientific discourse.

6.2. Results and discussion

6.2.1. Characterization of feedstock powders

The SEM microstructure analysis of the powdered YSZ and LCO raw feedstock materials, as shown in **Figure 6.1.** At an imaging voltage of 25.0 kV and 100x magnification using the S-3400N SEM, the SEM images offer a macroscopic view of the YSZ and LCO particles, showcasing the powder surface morphology and particle distribution within the raw feedstock. The powder materials exhibit a spherical shape with voids and a varied size distribution is significant.

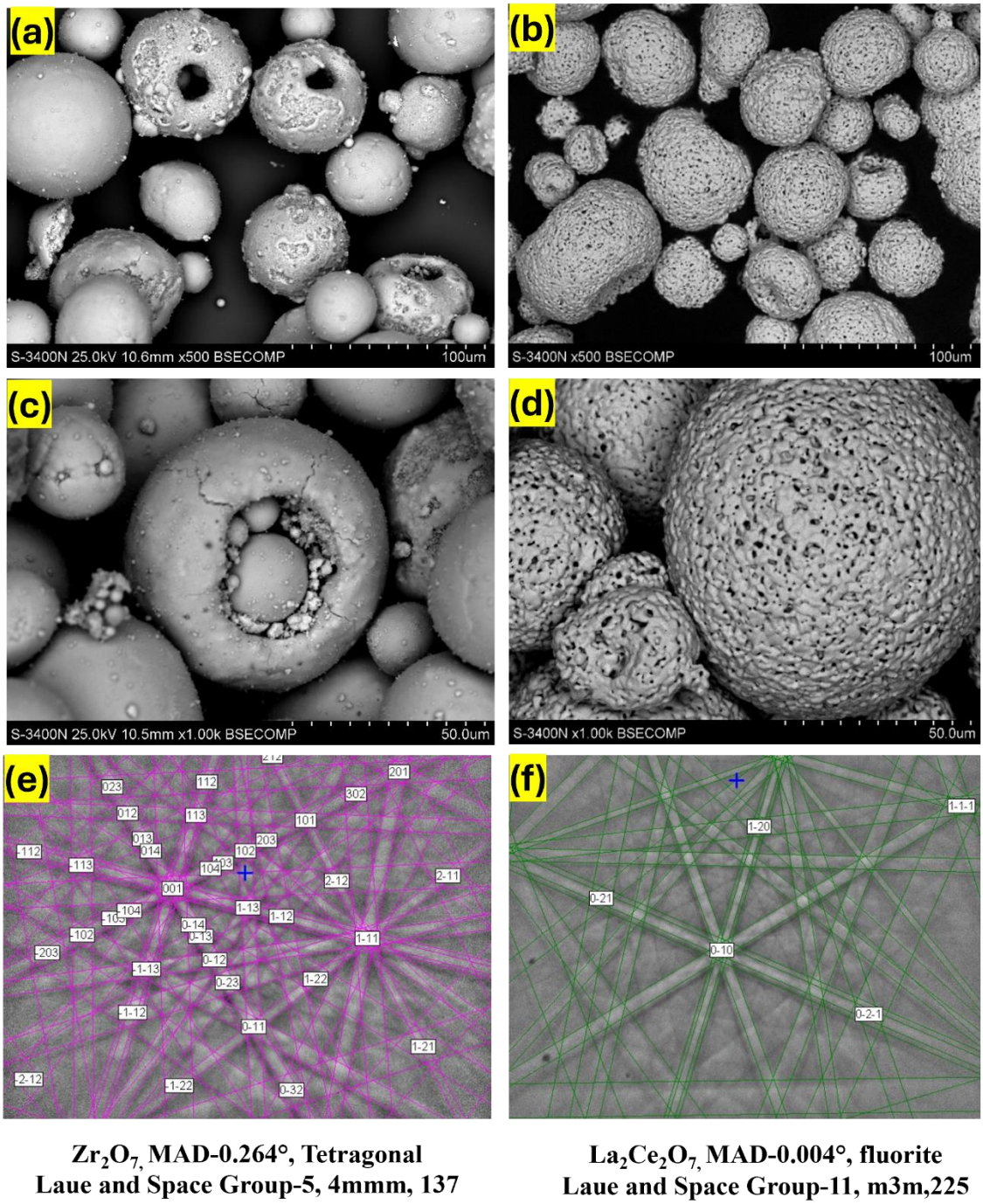

Figure 6.1. SEM micrographs of YSZ (a, c) and LCO (b, d) powders: high-resolution SEM images of powders at 100 µm and at 50 µm. Kikuchi lines: EBSD (e-f) method.

Spherical particles are often preferred in powder processing applications due to their favorable flowability and packing characteristics, which can facilitate uniform distribution and compaction during subsequent processing steps. The presence of voids within the particles can impact properties such as porosity and density, which are critical factors in

determining the performance of ceramic materials. Additionally, the varied size distribution of the particles may influence parameters such as sintering behavior and mechanical properties of the final product. The description of slight variations in the surface morphology of both YSZ and LCO particles, including flattened granules and individual spherical particles, suggests some degree of irregularity or aberrations in their geometry of particles. In Electron Backscatter Diffraction (EBSD) **Figure 6.1.** reveals the microstructural analysis of powder YSZ and LCO raw feedstock materials based on the crystallographic orientation and phase identification in materials. YSZ features a tetragonal crystal structure with unequal lattice parameters, while LCO adopts a pyrochlore arrangement characterized by interconnected polyhedral networks. Both compounds exhibit low mean atomic displacement parameters (MAD), with YSZ at 0.264° and LCO at 0.004°, suggesting minimal atom deviation within their respective lattices. The crystallographic properties of YSZ are defined by Laue and Space Group-5, 4mmm, with an International Tables for Crystallography (ITC) number of 137, while LCO is described by Laue and Space Group-11, m3m, with an ITC number of 225.

These specifications illustrate the symmetry elements present in their crystal lattices, crucial for understanding their structural stability and functional properties in various applications, from materials science to solid-state chemistry. **Figure 6.2.** illustrates the utilization of powder X-ray diffraction patterns for phase composition analysis. For LCO, the diffraction pattern reveals the $La_2Ce_2O_7$ cubic crystal structure with Fd3-m space group. the presence of a cubic $La_2Ce_2O_7$ phase with a fluorite type lattice structure, consistent with ICDD card number 01-084-8350. Conversely, YSZ exhibits a tetragonal phase of zirconium oxide, with the predominant phase displaying a tetragonal lattice structure, confirmed by ICDD card number 50-1089. Additionally, the distribution of granule or particle sizes in the powders used for APS-based coating deposition is a crucial consideration. This parameter holds particular significance in dual-phase composite coatings, especially when employing diverse feedstock materials. Ensuring the homogeneity of the microstructure requires a uniform distribution of structural elements. Both examined powders demonstrate high similarity in this regard, suggesting an anticipated even distribution of LCO and YSZ splats. As depicted in **Figure 6.2.,** the particle size distribution for YSZ and LCO powders falls within the same range, further supporting the expectation of homogeneity in the resulting coatings.

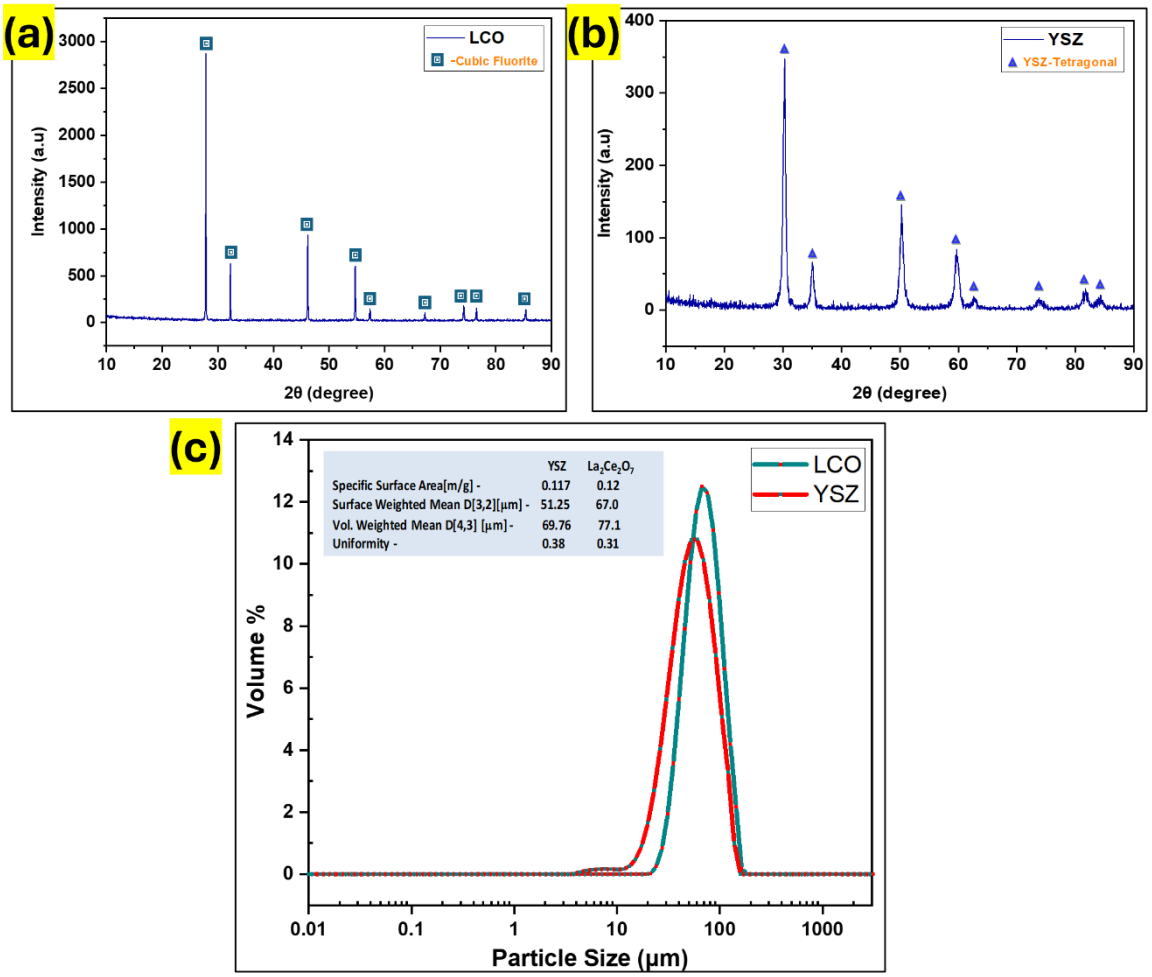

Figure 6.2. XRD Patterns for LCO (a) and YSZ (b) powders, indicating their phase composition. (c) Particle size measurements were obtained using a Master Sizer, with values following a log-normal distribution.

6.2.2. Characterization of coatings samples

The primary aim of the experiment was to examine the dual phase stability and surface degradation mechanisms of composite coatings, specifically those composed of a 50/50 combination of lanthanum cerate and zirconium oxide. The study was conducted in environments containing 100% liquid sodium sulfate (Na_2SO_4). Extensive research exists on the corrosion of TBC systems, but no previous studies have investigated the impact of pure Na_2SO_4 on the degradation of two-phase TBC composite systems specially cerates with zirconates composites. The current research focuses on coatings that involve novel composite mixtures of conventional YSZ and LCO systems. **Figure 6.3.** illustrates surface topography analysis, the surfaces of all samples appear similar, with no major differences

detected among them at high resolution. Presence of melted, partially melted, and un-melted particles can be seen which occur because not all particles undergo complete melting during the APS process, leading to a mix of different states on the coating surface. Cracks formation is a result of the rapid heating during the spraying process followed by equally rapid cooling. The coatings have numerous small pores, which are tiny voids or gaps within the coating material. Backscattered electrons colour contrast enables the differentiation of YSZ-related splats (appearing dark) from those associated with $La_2Ce_2O_7$ (appearing bright). The cross-sectional views of the TBCs system are shown in **Figure 6.4**. based on the microstructures and phase compositions observed, APS sprayed coatings were effectively fabricated with the specified $La_2Ce_2O_7$ + YSZ contents and orientations.

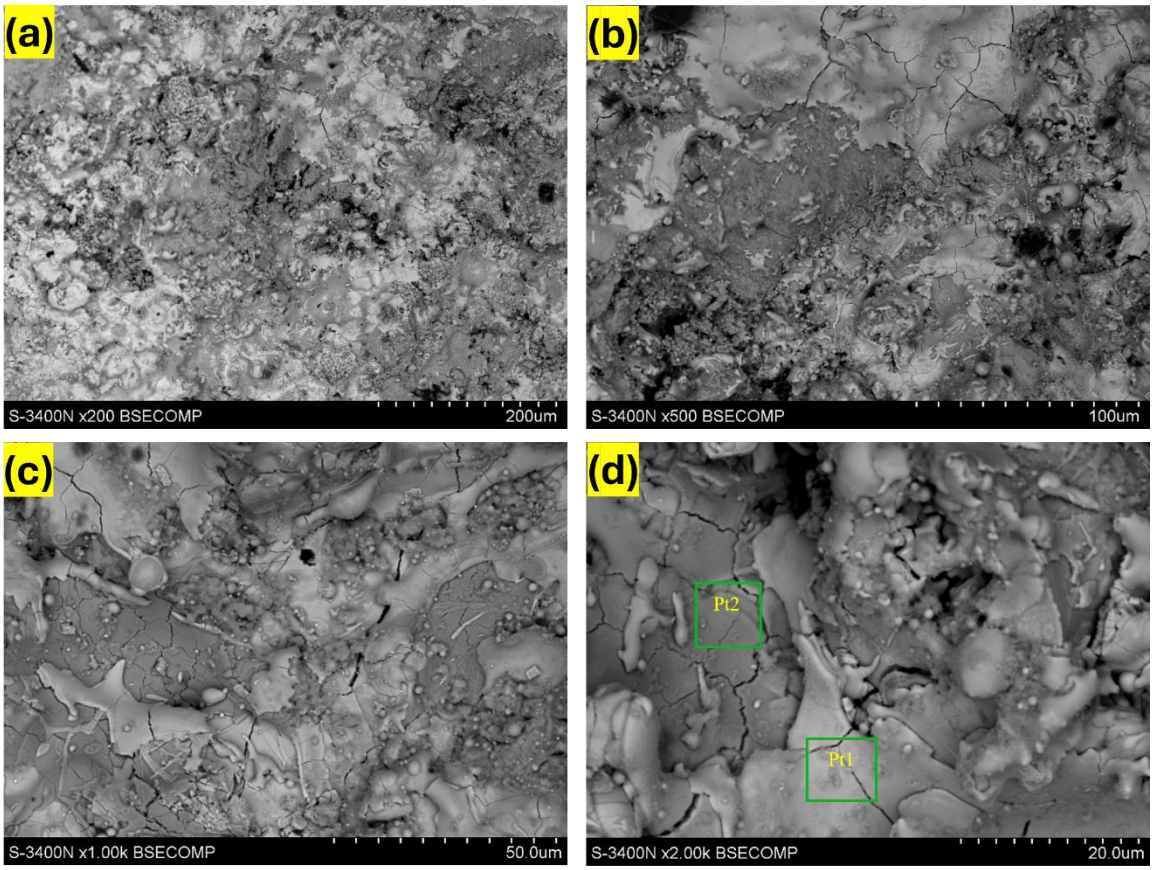

Weight %	O-K	Y-L	Zr-L	La-L	Ce-L
LCO+YSZ_pt1	16.5	0.6	11.4	34.8	36.8
LCO+YSZ_pt2	22.2	3.1	47.3	14.1	13.3

Atomic %	O-K	Y-L	Zr-L	La-L	Ce-L
LCO+YSZ_pt1	61.5	0.4	7.4	15.0	15.7
LCO+YSZ_pt2	64.9	1.7	24.3	4.7	4.4

Figure 6.3. SEM Micrographs of YSZ-LCO dual phase coatings: SEM top surface morphology, top surface EDX morphology

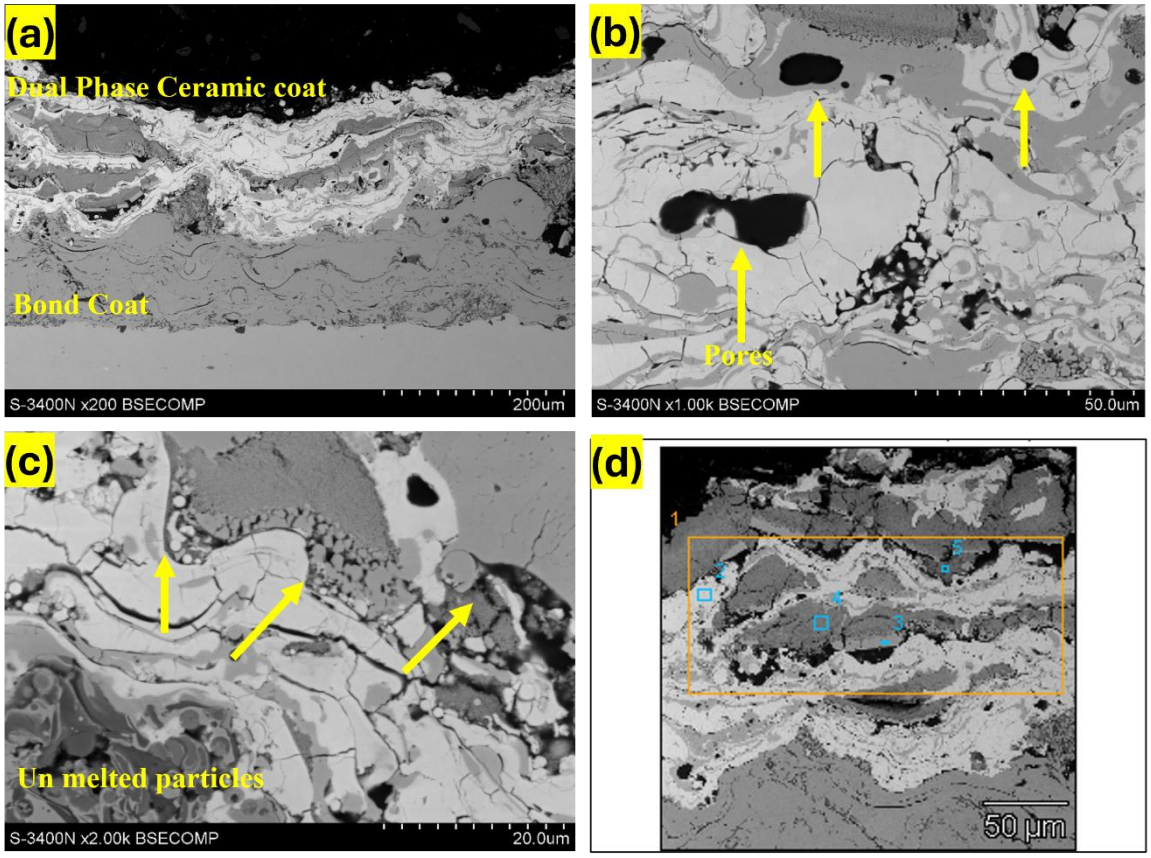

Weight %	O-K	Al-K	Cr-K	Ni-K	Y-L	Zr-L	La-L	Ce-L
LCO+YSZ _pt1	18.7	0.2		7.0	2.8	31.7	19.5	20.1
LCO+YSZ _pt2	14.7	0.2		5.6	0.2	5.9	32.8	40.6
LCO+YSZ _pt3	22.3	0.1	1.9	7.4	4.5	56.9	3.2	3.5
LCO+YSZ _pt4	21.7	0.1	2.2	8.5	6.1	53.3	3.7	4.4
LCO+YSZ _pt5	20.7	0.1	2.9	10.0	5.3	49.3	5.2	6.4

Atomic %	O-K	Al-K	Cr-K	Ni-K	Y-L	Zr-L	La-L	Ce-L
LCO+YSZ _pt1	59.7	0.3		6.1	1.6	17.8	7.2	7.3
LCO+YSZ _pt2	57.0	0.4		5.9	0.2	4.0	14.6	17.9
LCO+YSZ _pt3	61.0	0.2	1.6	5.5	2.2	27.3	1.0	1.1
LCO+YSZ _pt4	60.1	0.1	1.9	6.4	3.0	25.9	1.2	1.4
LCO+YSZ _pt5	58.6	0.2	2.6	7.7	2.7	24.5	1.7	2.1

Figure 6.4. SEM micrographs of YSZ-LCO dual phase coatings: SEM and EDX cross sectional surface morphology

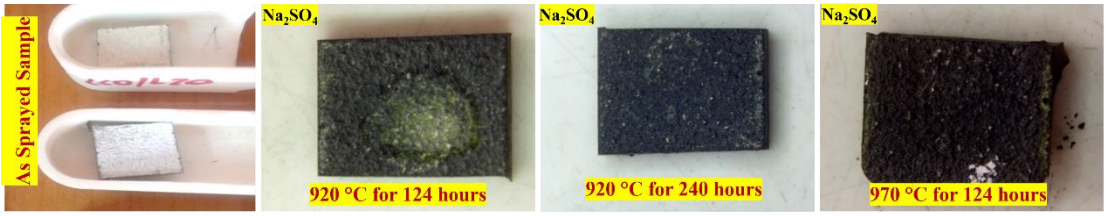

Figure 6.5. Stereomicrograph of YSZ-LCO dual phase coatings: Images of the examined high-temperature corrosion testing in (Na_2SO_4) corrosion environment at temperatures of 920°C for 240 hours and 970°C for 124 hours.

6.2.3. Degradation mechanism in LCO+YSZ

Dual phase TBCs is a stable system for high temperature applications. Our previous investigation also reveals that these types of systems can withstand at high temperature for prolong time. Although there are some structural changes observed during hot corrosion after several hours of long-term exposure, the visual inspection revealed the intact coatings, change in colour, formation of corrosion debris and minor depletion from the edges as it can be seen in the **Figure 6.5**. In the dual phase TBCs of LCO+YSZ system, initial decomposition leads to formation of four major primary active elements such as (ZrO_2, Y_2O_3, La_2O_3, CeO_2). These primary active elements make interactions further and leads to secondary products depending on the environment such as pure oxidation and hot corrosion particularly in the presence of pure sodium sulphate.

Significant results were obtained from the XRD pattern from **Figure 6.6.,** top surface morphology from **Figure 6.7. and Figure 6.8.,** cross-sectional Figure **6.9.**, particularly highlighting that the two-phase system tends to decompose or undergo hot corrosion at lower temperatures. This was evidenced by the formation chromites of lanthanum/yttria. At elevated temperatures, around 970 °C, the dissolution of phases was observed, like what we encountered in our previous GZO+YSZ dual phase TBCs experiments under pure oxidation conditions [17].

With cationic size of Y^{3+} = 104 pm and La^{3+} = 117 pm, and considering the structure based on $La_2Ce_2O_7$ and Y_2O_3 dopped ZrO_2 with a lattice parameter of **d = 3.18 Å**, it is observed mutual interactions among La_2O_3, CeO_2, ZrO_2, Y_2O_3, with assistance of Cr_2O_3, and NiO after hot corrosion. This results in multicomponent phase formation, including $LaCrO_3$ and $LaNiO_3$. Upon the deposition of La^{3+}, it is concluded that Y^{3+} occupying Ni^{2+} positions, while also allowing for the possible inclusion of Zr and Ce cations. A solid solution of La_2O_3 forms, represented as $(La,Y)_2O_3$, and NiO coexists as a solid solution with ZrO_2 and CeO_2 in NiO. Additionally, XRD detected formation of $(La,Y)_2O_3$ and La_2O_3 interacting with Cr_2O_3, resulting in two main compounds after exposure to 920°C: **$LaNiO_3$** and **$LaCrO_3$**. Further XRD pattern shows that 970°C at this temperature no change in the chromites but solid solution of Ce & Zr decomposed into Nio and $(Zr.Ce)O_2$. As $(La,Y)CrO_3$ +$(La,Y)NiO_3$ + $(Zr, Ce)O_2$ → $(La,Y)_2O_3$ → $(La,Y)_2$ $(Ce,Zr)_2O_7$ with d=3.12 and d=3.18 Å. SEM and EDX of (**Figure 6.7. – 6.8.**), cross sectional analysis (**Figure 6.9**.) results confirm and aligns with the finding obtained by XRD.

These findings, particularly the decomposition and phase dissolution observed at elevated temperatures in the dual phase system, guide our next set of experiments. Hot corrosion tests will be conducted at 920 °C, 950 °C, 970 °C, and 1000 °C, while samples subjected to pure oxidation will be tested at 900 °C, 950 °C, 1000 °C, 1050 °C, and 1100 °C to further explore the phase behavior under these conditions. It is important to note that this type of diffusional degradation in TBCs was not observed in the double ceramic layer (DCL) [20], and composite coatings under salt mixture with vanadium [21], this is the first report that explains the dual-phase degradation of LCO+YSZ ceramic coatings reveals new insights into how this degradation occurs due to phase dissolution and diffusional effects under pure sulphate hot corrosion, opening up new direction for further research.

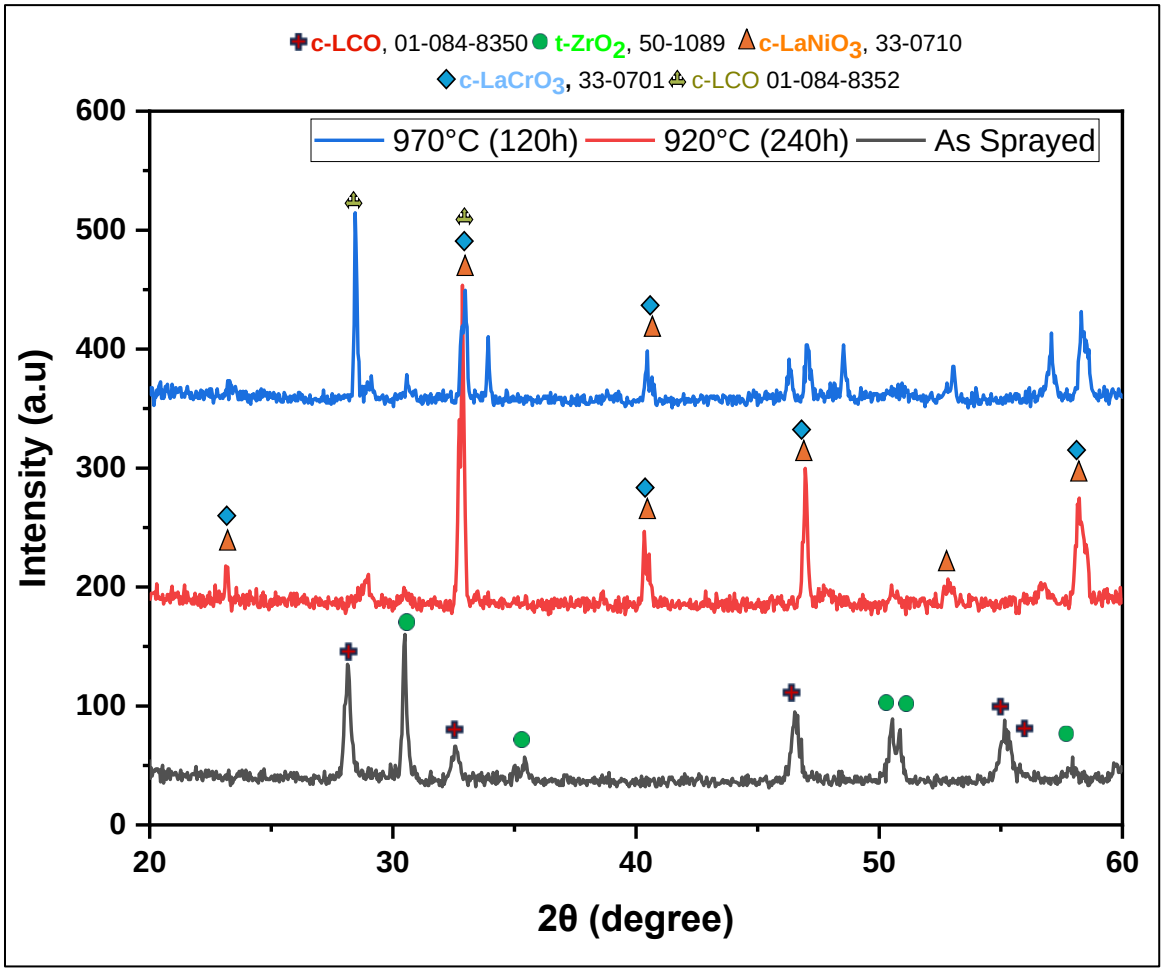

Figure 6.6 Diffraction pattern of heat-treated LCO-YSZ based dual phase coatings at 920°C (10 days) followed by XRD/SEM and further sintering at 970°C (4 days).

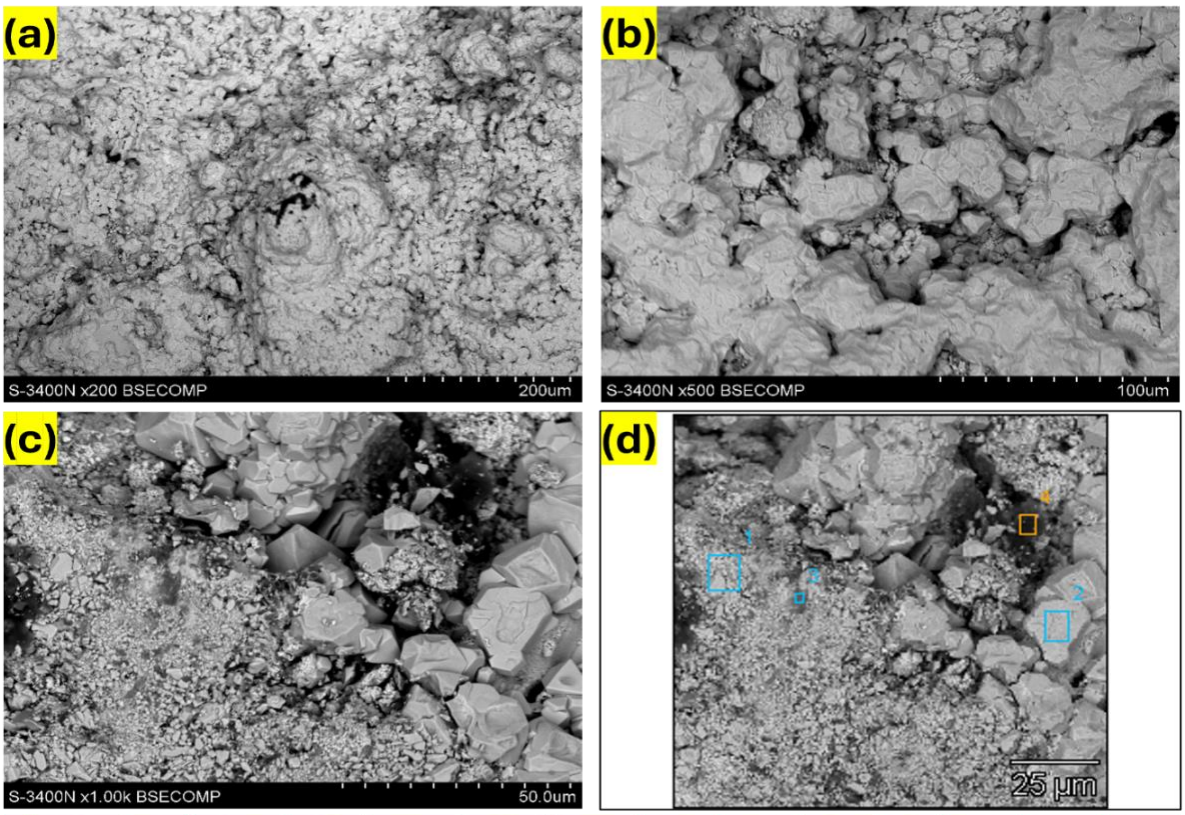

Weight%	O-K	Na-K	Al-K	Si-K	S-K	Cl-K	Ca-K	Cr-K	Ni-K	Y-L	Zr-L	La-L	Ce-L
pt1	12.5	0.1	0.7					17.0	4.1		2.8	46.4	16.4
pt2	11.4		0.6		0.2			25.0	2.2	0.0	0.6	57.0	2.8
pt3	18.1	0.2	1.1	2.2	1.0		12.3	15.6	5.2	0.3	2.7	36.1	5.2
pt4	31.7		0.5	20.2	0.7	0.9	1.4	9.0		0.0	3.4	24.4	7.8
Atom. %	**O-K**	**Na-K**	**Al-K**	**Si-K**	**S-K**	**Cl-K**	**Ca-K**	**Cr-K**	**Ni-K**	**Y-L**	**Zr-L**	**La-L**	**Ce-L**
pt1	46.1	0.3	1.5					19.3	4.2		1.8	19.8	6.9
pt2	42.0		1.3		0.5			28.3	2.2	0.0	0.4	24.1	1.2
pt3	48.9	0.4	1.8	3.4	1.4		13.2	12.9	3.9	0.1	1.3	11.2	1.6
pt4	61.1		0.5	22.2	0.6	0.8	1.1	5.3		0.0	1.1	5.4	1.7

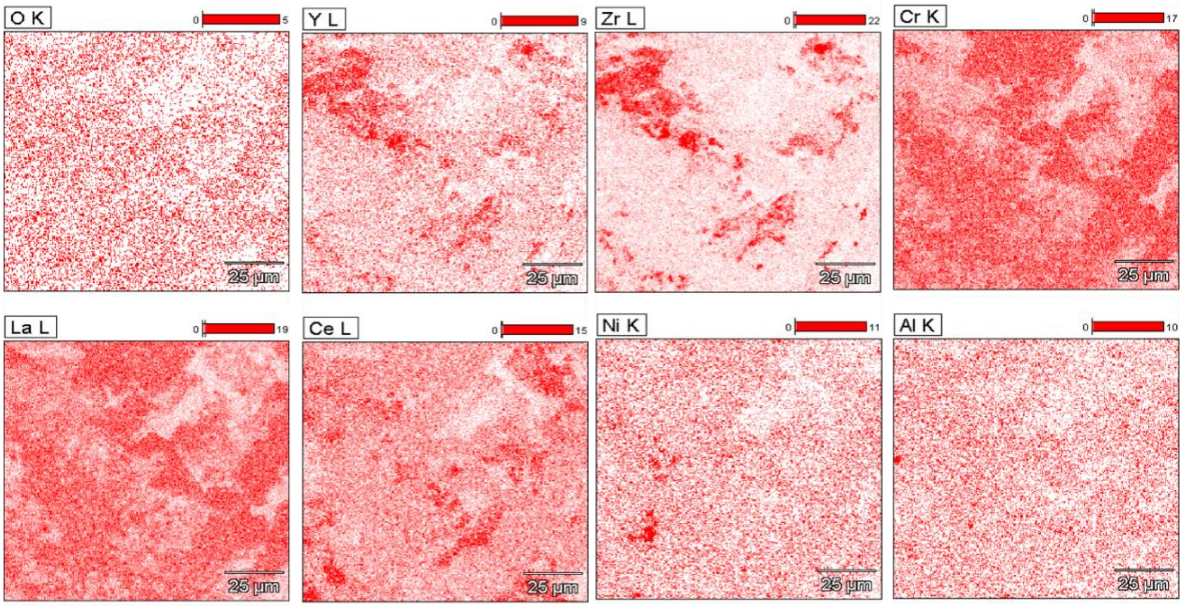

Figure 6.7. Top Surface SEM morphology and EDX analysis after hot corrosion 920 °C.

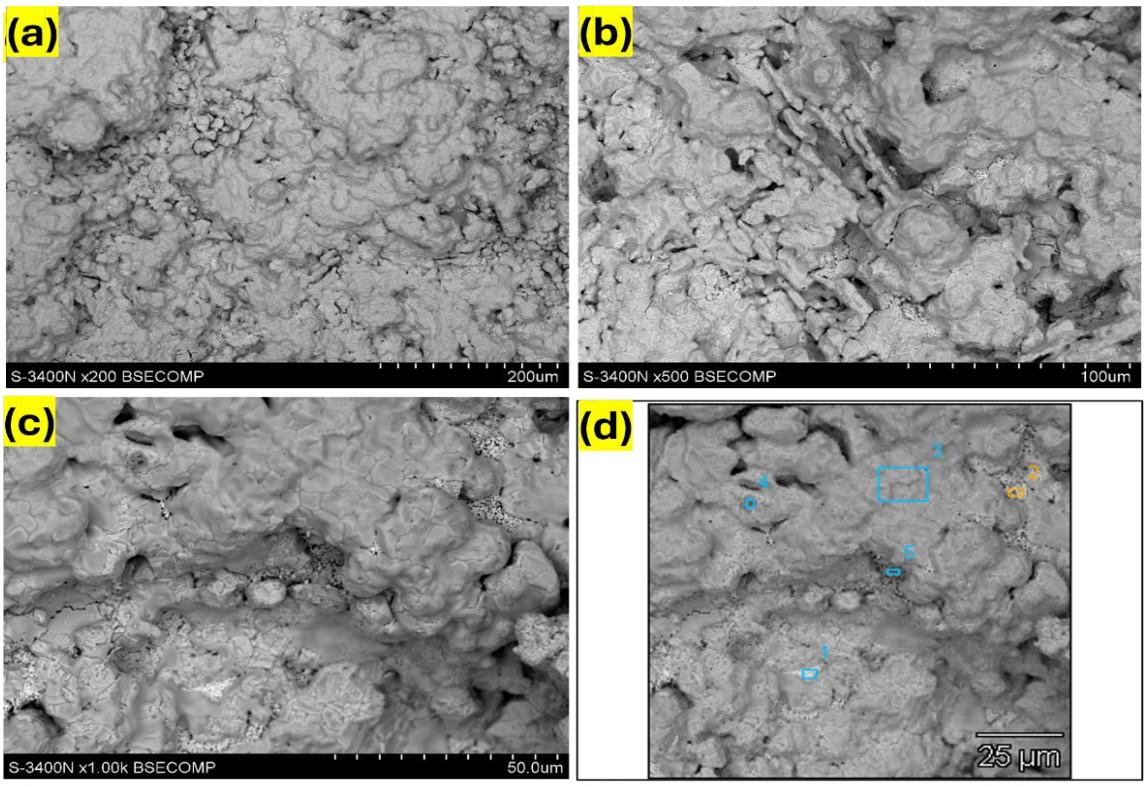

Weight%	O-K	Na-K	Al-K	Si-K	Cr-K	Fe-K	Ni-K	Y-L	Zr-L	Mo-L	La-L	Ce-L
Pt1	13.9	0.3			10.8					24.0	37.8	13.2
Pt2	13.8							0.3	5.4	11.7	16.7	52.2
Pt3	12.3	0.3			9.1					32.4	45.0	0.9
Pt4	21.6		0.1	0.1	7.8	16.7	26.9	0.0		7.4	18.8	0.6
Pt5	13.0	0.3			9.5			0.0		28.1	44.2	4.9
Atomic%	**O-K**	**Na-K**	**Al-K**	**Si-K**	**Cr-K**	**Fe-K**	**Ni-K**	**Y-L**	**Zr-L**	**Mo-L**	**La-L**	**Ce-L**
Pt1	50.9	0.7			12.2					14.7	15.9	5.5
Pt2	56.0							0.2	3.8	7.9	7.8	24.2
Pt3	47.2	0.9			10.8					20.8	20.0	0.4
Pt4	54.5		0.1	0.1	6.0	12.1	18.5	0.0		3.1	5.5	0.2
Pt5	49.0	0.8			11.0			0.0		17.7	19.3	2.1

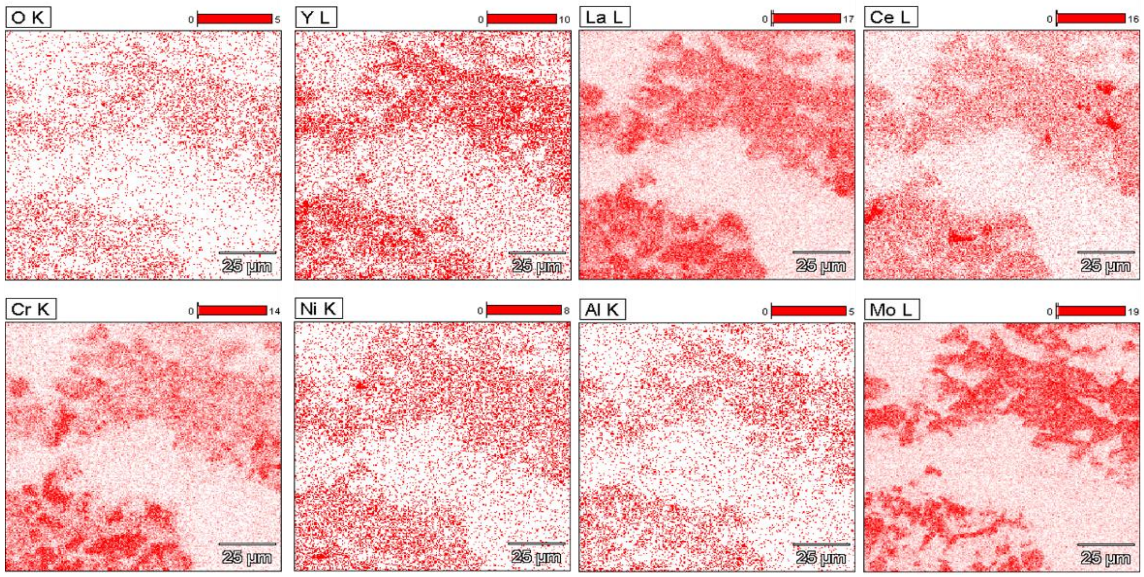

Figure 6.8. Top Surface SEM morphology and EDX analysis after hot corrosion 970 °C.

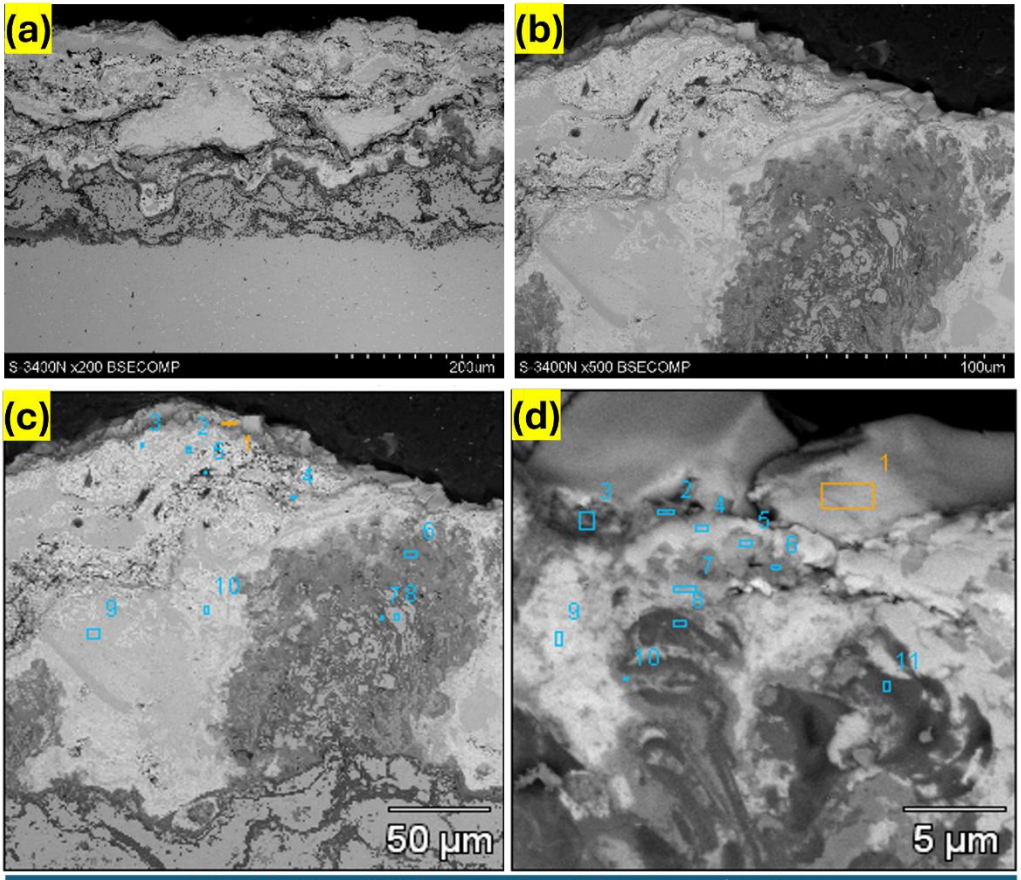

LCO+YSZ-970C-4d-920C-10days-(Na_2SO_4) - cross section (50 µm)

Weight %	O-K	Na-K	Mg-K	Al-K	Si-K	S-K	Cr-K	Fe-K	Ni-K	Y-L	Zr-L	La-L	Ce-L
pt1	36.3	1.6		1.0		16.4	4.1		10.0	0.4	2.1	26.1	2.0
pt2	25.9		0.1	1.5	0.4	2.8	21.8		12.7		1.7	30.1	3.0
pt3	26.8		0.1	1.7	0.4	1.8	22.9	3.6	21.2	0.2	2.1	17.0	2.1
pt4	22.6			1.1		1.4	18.6		10.9		1.5	41.8	2.2
pt5	31.6	1.7		1.0	0.3	10.9	8.9		9.8	0.5	2.1	31.1	2.1
pt6	26.5			1.2		2.7	17.4		41.0		1.6	7.8	1.8
pt7	22.3			1.1			7.2		25.8	1.1	18.5	14.7	9.2
pt8	28.0			7.3		0.7	17.8		38.6	0.5	1.4	4.1	1.5
pt9	20.5			1.3		1.3	8.0		10.1	0.4	5.0	18.1	35.4
pt10	24.5			3.5		0.4	9.5		55.3		1.4	3.6	1.8
pt11	30.4			13.1		0.7	15.3	0.5	31.3	1.1	1.3	4.9	1.4
Atomic%	O-K	Na-K	Mg-K	Al-K	Si-K	S-K	Cr-K	Fe-K	Ni-K	Y-L	Zr-L	La-L	Ce-L
pt1	67.4	2.0		1.1		15.2	2.4		5.1	0.1	0.7	5.6	0.4
pt2	60.5		0.2	2.1	0.5	3.3	15.7		8.1		0.7	8.1	0.8
pt3	58.9		0.2	2.3	0.5	2.0	15.4	2.3	12.7	0.1	0.8	4.3	0.5
pt4	59.6			1.7		1.8	15.0		7.8		0.7	12.7	0.7
pt5	64.9	2.5		1.2	0.3	11.2	5.6		5.5	0.2	0.8	7.4	0.5
pt6	57.0			1.6		2.9	11.5		24.0		0.6	1.9	0.4
pt7	58.0			1.7			5.8		18.3	0.5	8.5	4.4	2.7
pt8	56.3			8.8		0.7	11.0		21.2	0.2	0.5	1.0	0.4
pt9	60.0			2.3		1.8	7.2		8.0	0.2	2.6	6.1	11.8
pt10	53.7			4.6		0.4	6.4		33.0		0.5	0.9	0.4
pt11	57.3			14.7		0.6	8.9	0.3	16.1	0.4	0.4	1.1	0.3

LCO+YSZ-970C-4d-920C-10days-(Na_2SO_4) - cross section (5 µm)

Weight%	O-K	Na-K	Al-K	Si-K	S-K	Cr-K	Ni-K	Y-L	Zr-L	La-L	Ce-L
pt1	27.7		1.5	0.8	6.9	7.3	12.2	0.5	5.2	30.7	7.2
pt2	23.3		0.3				5.7	3.8	49.9	5.9	11.0
pt3	20.7		0.6		3.1		4.5	0.5	11.4	10.4	48.8
pt4	25.1	0.3	0.7		2.8	4.3	8.6	1.9	31.3	10.8	14.2
pt5	21.5		1.4		2.1		14.6	0.4	15.1	8.6	36.4
pt6	29.7		9.0		0.4	25.0	30.3	0.3	1.4	2.4	1.4
pt7	34.9		18.9		0.5	25.8	17.6	2.3			
pt8	23.0		1.5		0.3	4.2	69.2		1.0	0.8	
pt9	30.6	1.3	0.5		9.6	3.1	6.5	1.3	20.8	16.9	9.2
pt10	21.0		0.9		1.1	9.1	7.8	0.5	10.0	24.9	24.7
Atomic%	O-K	Na-K	Al-K	Si-K	S-K	Cr-K	Ni-K	Y-L	Zr-L	La-L	Ce-L
pt1	63.8		2.0	1.0	7.9	5.2	7.7	0.2	2.1	8.2	1.9
pt2	64.0		0.5				4.2	1.9	24.1	1.9	3.5
pt3	63.3		1.0		4.7		3.8	0.3	6.1	3.7	17.0
pt4	63.5	0.5	1.0		3.6	3.4	6.0	0.9	13.9	3.1	4.1
pt5	61.0		2.4		2.9		11.3	0.2	7.5	2.8	11.8
pt6	57.2		10.2		0.4	14.8	15.9	0.1	0.5	0.5	0.3
pt7	58.6		18.8		0.4	13.4	8.1	0.7			
pt8	51.8		2.0		0.3	2.9	42.4		0.4	0.2	
pt9	66.2	1.9	0.7		10.3	2.1	3.8	0.5	7.9	4.2	2.3
pt10	60.8		1.5		1.7	8.1	6.2	0.2	5.1	8.3	8.2

Figure 6.9. Cross sectional SEM morphology and EDX analysis after 970 °C.

Based on these findings, particularly the decomposition and phase dissolution observed at elevated temperatures for 920 °C, 970 °C, further set of hot corrosion (from 920 °C -1000 °C) and pure oxidation tests (950 °C -1100 °C) were performed to better investigate the phase behavior under these specific conditions. The XRD investigations **(Figure 6.10. and Figure 6.11.)**, along with the proposed reactions, reveal that in the presence of pure sodium sulfate, the YSZ-LCO degradation mechanism is significantly influenced by the specific elements present in the bond coat, mainly nickel (Ni) and chromium (Cr). Oxide from the TGO zone NiO and Cr_2O_3 upon interacting with TC layer formed the major corrosion products. In the case of LCO+YSZ, these interaction can be results of (Zr, Ce)O_2 and (La, Y)$_2O_3$ with NiO and Cr_2O_3. The possible interactions are NiO-(Zr, Ce)O_2 - (La, Y)$_2O_3$ and Cr_2O_3 -(La, Y)$_2O_3$. La_2O_3 can form a solid solution with Cr_2O_3 because La^{3+} and Cr^{3+} ions can substitute for each other in the crystal lattice. The formation of $LaCrO_3$ occurs because the La^{3+} ions can replace Cr^{3+} ions in the Cr_2O_3 structure, given their similar charge and compatible crystal structures. The interaction occurs because the lattice energies (the energy released when ions are added to the crystal lattice) of the La and Cr oxides are compatible, making it energetically favorable for these ions to substitute for each other in the crystal structure. In LCO+YSZ system, La_2O_3 (produced from the decomposition of $La_2Ce_2O_7$) reacts with Cr_2O_3 from the bond coat. The La^{3+} ions from La_2O_3 can substitute for Cr^{3+} ions in the Cr_2O_3 lattice, forming $LaCrO_3$. This happens because both La^{3+} and Cr^{3+} have the same charge and similar ionic radii, making the substitution energetically favorable. Similarly, La_2O_3 reacts with NiO to form $LaNiO_3$. Although Ni^{2+} has a different charge, the reaction forms a different compound with a compatible crystal lattice type structure, where the La^{3+} ions interact with the NiO matrix, creating a stable perovskite structure ($LaNiO_3$). The formation of these solid solutions and resulting compounds based on the lattice type ($LaCrO_3$ and $LaNiO_3$) alters the microstructure of the coating, which could impact its thermal and mechanical properties. Solid solutions can either strengthen the material by creating a more complex and stable phase, or they can lead to brittleness if the resulting phase is less ductile. The new phases compounds based on the lattice type ($LaCrO_3$ and $LaNiO_3$) might offer different corrosion resistance compared to the original materials. At high temperatures like 920°C, nickel can form a solid solution with other elements (such as Cr, Al, or Ni) present in the bond coat or diffused from TGO layer. YSZ typically has distinctive peaks in XRD patterns. At this temperature, the peak positions of the nickel solid solution in XRD

coincide with the peak positions of zirconia. As a result, the nickel solid solution diffraction peaks can overshadow or obscure the peaks of zirconia, making it difficult to clearly identify the zirconia phase in the XRD pattern. This can be explained as Nickel solid solutions generate stronger or broader peaks that mask the weaker zirconia peaks, especially if the nickel phase is more dominant in terms of volume fraction. Similar study has noted [21] the overlapping diffraction peaks, where the nickel solid solution obscures the zirconia phase, and highlights how synthesis conditions can influence phase distribution and the characteristics of the interfaces. Furthermore, a combined oxide phase where Zr, Ce, and Y atoms are incorporated into the same crystal lattice, forming a homogeneous mixture, depending on their stability at high temperatures, these compounds can either protect the underlying materials or accelerate degradation if they are prone to cracking or oxidation, which needs further investigation. $ZrO_2(Y_2O_3) + CeO_2 \rightarrow (Zr, Ce)O_2$

Figure 6.10. revealed that $LaCrO_3$ has been observed to exist in two distinct crystallographic forms—orthorhombic 33-0701 and cubic 75-0441—at elevated temperatures. XRD analysis revealed that, under high-temperature conditions, both phases coexist, as indicated by diffraction peaks corresponding to d-values of 2.74 Å, 1.94 Å, and 1.58 Å. However, the orthorhombic phase is more stable and prevalent, as evidenced by the greater number of XRD peaks associated with this structure. The orthorhombic form's stability is attributed to its lower symmetry and more complex crystal lattice, which, despite the presence of the higher-symmetry cubic phase, remains energetically favorable at elevated temperatures.

o-$LaCrO_3$ also demonstrates superior thermal properties, particularly in terms of spectral remittance and heat transport. Its lower thermal conductivity and higher thermal emittance make it more effective in insulating and managing thermal radiation, which is critical in TBCs applications. The formation of corrosion products, and their presence indicated that coatings peels off from the edges/top surface with YSZ-LCO/BC interface. This type of conclusion is not reported in the literature of TBCs-hot corrosion analysis. In the context of high-temperature materials and solid-state chemistry, both (Ni) and (Cr) can form various complex oxides and perovskite structures. To understand their formation, equation was proposed at how these elements combine with others to form solid solutions or compounds, particularly in the context of perovskite structures, which are commonly represented by the general formula ABO_3 or related structures like $A_2B_2O_6$. In perovskites,

La^{3+} and Y^{3+} occupy the A-sites, while Ni^{2+} or Cr^{3+} occupy the B-sites, leading to materials with specific thermal properties.

Table 6.1. Basic Proposed equation for current TBCs System.

$2\ Na + ½\ O_2 \rightarrow Na_2O$ (Basic Species)	(1)
$S + O2 \rightarrow SO_2$; $SO_2 + ½\ O_2 \rightarrow SO_3$ (Acidic Species)	(2)
$SO3 + Na_2O \rightarrow Na_2SO_4$ (Formation of Salt)	(3)
$YSZ + SO_3 \rightarrow Y2(SO4)_3 + m\text{-}ZrO_2$ (Degradation)	(4)
$La_2O_3 + 2NiO \rightarrow 2LaNiO_3$	(5)
$La_2O_3 + Cr_2O_3 \rightarrow 2LaCrO_3$	(6)
$La_2Ce_2O_7 \rightarrow La_2O_3 + Ce_2O$	(7)
$½\ La_2O_3 + ½\ Y_2O_3 \rightarrow (La, Y)_2O_3$	(8)
$½\ ZrO_2 + ½\ CeO_2 \rightarrow (Zr,Ce)O_2$	(9)
$(Zr,Ce)O_2 + NiO \rightarrow NiO(Zr, Ce)O_2$	(10)
$½\ La_2O_3 + ½\ Y_2O_3 + NiO(Zr, Ce) \rightarrow (La, Y)\ (Ni, Zr, Ce)O_3$	(11)
$½\ La_2O_3 + ½\ Y_2O_3 + CrO_3 \rightarrow (La, Y)CrO_3$	(12)

In terms of pure oxidation **Figure 6.11.** shows the system is stable and there is no decomposition observed. In LCO+YSZ dual phase high-temperature oxidation system, it was observed both structural stability and lattice parameter variations over a range of temperatures (α values varies like from as prayed 5.469, at 950°C α=5.389, at 1000°C α=5.3619, at 1050°C α=5.3619, at 1100°C α= 50504). When subjected to high-temperature oxidation, the system remains stable, with no observed decomposition. This indicates that dual phase YSZ+LCO ceramic materials are resistant to thermal degradation or oxidation over time, which is crucial for extreme environments (e.g., jet engines or turbines). The second phenomenon of structural changes in the crystal lattice. These changes are likely to be due to thermal expansion and polymorphic transitions. The reduction in lattice parameter (α) indicates that the crystal structure is shrinking or contracting as temperature increases. The explanation for this contraction lies in the ionic sizes of the elements—specifically, Yttrium (Y^{3+}) and Lanthanum (La^{3+}). According to Shannon's ionic radii:Y^{3+} has an ionic radius of 104 pm while La^{3+} has an ionic radius of 117 pm.

When these ions are incorporated into the crystal lattice, their sizes play a significant role in determining how the lattice can accommodate them. In YSZ+LCO, Y^{3+} is smaller than La^{3+}, which means that when Y^{3+} substitutes for La^{3+} in the lattice, it can fit more easily into the available space. This leads to a tighter, more compact crystal structure, particularly at high temperatures.

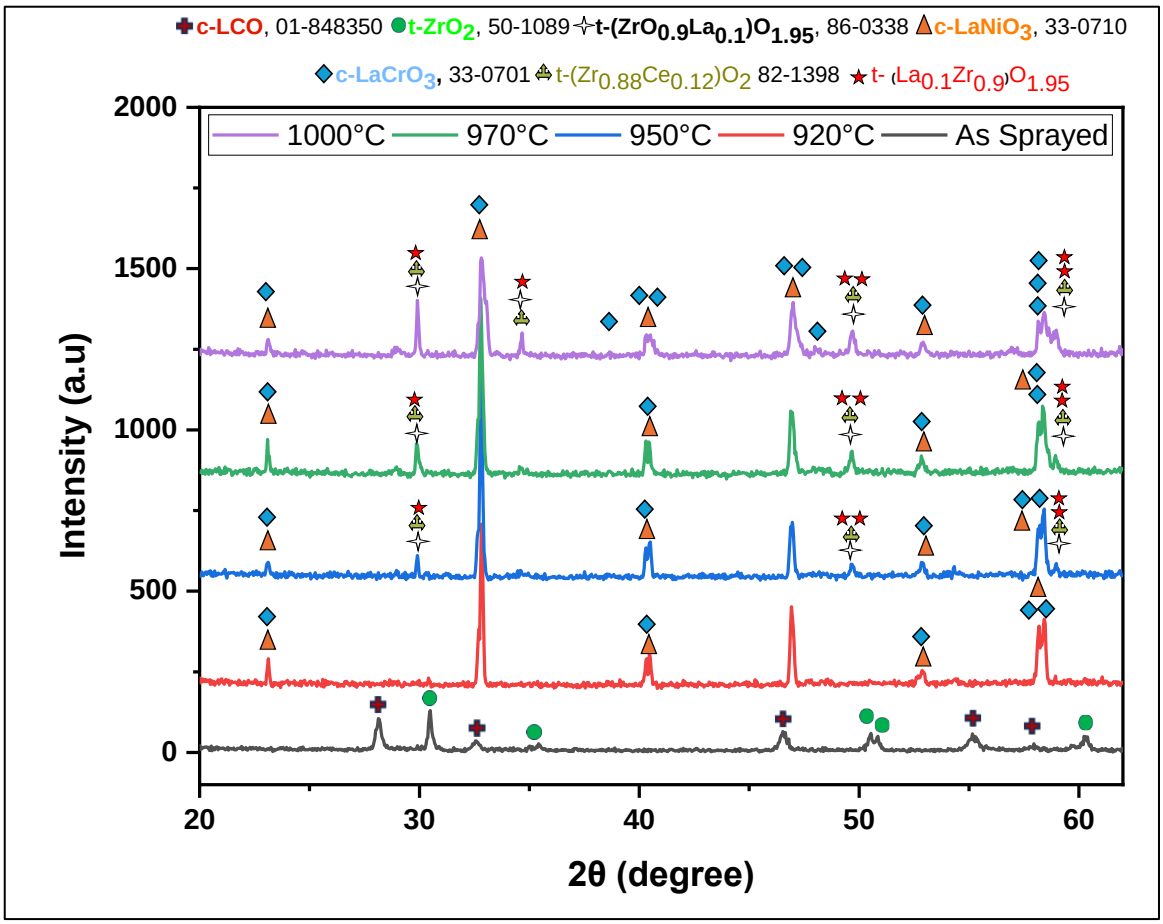

Figure 6.10. Phase constituent of hot corrosion at lower temperature for 8YSZ and LCO dual phase, as a function of temperature in sodium sulphate for 24 hours each interval.

The shrinking lattice parameter suggests that a polymorphic transition in LCO+YSZ. Based on Figure **6.11.** At 900°C and 950°C, the lattice parameter **a** decrease from 5.4693 Å (as-sprayed) to 5.3619 Å. This is a typical observation in high-temperature treatment of ceramic coatings, particularly when phase transitions are happening. The reduction in lattice parameter suggests a tightening of the crystal structure, likely due to the rearrangement of atoms or ions, such as $\mathbf{Y^{3+}}$ or $\mathbf{Zr^{4+}}$, within the lattice. At 900°C and 950°C, there's a clear transition to a more compact phase, which might involve the stabilization of certain high-temperature phases (e.g., cubic or tetragonal ZrO_2). As noted, Y^{3+} ions might be playing a stabilizing role here due to their smaller ionic radius compared to other cations like La^{3+}. Pure oxidation XRD analysis at 1050°C, became challenging due to the mixing of peaks. This could indicate the presence of multiple coexisting phases. These peaks overlap is likely due to a polymorphic transition where the material exists in a mixed phase regime—possibly a mixture of cubic PDF card number 01-0848353 and 01-0848354. The assignment of

multiple card numbers for the XRD peaks at this stage further supports the notion of a mixed phase.

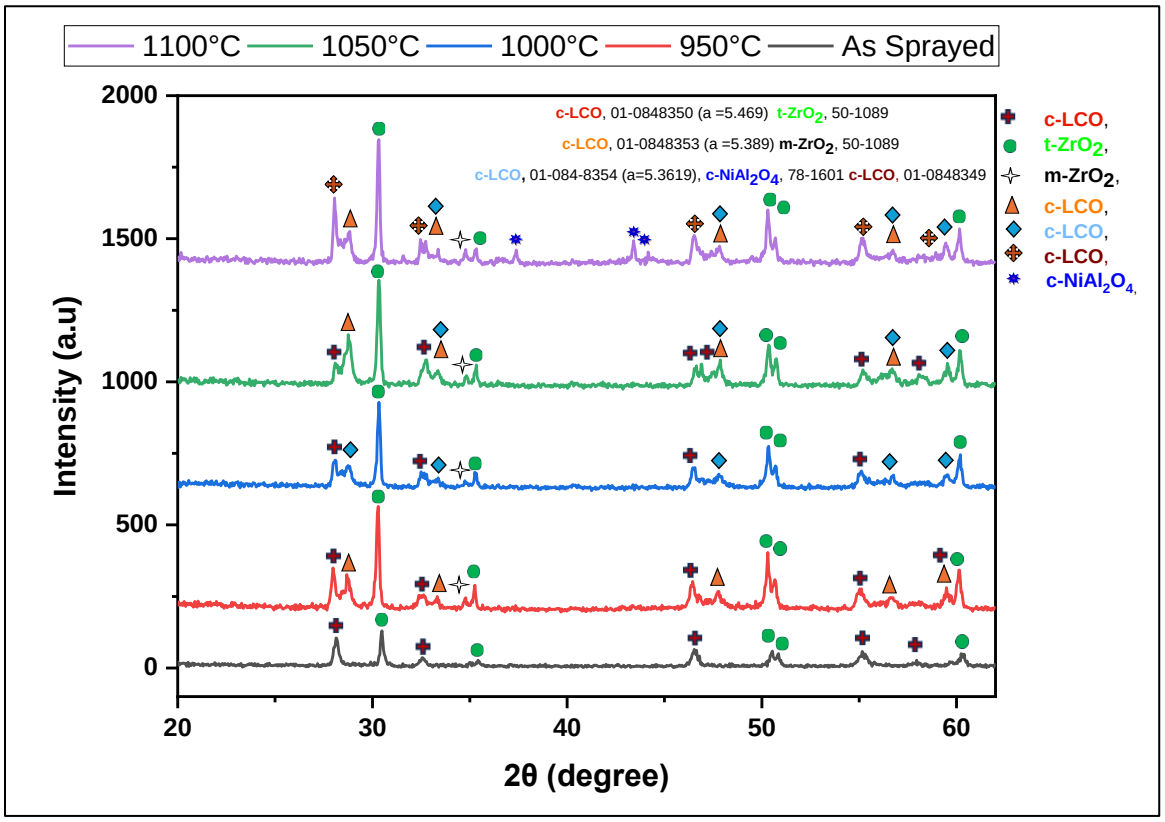

Figure 6.11. Phase constituent of pure oxidation at high temperatures for 8YSZ and LCO dual phase, as a function of temperature for 24 hours each interval.

The most interesting part of experimental observation is the sudden increase in lattice parameter at 1100°C, where a = 5.504 Å. This suggests a reverse trend—instead of further contraction, the lattice is expanding. This unexpected result might indicate several possible phenomena. One possible explanation is that the material transitions to a different phase at 1100°C—potentially a cubic phase with a larger lattice parameter. At such high temperatures, there is diffusion of elements (e.g., Ni, Al from the bond coat or TGO) into the topcoat and form the corrosion products of nickelate aluminates with PDF Card number 78-1601 as indicated in **Figure 6.11.**, which expands the lattice. The presence of diffused elements could create solid solution effects, which tend to increase the lattice parameter due to the introduction of larger or smaller atoms into the crystal structure. The top ceramic material YSZ is also experiencing anisotropic thermal expansion at this high temperature, leading to an expansion of the overall dual phase type crystal lattice. In contrast, La^{3+}, being

larger, exerts more pressure on the lattice, which can cause local distortion or expansion if La^{3+} ions dominate the structure. This is one reason why Y^{3+}-stabilized phases are often more thermally stable than La^{3+}-containing phases. The observed structural changes particularly the reduction in a value in the crystal lattice type structure and vice versa—are directly related to how the system accommodates these ions at elevated temperatures, with Y^{3+} or La^{3+} playing a key role in stabilizing the high-temperature phases and preventing decomposition. The evolution of the lattice parameter in LCO+YSZ system shows a complex interplay between phase transitions, elemental diffusion, and thermal expansion. Understanding these internal structural dynamics could pave the way for more robust, thermally stable coatings in the future.

6.3. Summary

Two phase ceramic powders for the lanthanum cerate and yttrium stabilized zirconia show stability in terms of pure oxidation rather than hot corrosion. Lanthanum based zirconates and cerates are stable in dual phase system. As there is problem of mutual interaction, dissolution in GZO based systems, although La-based systems are much more stable, but here the basic problem identified, which is interaction of alloying elements from TGO zones with TC ceramic layers. The formulated powders were mixed at room temperature and sintered at higher temperature; the studies confirm the interaction in module powder is exactly the same as in TBCs sprayed coatings.

6.4. Conclusion

The dual phase system of LCO+YSZ underwent hot corrosion at 920°C and 970°C for long-term exposure revealed significant phase changes, including decomposition and dissolution of phases within the multicomponent ceramic system as can be seen in **Table 6.1.** The important information from this research is as follows,

1. The formation of key compounds such as $LaNiO_3$ and $LaCrO_3$ at elevated temperatures was confirmed, indicating the influence of high-temperature corrosion on the material's microstructural stability.
2. Further investigations at incremental intervals of 24 h intervals in both hot corrosion and pure oxidation environments demonstrated a distinct phase behavior under each

condition, with accelerated degradation in the hot corrosion tests compared to the oxidation tests.

3. The presence of Na_2SO_4 results highlight that phase stability and resistance to corrosion are temperature-dependent, with noticeable phase transitions occurring in the temperature range studied. This mechanism is quite like the "fluxing mechanism" proposed by Raap, where phase dissolution and reprecipitation occur due to interactions with molten species during corrosion.
4. The system of LaCO with YSZ is quite stable under pure oxidation than hot corrosion test.

6.5. References

1. Mulla, J., Kaka, F., & Satapathy, R. K. (2023). The emergence of reflective thermal barrier coatings. *Critical Reviews in Solid State and Materials Sciences*, 1-25.
2. Ozcelik, A., Eker, A. A., Karabaş, M., Avci, A., & Kucukyildirim, B. O. (2024). Enhanced CMAS and hot corrosion degradation of YSZ thermal barrier coating with nano powders. *Surface and Coatings Technology*, 130624.
3. Zhong, X. H., Wang, Y. M., Xu, Z. H., Zhang, Y. F., Zhang, J. F., & Cao, X. Q. (2010). Hot-corrosion behaviors of overlay-clad yttria-stabilized zirconia coatings in contact with vanadate–sulfate salts. *Journal of the European Ceramic Society*, *30*(6), 1401-1408.
4. Iqbal, A., & Moskal, G. (2023). Recent development in advance ceramic materials and understanding the mechanisms of thermal barrier coatings degradation. *Archives of Computational Methods in Engineering*, *30*(8), 4855-4896.S
5. Wei, Z. Y., Meng, G. H., Chen, L., Li, G. R., Liu, M. J., Zhang, W. X., ... & Li, C. J. (2022). Progress in ceramic materials and structure design toward advanced thermal barrier coatings. *Journal of Advanced Ceramics*, *11*(7), 985-1068.
6. Anantharaman, A. P., & Dasari, H. P. (2021). Potential of pyrochlore structure materials in solid oxide fuel cell applications. *Ceramics International*, *47*(4), 4367-4388.
7. Xu, J., Xi, R., Xu, X., Zhang, Y., Feng, X., Fang, X., & Wang, X. (2020). A2B2O7 pyrochlore compounds: a category of potential materials for clean energy and environment protection catalysis. *Journal of Rare Earths*, *38*(8), 840-849.
8. Jitta, R. R., Gundeboina, R., Veldurthi, N. K., Guje, R., & Muga, V. (2015). Defect pyrochlore oxides: as photocatalyst materials for environmental and energy applications-a review. *Journal of Chemical Technology & Biotechnology*, *90*(11), 1937-1948.
9. Fatima, K., Abbas, Z., Naz, A., Alshahrani, T., Chaib, Y., Jaffery, S. H. A., ... & Algarni, H. (2022). Shedding light on the structural, optoelectronic, and thermoelectric properties of pyrochlore oxides (La2Q2O7 (Q= Ge, Sn)) for energy applications: A first-principles investigation. *Journal of Solid State Chemistry*, *313*, 123305.
10. Liu, X. Y., Yi, H., Che, J. W., & Liang, G. Y. (2019). Phase, compositional, structural, and chemical stability of La2Ce2O7 after high temperature heat treatment. *Ceramics International*, *45*(4), 5030-5035.
11. Cao, X., Vassen, R., Fischer, W., Tietz, F., Jungen, W., & Stöver, D. (2003). Lanthanum–cerium oxide as a thermal barrier-coating material for high-temperature applications. *Advanced Materials*, *15*(17), 1438-1442.
12. Xu, Z. H., He, L. M., Lu, F., & Mu, R. D. (2011, July). Failure of the EB-PVD TBCs of rare earth zirconates. In *Materials Science Forum* (Vol. 686, pp. 561-568). Trans Tech Publications Ltd.
13. Praveen, K., Sivakumar, S., Ananthapadmanabhan, P. V., & Shanmugavelayutham, G. (2018). Lanthanum cerate thermal barrier coatings generated from thermal plasma synthesized powders. *Ceramics International*, *44*(6), 6417-6425.
14. Singh, P., Pandit, N., & Keshri, A. K. (2024). Plasma-sprayed GNP/CNT reinforced lanthanum-cerate coatings: Hot corrosion assessment in Na2SO4-V2O5 environment. *Surface and Coatings Technology*, 130676.
15. Lashmi, P. G., Balaji, N., Kumar, S. S., & Aruna, S. T. (2021). Hot corrosion properties of plasma sprayed La2Ce2O7/YSZ vis-à-vis La2Ce2O7/cluster paired zirconia thermal barrier coatings. *Surface and Coatings Technology*, *409*, 126902.
16. Praveen, K., Shanmugavelayutham, G., Rao, D. S., & Sivakumar, G. (2022). Development of lanthanum cerate based thermal barrier coatings with enhanced resistance to ingestion by volcanic ash particles. *Corrosion Science*, *195*, 109948.
17. Iqbal, A., Moskal, G., Głowacka, H. M., Pawlik, T., & Cavalerio, A. (2023). Phase decompositions of Gd2Zr2O7+ 8YSZ TBC systems under the condition of long-term high-temperature oxidation. *Surface and Coatings Technology*, *462*, 129471.
18. Migas, D., Moskal, G., & Jucha, S. (2022). Hot corrosion behavior of double-phase Nd2Zr2O7-YSZ thermal barrier coatings. *Surface and Coatings Technology*, *449*, 128955.
19. Moskal, G., Jucha, S., Mikuśkiewicz, M., Migas, D., & Jasik, A. (2020). Atypical decomposition processes of Sm2Zr2O7+ 8YSZ dual-phase TBCs during hot corrosion. *Corrosion Science*, *170*, 108681.

20. Liu, K., Bai, Y., Li, J., Ma, J., Du, J., Cao, Y., & Li, X. (2018). Structure-property relationship and design of plasma-sprayed La2Ce2O7/8YSZ composite coatings for gas turbine blades. *Ceramics International*, *44*(12), 13662-13673.
21. Dehkharghani, A. M. F., Rahimipour, M. R., & Zakeri, M. (2021). Hot corrosion behavior of plasma sprayed La2Ce2O7/YSZ thermal barrier composite coating in the presence of Sulfate and Vanadate molten Salts. *Corrosion Science*, *183*, 109349.
22. Huo, Fupeng, Yu-An Shen, Siliang He, Keke Zhang, and Hiroshi Nishikawa. "Fabrication of NiO/ZrO2 nanocomposites using ball milling-pyrolysis method." *Vacuum* 191 (2021): 110370.

7. CONCLUSION

The conducted research aimed to determine the stability of the phase composition in a new type of composite thermal barrier coatings, comprising a mixture of two phases, namely lanthanum zirconates and gadolinium, alongside a conventional compound used in thermal barrier coatings, namely zirconium oxide modified with yttria, type 8YSZ. The third variant subjected to research was a system of lanthanum cerate with 8YSZ.

This solution demonstrated excellent insulating properties, significantly surpassing the insulating capabilities of TBCs systems based on, for example, single-phase $Ln_2Zr_2O_7$ coatings. This effect arises from the thermal resistance generated by interphase grain boundaries. However, this subject has been explored in another research that is not covered in this doctoral dissertation.

Thermal conductivity is a very important, if not critical, parameter that determines the usefulness of new materials or technological solutions in developing TBCs systems. The second equally important factor, alongside the insulating properties, is the stability of the phase composition. While in single-phase and single-layer coatings, this issue was viewed through the lens of interactions between the oxides forming the TGO zone, particularly aluminum oxide, in the case of composite coatings, the concern for phase stability in the system of ceramic materials forming the ceramic coating is equally significant.

The tendency for mutual interactions between lanthanum and gadolinium zirconates, as well as lanthanum cerate and oxide-modified zirconium oxide, was analyzed in the case under consideration. These analyses were carried out under conditions of pure oxidation and in the presence of molten sulphate salts of the Na_2SO_4 type. Analyses in an environment containing V_2O_5 were omitted, as the destruction process occurring in such an environment is very active from the perspective of the kinetics involved. This would hinder a precise description of the phenomena occurring, achievable through analysis in the sulphate salt environment.

The studies above were carried out in two modes: TBCs systems treated with plasma on samples made of nickel superalloy IN-625 and on model powders. In the first case discussed, tests were performed within a range of 900 °C up to 1100 °C (limited by the operating constraints of the substrate material). In contrast, in the second case, the tests were

conducted at higher temperatures, reaching 800 °C to 1400 °C. The research encompassed chemical and phase composition analyses, aiming to identify potential oxidation and corrosion products.

The analyses indicated that the system of ceramic compounds of the $La_2Zr_2O_7$ + 8YSZ type exhibits virtually no tendency for mutual interactions under oxidation and hot corrosion processes. No compounds were detected that could result from the decomposition of any of the primary components of the TBCs system. However, compounds formed from the reaction between nickel, chromium oxide, and lanthanum oxide were evident. The resulting chromites and nickelates stem from the oxidation of the interlayer and the diffusion of the resulting oxides to the external ceramic layer.

A different situation was observed in the case of the $Gd_2Zr_2O_7$ + 8YSZ system, where a notable tendency to form intermediate compounds within the group of non-stoichiometric zirconates was identified. These findings were corroborated during tests on model powders conducted under conditions of pure oxidation and hot corrosion in liquid salt deposits.
The differences in the behavior of lanthanum and gadolinium zirconates arise directly from the energy needed to initiate the order-disorder transformation, which has the highest value in the case of lanthanum zirconates and the lowest for gadolinium zirconates. An additional factor favoring this transformation, and possibly initiating it, is the diffusion of Y_2O_3 from 8YSZ to $La_2Zr_2O_7$, resulting in a decrease in the cation radii ratio r(La,Y) to rZr to a value below 1.46, which corresponds to the stabilization of the fluorite phase (non-stoichiometry effect).

Considering the $La_2Ce_2O_7$ + 8YSZ system, another type of mutual interaction was observed, which in this case involved the decomposition of lanthanum cerate and 8YSZ into the component oxides, as well as the formation of chromites (as in the first case) and lanthanum nickelates, alongside zirconium oxides modified with lanthanum and cerium oxide. To summarize, the research conducted provided answers to the questions posed in Chapter 1 under proposed research questions, which can be concluded as follows:

1. The thermal-phase stability of the examined systems depends on the energy required to initiate the order-disorder transformation, which is highest for lanthanum zirconate and lowest for gadolinium zirconate. This is evidenced by the absence of mutual interactions in the $La_2Zr_2O_7$ + 8YSZ system and a pronounced tendency to form non-stoichiometric phases in the $Gd_2Zr_2O_7$ + 8YSZ system.

2. The introduction of liquid Na_2SO_4 salt deposits into the system does not significantly affect the degradation process of the components that form the ceramic layer in the case of the $La_2Zr_2O_7$ + 8YSZ coating. In the case of TBCs systems of the $Gd_2Zr_2O_7$ + 8YSZ type, the tendency for mutual interactions is comparable in both pure oxidation and in an environment with the addition of sulfate salts. The observed decomposition processes of gadolinium zirconates are based on the reactions of acidic and basic oxides, as described by Rapp.

3. In none of the analyzed cases was the presence of sulphate or oxysulphate compounds detected, typical of the destruction processes of single-phase TBCs systems based on rare-earth zirconates.

4. A significantly more intensive course of destruction occurred in the case of the TBCs containing lanthanum cerate, indicating that the role of the B-type element (Zr, Ce, or Hf) is also highly important for the stability of the phase composition of the tested coatings.

5. The studies facilitated the identification of an independent degradation mechanism linked to the formation of chromites and lanthanum nickelates with a perovskite-type structure. Their presence arises from the reaction of oxides produced by the diffusion of NiO and Cr_2O_3 from the TGO zone, interacting with La_2O_3 oxide.

The results indicate a significant application potential of composite TBCs systems based on lanthanum zirconate and 8YSZ. However, further analysis is needed to ascertain the role of oxides from the TGO zone and their impact on the degradation process of the ceramic insulating layer.

ANNEX A

Copyright permission for non-open Access Pictures

CCC RightsLink

SPRINGER NATURE

Progress in ceramic materials and structure design toward advanced thermal barrier coatings

Author: Zhi-Yuan Wei et al
Publication: Journal of Advanced Ceramics
Publisher: Springer Nature
Date: Jul 2, 2022

Copyright © 2022, The Author(s)

Creative Commons

This is an open access article distributed under the terms of the Creative Commons CC BY license, which permits unrestricted use, distribution, and reproduction in any medium, provided the original work is properly cited.

You are not required to obtain permission to reuse this article.
To request permission for a type of use not listed, please contact Springer Nature

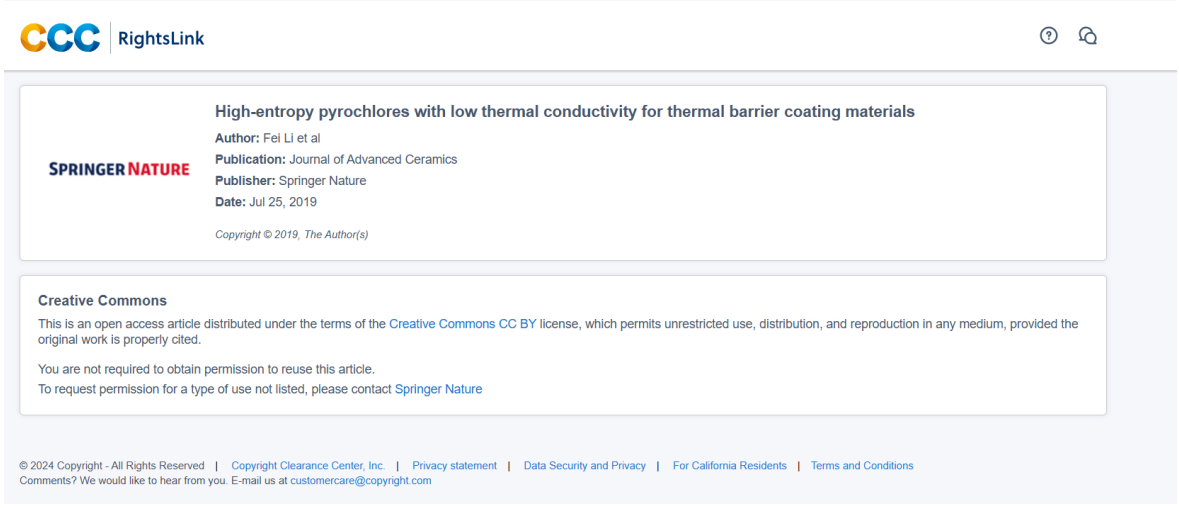

CCC RightsLink

SPRINGER NATURE

High-entropy pyrochlores with low thermal conductivity for thermal barrier coating materials

Author: Fei Li et al
Publication: Journal of Advanced Ceramics
Publisher: Springer Nature
Date: Jul 25, 2019

Copyright © 2019, The Author(s)

Creative Commons

This is an open access article distributed under the terms of the Creative Commons CC BY license, which permits unrestricted use, distribution, and reproduction in any medium, provided the original work is properly cited.

You are not required to obtain permission to reuse this article.
To request permission for a type of use not listed, please contact Springer Nature

ELSEVIER LICENSE
TERMS AND CONDITIONS

Nov 24, 2024

This Agreement between Amjad Iqbal Silesian University of Technology, Gliwice, Poland University of Coimbra, Portugal ("You") and Elsevier ("Elsevier") consists of your license details and the terms and conditions provided by Elsevier and Copyright Clearance Center.

License Number	5915390811047
License date	Nov 24, 2024
Licensed Content Publisher	Elsevier
Licensed Content Publication	Corrosion Science
Licensed Content Title	Atypical decomposition processes of Sm2Zr2O7 + 8YSZ dual-phase TBCs during hot corrosion
Licensed Content Author	Grzegorz Moskal,Sebastian Jucha,Marta Mikuśkiewicz,Damian Migas,Anna Jasik
Licensed Content Date	Jul 1, 2020
Licensed Content Volume	170
Licensed Content Issue	n/a
Licensed Content Pages	1
Start Page	108681
End Page	0
Type of Use	reuse in a thesis/dissertation

Portion	figures/tables/illustrations
Number of figures/tables/illustrations	1
Format	both print and electronic
Are you the author of this Elsevier article?	No
Will you be translating?	No
Title of new work	Characterization of destruction processes in two phase thermal barrier coatings – model investegations in condition of high temperature oxidation and corrosion in liquid salts deposits
Institution name	SUT Poland
Expected presentation date	Jan 2025
Portions	Figure # 2
The Requesting Person / Organization to Appear on the License	Amjad Iqbal Silesian University of Technology, Gliwice, Poland University of Coimbra, Portugal
Requestor Location	Mr. Amajd Iqbal Department of Mechanical Engineering, ARISE, CEMPERE, Rua Lu's Reis Santos, NIF 501617582, Order No - 4700035297 Coimbra, Coimbra 3030-788 Portugal
Publisher Tax ID	GB 494 6272 12
Customer Tax ID	PT501617582
Total	0.00 USD
Terms and Conditions	